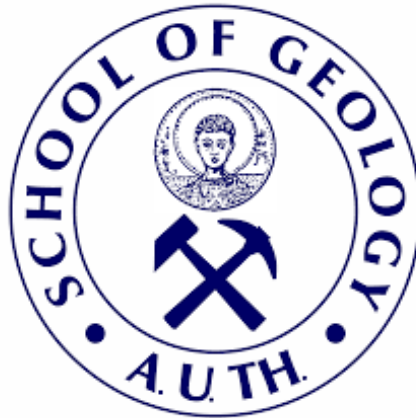




Aristotle University of Thessaloniki (A.U.Th.)
Faculty of Science
Department of Geophysics



Estimation of spectral amplification coefficients of seismic motion in Greece and comparison with the corresponding coefficients of the 'Eurocode 8' Antiseismic Code

A thesis submitted for the partial fulfillment of the requirements for the Master degree

in

Postgraduate studies programme: 'Applied and Environmental Geology', direction: 'Applied Geophysics and Seismology'

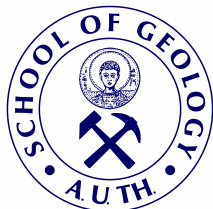
by

Eirini Chatzianagnostou

Thessaloniki

2024





Aristotle University of Thessaloniki
(AUTH)
Faculty of Science
Department of Geophysics
54124, Thessaloniki, Greece

Estimation of spectral amplification coefficients of seismic motion in Greece and comparison with the corresponding coefficients of the 'Eurocode 8' Antiseismic Code

Eirini Chatzianagnostou
Graduate Geologist

THREE-MEMBER EXAMINING BOARD

Prof. Hatzidimitriou Panayiotis, Professor of Seismology, A.U.T.H., Supervisor.

Dr. Theodoulidis Nikolaos, Director of Research, I.T.S.A.K., Board Member.

Dr. Triantafyllidis Petros, Laboratory Teaching Staff, A.U.T.H., Board Member.

Oral Examination:

Place: Thessaloniki

Date: 08/07/2024



© Eirini Chatzianagnostou, 2024
All rights reserved.

ESTIMATION OF SPECTRAL AMPLIFICATION COEFFICIENTS OF SEISMIC MOTION IN GREECE AND COMPARISON WITH THE CORRESPONDING COEFFICIENTS OF 'EUROCODE 8' ANTISEISMIC CODE – Master Thesis

© Ειρήνη Χατζηαναγνώστου, 2024
Με επιφύλαξη παντός δικαιώματος.

ΕΚΤΙΜΗΣΗ ΣΥΝΤΕΛΕΣΤΩΝ ΦΑΣΜΑΤΙΚΗΣ ΕΝΙΣΧΥΣΗΣ ΣΕΙΣΜΙΚΗΣ ΚΙΝΗΣΗΣ ΣΤΗΝ ΕΛΛΑΔΑ ΚΑΙ ΣΥΓΚΡΙΣΗ ΜΕ ΤΟΥΣ ΑΝΤΙΣΤΟΙΧΟΥΣ ΣΥΝΤΕΛΕΣΤΕΣ ΤΟΥ ΑΝΤΙΣΕΙΣΜΙΚΟΥ ΚΑΝΟΝΙΣΜΟΥ 'ΕΥΡΩΚΩΔΙΚΑ 8' – Μεταπτυχιακή Διπλωματική Εργασία

Citation:

Chatzianagnostou E., (2024). "Estimation of spectral amplification coefficients of seismic motion in Greece and comparison with the corresponding coefficients of 'Eurocode 8' Antiseismic Code". Master Thesis, School of Geology, Aristotle University of Thessaloniki.

Χατζηαναγνώστου Ε., (2024). "Εκτίμηση συντελεστών φασματικής ενίσχυσης σεισμικής κίνησης στην Ελλάδα και σύγκριση με τους αντίστοιχους συντελεστές του Αντισεισμικού Κανονισμού 'Ευρωκώδικα 8'". Μεταπτυχιακή Διπλωματική Εργασία, Τμήμα Γεωλογίας Α.Π.Θ.

It is forbidden to copy, store and distribute this work, in whole or in part, for commercial purposes. Reproduction, storage and distribution are permitted for non-profit, educational or research purposes, provided the source of origin is indicated. Questions concerning the use of work for profit-making purposes should be addressed to the author.

The views and conclusions contained in this document express the author and should not be interpreted as expressing the official positions of the Aristotle University of Thessaloniki.



ACKNOWLEDGEMENTS

The present study was prepared in the context of a research project SIREAT, *Argonet+*, by the Institute of Engineering Seismology and Earthquake Engineering (I.T.S.A.K.).

First of all, I would like to express my sincere gratitude to one of my supervisors, Dr. Nikolaos Theodoulidis, for his support and belief in me and my potentials. Under his guidance, I acquired a great deal of knowledge of scientific methods and experimental tools needed for the present study and my future work. I am more than grateful to Prof. Professor Panayiotis Hatzidimitriou, my supervisor and Dr. Petros Triantafyllidis, member of the examining board, for being great teachers to me and for all the scientific and personal advice they gave to me. Of course, I need to thank Ioannis Grendas, postdoctoral researcher, for his dedicated help and his contribution to this study, his willingness to discuss my questions about the subject, and, most importantly, for his major support to continue. I would like to thank Giorgos Papadopoulos, Master graduate from AUTH, for the technical knowledge he shared with me and Ioanni Maragkaki for providing the earthquake data. Since this thesis submission stands as a closure of my master studies, I take the opportunity to thank all my tutors for their persistence in addressing our needs and for making these two years full of knowledge and truly rewarding.

Last but not least, I owe a big thanks to my friends and family for always encouraging me.



ABSTRACT

Site characterisation at a target site is a fundamental component in understanding the geotechnical characteristics and predicting site's ground response for seismic hazard assessment. Seismic building codes usually adopt as a fundamental parameter for site classification the average velocity of S-waves at the topmost 30 m of the subsurface, V_{S30} . However, to address the limitations of this approach, efforts towards new seismic codes have been attempted, introducing additional parameters. The primary aim of this dissertation is to enhance seismic hazard assessment by presenting an integrated approach for Site Amplification Factors (SAFs) estimation, by considering both the seismological, $H_{3\text{km/s}}$, and engineering, $H_{0.8\text{km/s}}$ bedrock, using 152 stations of ITSAK accelerometer network, throughout Greece. The Horizontal Spectral Amplification Factors (HSAFs) estimated down to $H_{0.8\text{km/s}}$, have been utilised in categorisation per soil type according to the European current seismic building code (Eurocode 8, EC8-1) and the new version of 2024 draft of EC8. For each category in both EC8 versions, an average HSAF was calculated and juxtaposed along with the standard site amplification factors determined in the codes. Horizontal and Vertical SAFs alongside with seismic source (moment magnitude M_o , stress drop $\Delta\sigma$) and propagation path factors (geometrical spreading γ , quality, Q) of shear wave window of recordings, were estimated through the Generalized Inversion Technique (GIT). Six stations were selected as references, which were located on 'rock' formations all over Greece, according to IGME geological maps. Ambient noise measurements (mHVSR) and dispersion curves data at those six reference sites were utilised for a joint inversion, using 'HV-inv' software, taking into account the Diffused Field Assumption (DFA), in order to acquire 1D profiles of shear wave velocity with respect to depth, V_{sz} , down to seismological bedrock. These six reference sites profiles, were then used to estimate their corresponding 1D theoretical Site spectral Amplification Factors ($SAFs^{theoretical}$) for $H_{0.8\text{km/s}}$ and $H_{3\text{km/s}}$, in order to adapt their observed Fourier Amplification Spectra (FAS) on the surface to their equivalent on bedrock. Then, the deconvolved FAS were fed in the GIT and the resulting seismic source, path and site factors for $H_{0.8\text{km/s}}$ were compared with the corresponding ones for $H_{3\text{km/s}}$, revealing small differences for the first two factors and more discernible for the site factor. Furthermore, the inverse of the horizontal-to-vertical spectra ratio, $V_b H_b R$, which is used to convert the amplitude of horizontal S-waves into vertical P-waves, was evaluated for each reference site. Since the horizontal-to-vertical spectral ratio of earthquake recordings (eHVSR) also contain the vertical amplification there is need to correct the VSAF. For this purpose, the Vertical Amplification Correction Functions (VACFs) were determined utilising the HSAFs as resulted from the GIT analysis, which could be used to blindly estimate the HSAF at a site. An average VACF was calculated for all 152 stations and an average VACF for eight categories based on the fundamental frequency, f_0 , and the corresponding amplification, A_0 , of eHVSR data. Finally,



the 152 accelerometer station sites were characterised according to the current EC8 and the draft 2024 EC8. While overall comparisons of HSAF and the corresponding EC8 amplification factors per category align satisfactorily, certain discrepancies and limitations were identified and discussed.



ΠΕΡΙΛΗΨΗ

Η εδαφική κατηγοριοποίηση μιας θέσης αποτελεί θεμελιώδες στοιχείο για την κατανόηση των γεωλογικών χαρακτηριστικών αλλά και την πρόβλεψη της εδαφικής της απόκρισης, με στόχο την ακριβέστερη εκτίμηση της σεισμικής επικινδυνότητας. Αρκετοί αντισεισμικοί κανονισμοί υιοθετούν ως κύρια παράμετρο για την εδαφική ταξινόμηση μιας θέσης, τη μέση ταχύτητα των εγκάρσιων κυμάτων στα αρχικά 30 m του υπεδάφους, V_{S30} . Ωστόσο, εντοπίστηκαν αρκετοί περιορισμοί στη προσέγγιση αυτή, οδηγώντας σε τροποποιήσεις των αντισεισμικών κανονισμών, εισάγοντας επιπρόσθετες παραμέτρους. Πρωταρχικός στόχος αυτής της διατριβής είναι η βελτίωση των εκτιμήσεων της σεισμικής επικινδυνότητας, παρουσιάζοντας μια προσέγγιση για την εκτίμηση των φασματικών παραγόντων ενίσχυσης (Site Spectral Amplification Factors, SAFs), τόσο για το σεισμολογικό, $H_{3\text{km/s}}$ όσο και το βραχώδες, $H_{0.8\text{km/s}}$, υπόβαθρο, αξιοποιώντας 152 σταθμούς του δικτύου επιταχυνσιογράφων του Ινστιτούτου Τεχνικής Σεισμολογίας και Αντισεισμικών Κατασκευών (Ι.Τ.Σ.Α.Κ.) από όλο τον ελλαδικό χώρο. Οι συντελεστές φασματικής ενίσχυσης οριζόντιας συνιστώσας (HSAFs) που υπολογίστηκαν για $H_{0.8\text{km/s}}$, χρησιμοποιήθηκαν στη κατηγοριοποίηση ανά τύπο εδάφους σύμφωνα με τον ισχύοντα ευρωπαϊκό αντισεισμικό κανονισμό (Ευρωκώδικας 8, EC8-1) και τη νέα έκδοση του 2024 EC8. Για κάθε κατηγορία εδάφους που ορίζεται και στους δύο ευρωκώδικες EC8 υπολογίστηκε ένας μέσος όρος HSAF και συγκρίθηκε με τους αντίστοιχους συντελεστές που ορίζονται στους δύο κώδικες. Τα SAFs της οριζόντιας και κατακόρυφης συνιστώσας, μαζί με παράγοντες της σεισμικής πηγής (σεισμική ροπή, M_0 , πτώση τάσης, $\Delta\sigma$) και του δρόμου διαδρομής (συντελεστής γεωμετρικής διασποράς γ , συντελεστής ποιότητας, Q) των φασμάτων Fourier, εκτιμήθηκαν μέσω της Γενικευμένης Αντιστροφής (Generalized Inversion Technique, GIT). Επιλέχθηκαν έξι σταθμοί αναφοράς σε όλη την Ελλάδα, εγκατεστημένοι σε βραχώδεις σχηματισμούς, σύμφωνα με τους γεωλογικούς χάρτες του ΙΓΜΕ. Οι μετρήσεις περιβαλλοντικού θορύβου (mHVSR) και οι υπολογισμοί των καμπυλών διασποράς σε αυτές τις έξι θέσεις, χρησιμοποιήθηκαν σε μια κοινή αντιστροφή, χρησιμοποιώντας το λογισμικό 'HV-inv', λαμβάνοντας υπόψη την υπόθεση της διάχυσης της σεισμικής ενέργειας (Diffused Field Assumption, DFA), με στόχο την ανάκτηση μονοδιάστατου (1D- V_{sz}) προφίλ μέχρι το βάθος του σεισμολογικού υποβάθρου. Αυτά τα έξι προφίλ στις θέσεις αναφοράς, στη συνέχεια χρησιμοποιήθηκαν για την εκτίμηση των 1D θεωρητικών φασματικών παραγόντων ενίσχυσης (1D theoretical Site spectral Amplification Factors, $SAFs^{theoretical}$) για $H_{0.8\text{km/s}}$ και $H_{3\text{km/s}}$, προκειμένου να γίνει αναγωγή των παρατηρούμενων φασμάτων Fourier (FAS) από την επιφάνεια στο ζητούμενο υπόβαθρο. Στη συνέχεια, τα διορθωμένα FAS αξιοποιήθηκαν στη τροφοδοτήθηκαν στον κώδικα της GIT και οι προκύπτοντες παράγοντες σεισμικής πηγής, διαδρομής και θέσης ενδιαφέροντος για $H_{0.8\text{km/s}}$ συγκρίθηκαν με τους αντίστοιχους για $H_{3\text{km/s}}$, αποκαλύπτοντας διαφορές μικρές για τους δύο πρώτους παράγοντες και πιο ευδιάκριτες στη περίπτωση των τοπικών εδαφικών συνθηκών. Επιπλέον, ο αντίστροφος φασματικός λόγος της οριζόντιας προς την κατακό-

ρυφη συνιστώσα, $V_b H_b R$, που χρησιμοποιείται για τη μετατροπή του πλάτους των οριζόντιων εγκαρσίων κυμάτων σε κατακόρυφα επιμήκη κύματα, αξιολογήθηκε για κάθε ένα σταθμό αναφοράς. Καθώς το eHVSR περιέχει, επιπλέον, την κατακόρυφη ενίσχυση, απαιτείται η διόρθωση του VSAF. Για τον σκοπό αυτό προσδιορίστηκε η συνάρτηση διόρθωσης της κατακόρυφης φασματικής ενίσχυσης (Vertical Amplification Correction Function, VACF) με τη χρήση των HSAF που προέκυψαν από το GIT. Ένας μέσος όρος VACF υπολογίστηκε για τους 152 σταθμούς, αλλά επίσης, ένας μέσος VACF για τις οκτώ κατηγορίες εδαφών με βάση τη θεμελιώδη συχνότητα, f_0 , και το αντίστοιχο πλάτος, A_0 , των δεδομένων eHVSR. Τέλος, οι 152 θέσεις των σταθμών επιταχυνσιογράφων κατηγοριοποιήθηκαν σύμφωνα με τις οδηγίες του ισχύοντος EC8 και του 2024 draft EC8. Ενώ η σύγκριση των εκτιμηθέντων HSAF με αυτούς του ερωκώδικα τόσο για το σύνολο των σταθμών όσο και για κάθε κατηγορία εδαφών εμφανίζουν ικανοποιητική συμφωνία, εντοπίστηκαν ορισμένες αποκλίσεις και συζητούνται περιορισμοί που προκύπτουν.



List of Acronyms

| | |
|-----------------------|---|
| $SAF^{theoretical}$ | Site Spectral Amplification Factor at the six Reference Sites. xv, xvi, 5, 32–34, 36, 38, 39, 41, 48, 64–67 |
| V_{S30} | The average shear wave velocity for the top 30 m of soil. xviii, 1, 2, 4, 14, 58–60, 67 |
| V_{SZ} | Profile of shear wave velocity with respect to depth. xii, xiii, xvii, 3, 5, 8, 11, 18–20, 23, 24, 28, 30, 32, 34, 38, 39, 48, 49, 65, 66, 68 |
| $H_{0.8\text{ km/s}}$ | The engineering bedrock the depth (H) where shear wave velocity (V_S) reaches 0.8 km/s. xvi, xvii, 4, 5, 34, 39, 40, 42–48, 52, 64–68 |
| $H_{3\text{ km/s}}$ | The seismological bedrock the depth (H) where shear wave velocity (V_S) reaches 3 km/s. xvi, xvii, 5, 34, 39, 40, 42–48, 51, 64, 65, 67 |
| $V_b H_b R$ | Bedrock Vertical-to-Horizontal Ratio. xvii, 5, 12, 18, 51, 52, 65, 67, 68 |
| DFA | Diffuse Field Assumption. xii, xvii, 3, 8–10, 12, 19, 52, 67 |
| EC8 | Eurocode 8. xiii, xviii, xix, xxi, 4, 55–63, 65–68 |
| eHVSR | Horizontal-to-Vertical Spectral Ratio resulted from earthquake recordings. xvii, xviii, 3, 10–12, 17, 18, 50, 51, 53–57, 61, 65, 66 |
| EMR | Earthquake-to-Microtremor Ratio. xviii, 18, 57 |
| FAS | Fourier Amplitude Spectra on surface. 2, 3, 11, 12, 14, 18, 34, 38, 39, 41, 42, 54, 65, 66, 68 |

| | |
|-------|---|
| GIT | Generalized Inversion Technique. xii, xiii, xvii, xviii, 2–5, 11–13, 18, 38, 39, 41, 42, 44, 47–51, 53–55, 58, 64, 65, 67 |
| HSAF | Horizontal Site Amplification Factor. xvii–xix, 1, 3, 4, 12, 49–51, 53, 55–57, 59, 60, 62–66 |
| HVSR | Horizontal-to-Vertical Spectral Ratio. xii, 7, 9, 10, 14, 17–21, 23, 24, 26 |
| mHVSR | Horizontal-to-Vertical Spectral Ratio using ambient noise records. xii, xiv, xv, 3, 5, 9, 10, 15, 17–20, 22, 24, 26, 28, 30, 32, 57, 64, 66 |
| SAF | Site Amplification Factor. 1–4, 39, 67 |
| TF | Transfer Function. 10, 11 |
| VACF | Vertical Amplification Correction factor. xiii, xviii, 3, 5, 12, 52–57, 65–67 |
| VHSR | Vertical-to-Horizontal Spectral Ratio at surface. xviii, 52, 53 |
| VSAF | Vertical Site Amplification Factor. xvii, 12, 18, 47, 49–51, 65 |



Contents

| | |
|--|-----------|
| List of Acronyms | x |
| 1 Introduction | 1 |
| 2 Methodology | 5 |
| 2.1 Inversion of HVSR spectral ratios and Dispersion Curves under the Diffuse Field Assumption | 7 |
| 2.1.1 Horizontal-to-Vertical Spectral Ratio technique (HVSR) | 7 |
| 2.1.2 Dispersion Curves | 8 |
| 2.1.3 Inversion under the Diffuse Field Assumption (DFA) | 8 |
| 2.2 Theoretical Site Spectral Amplification Factors ($SAF_s^{theoretical}$) | 10 |
| 2.3 Generalized Inversion Technique (GIT) | 11 |
| 3 Data Used | 14 |
| 3.1 HVSR and Dispersion Curve data | 14 |
| 3.2 Fourier Amplitude Spectra of S-waves | 16 |
| 3.3 Fundamental Frequency Analysis to Estimate Bedrock Depth | 17 |
| 4 Data processing and results | 18 |
| 4.1 Joint Inversion of mHVSR and Dispersion Curve | 19 |
| 4.1.1 'HV-Inv' algorithm for 1D V_{SZ} profiles | 19 |
| 4.1.2 V_{SZ} profiles generation for the reference stations | 20 |



| | | |
|----------|--|-----------|
| 4.2 | 1D - Theoretical Site Spectral Amplification Factors ($SAF_s^{theoretical}$) of 6 Reference Stations | 32 |
| 4.3 | Generalized Inversion Technique (GIT) | 38 |
| 4.3.1 | Selection of V_{SZ} profiles of reference stations for GIT implementation | 38 |
| 4.3.2 | Final GIT for Source, Path, and Site Factors Determination | 41 |
| 4.3.2.1 | Seismic Source Factors | 42 |
| 4.3.2.2 | Attenuation Factors | 43 |
| 4.3.2.3 | Site Amplification Factors (SAFs) | 47 |
| 4.3.3 | Vertical Amplification Correction Functions (VACFs) | 52 |
| 4.4 | Soil type categorisation according to Eurocode 8 (EC8) and comparison with SAFs | 57 |
| 4.4.1 | Categorisation according to the current EC8 | 58 |
| 4.4.2 | Categorisation according to EC8 2024 draft | 60 |
| 5 | Discussion and Conclusions | 64 |
| A | Site Amplification Factors (SAFs) for the 152 stations | 79 |
| A | mHVSRS of 132 stations out of the 152 total stations. | 89 |
| A | Additional tables | 96 |



List of Figures

| | | |
|-----|---|----|
| 2.1 | A schematic flowchart that shows the steps of this thesis. | 6 |
| 2.2 | Illustration of the source of waveform, the path and the site effects in sediment formations. | 7 |
| 3.1 | Map of reference station locations | 15 |
| 3.2 | Map showing the earthquakes selected for this study (right) as well as the ray paths (left) derived between the hypocenters (red) and the recording stations (blue). | 16 |
| 4.1 | Results of joint inversions of empirical mHVSR and dispersion curves for the reference station 'AIG2'. Black line error bars in 4.1a and 4.1b represent the experimental mHVSR and dispersion curve, respectively, with assumed standard deviation 40%, while the red lines represent the corresponding theoretical ones. In 4.1c, the coloured lines show the forward calculations for the velocity models, the black line represents the mean model, while the red line the best fitting model for V_P , V_S (m/s) and density (kg/m^3), from left to right. | 22 |
| 4.2 | Results of joint inversions of empirical mHVSR and dispersion curves for the reference station 'ART2'. Black line error bars in 4.2a and 4.2b represent the experimental mHVSR and dispersion curve, respectively, with assumed standard deviation at 40%, while the red lines represent the corresponding theoretical ones. In 4.2c, the coloured lines show the forward calculations for the velocity models, the black line represents the mean model, while the red line the best fitting model for V_p , V_s (m/s) and density (kg/m^3), from left to right. | 24 |



| | | |
|-----|---|----|
| 4.3 | Results of joint inversions of empirical mHVSR and dispersion curves for the reference station 'ATH5'. Black line error bars in 4.3a and 4.3b represent the experimental mHVSR and dispersion curve, respectively, with assumed standard deviation at 40%, while the red lines represent the corresponding theoretical ones. In 4.3c, the coloured lines show the forward calculations for the velocity models, the black line represents the mean model, while the red line the best fitting model for V_P , V_S (m/s) and density (kg/m^3), from left to right. | 26 |
| 4.4 | Results of joint inversions of empirical mHVSR and dispersion curves for the reference station 'SEIS'. Black line error bars in 4.4a and 4.4b represent the experimental mHVSR and dispersion curve, respectively, with assumed standard deviation at 40%, while the red lines represent the corresponding theoretical ones. In 4.4c, the coloured lines show the forward calculations for the velocity models, the black line represents the mean model, while the red line the best fitting model for V_P , V_S (m/s) and density (kg/m^3), from left to right. | 28 |
| 4.5 | Results of joint inversions of empirical mHVSR and dispersion curves for the reference station 'SIA'. Black line error bars in 4.5a and 4.5b represent the experimental mHVSR and dispersion curve, respectively, with assumed standard deviation at 40%, while the red lines represent the corresponding theoretical ones. In 4.5c, the coloured lines show the forward calculations for the velocity models, the black line represents the mean model, while the red line the best fitting model for V_P , V_S (m/s) and density (kg/m^3), from left to right. | 30 |
| 4.6 | Results of joint inversions of empirical mHVSR and dispersion curves for the reference station "VSK1". Black line error bars in 4.6a and 4.6b represent the experimental mHVSR and dispersion curve, respectively, with assumed standard deviation at 40%, while the red lines represent the corresponding theoretical ones. In 4.6c, the colored lines show the forward calculations for the velocity models, the black line represents the mean model, while the red line the best fitting model for V_P , V_S (m/s) and density (kg/m^3), from left to right. | 32 |
| 4.7 | $SAF_{HV-Inv}^{theoretical}$. $SAF^{theoretical}$ for depths where the V_s reaches 0.8 km/s (left), and 3 km/s (right). Horizontal component is represented by the black line, while the vertical component by the grey line. | 36 |



LIST OF FIGURES

4.8 $SAFs_{HV-Inv}^{theoretical}$ (solid lines) and $SAFs_{G-D}^{theoretical}$ (dashed lines). $SAF^{theoretical}$ for depths, where the V_s reaches 0.8 km/s (left), and 3 km/s (right). Black line represent horizontal $SAFs_{HV-Inv}^{theoretical}$ and dark blue horizontal $SAFs_{G-D}^{theoretical}$. Grey line represent vertical $SAFs_{HV-Inv}^{theoretical}$ and light blue line vertical $SAFs_{G-D}^{theoretical}$ 38

4.9 Inverted Moment Magnitude (M_w (inv)) versus inverted observed Moment magnitude (M_w (init)) (top). With dashed lines, the range of ± 0.2 of the bisector is depicted. Comparison between the inversion calculated corner frequencies, f_c and the computed M_w , alongside with the Brune's stress drop lines (bottom). 40

4.10 Comparison of Horizontal Site Amplification Factors (HSAF) for 6 random stations all over Greece, between 'HV-Inv' (grey line) and Geopsy-Dinver (black line), with respect to engineering bedrock (4.10a) and seismological bedrock (4.10b) 41

4.11 Comparison between Inverted Moment Magnitude ($M_{w(inv)}$) and observed Moment Magnitude ($M_{w(init)}$). For engineering bedrock $H_{0.8 \text{ km/s}}$ (left) and seismological bedrock $H_{3 \text{ km/s}}$ (middle). With dashed lines, the range of ± 0.2 of the bisector is depicted. On the right plot direct comparisons between the two bedrock delineations are presented, featuring the $M_{w(inv)}$ for $H_{0.8 \text{ km/s}}$ and $H_{3 \text{ km/s}}$, with a bisector as a reference line, and the corresponding ratio (%) according to $\left(\frac{M_{w_{H_{3 \text{ km/s}}}}}{M_{w_{H_{0.8 \text{ km/s}}}}} - 1 \right) \cdot 100\%$ versus the number of data 42

4.12 Comparison of the computed corner frequencies, f_c , and the inverted M_w , alongside with the Brune's stress drop lines. For engineering bedrock $H_{0.8 \text{ km/s}}$ (left) and seismological bedrock $H_{3 \text{ km/s}}$ (middle). On the right plot direct comparisons between the two bedrock delineations are presented, featuring the f_c for $H_{0.8 \text{ km/s}}$ and $H_{3 \text{ km/s}}$ with their bisector as a reference line, and the corresponding ratio (%) according to $\left(\frac{f_{c_{H_{3 \text{ km/s}}}}}{f_{c_{H_{0.8 \text{ km/s}}}}} - 1 \right) \cdot 100\%$ versus the number of data. 43

4.13 Maps corresponding to the computed $Q(f)$ for the frequencies 0.5 Hz (left), 1 Hz (middle) and 5 Hz (right). For $H_{0.8 \text{ km/s}}$ (top) and $H_{3 \text{ km/s}}$ (bottom) 45

4.14 Maps corresponding to the uncertainties of $Q(f)$ for frequencies 0.5 Hz (left), 1 Hz (middle) and 5 Hz (right). For $H_{0.8 \text{ km/s}}$ (top) and $H_{3 \text{ km/s}}$ (bottom) 45



LIST OF FIGURES

4.15 Maps corresponding to the smoothed values of $Q(f)$ with $CV \leq 7$ for frequencies 0.5 Hz (left), 1 Hz (middle) and 5 Hz (right). For $H_{0.8 \text{ km/s}}$ (top) and $H_{3 \text{ km/s}}$ (bottom) 46

4.16 Comparison of the quality factor, Q_0 for $H_{0.8 \text{ km/s}}$ and $H_{3 \text{ km/s}}$. The dashed line represents the bisector as a reference line. Inner plot: Q_0 ratio (%) for each of the 241 studied subareas. b) The ratio of α (%) for each of the 241 studied subareas. c) Comparison of geometrical spreading coefficient, γ for $H_{0.8 \text{ km/s}}$ (grey points) and $H_{3 \text{ km/s}}$ (black points) with $\pm \text{std}$. Inset lower plot: The relative difference between $\gamma_{3 \text{ km/s}}$ and $\gamma_{0.8 \text{ km/s}}$. Inset upper plot: The relative difference between $\gamma_{3 \text{ km/s}}$ and $\gamma_{0.8 \text{ km/s}}$ amplify with increasing epicentral distance, r , while the colorbar represents the number of seismic rays at each distance r . 47

4.17 The Horizontal Site Amplification Factors (HSAFs) at 9 selected stations all over Greece for $H_{3 \text{ km/s}}$ (black line), and $H_{0.8 \text{ km/s}}$ (grey line). 48

4.18 Top: $HSAFs^{GIT}$ ratios ($HSAF_{3 \text{ km/s}}^{GIT} / HSAF_{0.8 \text{ km/s}}^{GIT}$) with the geometrical mean of that ratio and \pm a standard deviation. Middle: $HSAFs^{theoretical}$ ratios ($HSAF_{3 \text{ km/s}}^{theoretical} / HSAF_{0.8 \text{ km/s}}^{theoretical}$) derived from the 1D- V_{SZ} profiles of the six reference stations with the geometrical mean of that ratio and \pm a standard deviation. Bottom: The above mentioned geometrical means and the corresponding std alongside with the least squares fit (green dashed line). 49

4.19 HSAF and VSAF correlation obtained by GIT regarding the maximum amplitudes (left) and the geometrical average amplitudes (right) for the 152 stations. The linear regression lines and the regression coefficients are depicted, as well as the correlation coefficient, R^2 50

4.20 HSAF obtained by GIT and eHVSR correlation in regards to (a) the maximum amplitudes and (b) the geometrical average amplitudes for the 152 stations. Furthermore, the linear regression lines and the regression coefficients are depicted, as well as the R^2 51

4.21 Comparison of $V_b H_b R$ curves for engineering and seismological bedrock. (a) The $V_b H_b R$ curve (red) for all six reference stations down to engineering bedrock ($H_{0.8 \text{ km/s}}$) alongside with their geometrical average (black line) with $\pm 1 \text{std}$ (dashed black line). Green line: the theoretical solution from the diffuse field assumption (DFA). (b) The $V_b H_b R$ curve (red) for all six reference stations down to seismological bedrock ($H_{3 \text{ km/s}}$) alongside with their geometrical average (black line) with $\pm 1 \text{std}$ (dashed black line). Green line: the theoretical solution from the diffuse field assumption (DFA). 52



| | | |
|------|--|----|
| 4.22 | Left: Log-average VACFs for eight site categories classified by the maximum eHVSR, where f_p is the peak frequency and A_p the corresponding peak amplitude. Right: Log-average VACFs for ten site categories classified by the maximum eVHSR, where f_p is the peak frequency and A_p the corresponding peak amplitude. Stations were categorized into only four of the ten categories. | 53 |
| 4.23 | Simulated HSAFs according to equation 4.12 (blue circles) and the observed on the surface eHVSRs (open circles) versus the calculated HSAFs from GIT analysis. From left to right the horizontal axis for peak amplitude and in the Fourier spectral amplitudes at 0.5, 1.0, 2.0 and 5 Hz. | 54 |
| 4.24 | Variation of the logarithmic average empirical VACF for all 152 stations (black curves) $\pm std$, in comparison with the curves calculated for Japanese data (blue curves) $\pm std$, by Ito et al., [33] | 55 |
| 4.25 | Variation of the logarithmic average VACF (black curve) for all 152 stations (green curves) divided by the type per soil of each site according to the current EC8. | 56 |
| 4.26 | Comparison of simulated HSAFs by employing the log-average VACF and its calculated standard deviation (black lines), the simulated HSAF based on the peak amplitude (A_p) and peak frequency (f_p) in observed eHVSR data (green line), the corrected SSR (red line), and the eHVSR (green line) at stations CK0 (left) and TST (right). | 56 |
| 4.27 | Earthquake-to-microtremor ratio, EMR for each out of 152 stations (coloured lines) alongside with the logarithmic mean and $\pm 1std$ (black solid and dashed lines) | 57 |
| 4.28 | Colour representation of the categorization of sites according to the current EC8 in a V_{s30} versus fundamental frequency (Hz) plot. | 59 |
| 4.29 | Left: Upper and lower limits of period-dependent site amplification factors for $V_{s30} = 0.8 \text{ km/s}$ for category A, for category B $360 \text{ m/s} \leq V_{s30} < 0.8 \text{ km/s}$, $180 \text{ m/s} \leq V_{s30} < 360 \text{ m/s}$ for category C, and $150 \text{ m/s} \leq V_{s30} < 180 \text{ m/s}$ for D, according to the GMMs by Boore et al.[12] (grey dashed dotted lines) alongside with the corresponding amplification factors according to the current EC8 (black lines). Right: Amplification factors according to the current EC8 (black lines), considering high seismicity regions. And the HSAF (green dashed dotted lines) with the estimated logarithmic mean (green curve) and $\pm 1std$. | 60 |

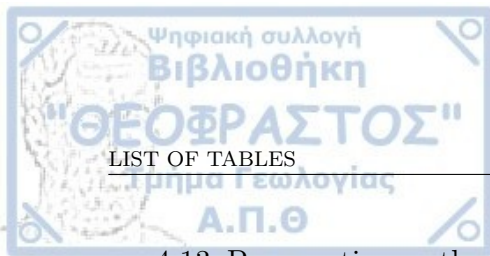


| | | |
|------|--|----|
| 4.30 | Amplification factors according to EC8 2024 draft (black lines) with a standard deviation (dashed black lines), considering high seismicity regions ($S_{\alpha,RP} = 6 \text{ m/s}^2$, $S_{\beta,RP} = 2 \text{ m/s}^2$). And the HSAF (green dashed curves) with the estimated logarithmic mean (green curve) and a $\pm std$ | 63 |
| A.1 | Horizontal and Vertical Site Amplification Factors for engineering bedrock (grey lines) against the Horizontal and Vertical Site Amplification Factors for seismological bedrock (black lines) for each of the 152 stations | 88 |
| A.1 | Horizontal-to-Vertical Spectra Ratio of ambient noise (mHVSR) for 132 of 152 studied stations produced from Geopsy software. | 95 |



List of Tables

| | | |
|------|--|----|
| 4.1 | Initial parameter model for space exploration in the joint inversion procedure for reference station "AIG2". | 21 |
| 4.2 | Values of the best fit and final parameter model for ref. station "AIG2". | 21 |
| 4.3 | Initial parameter model for space exploration in the joint inversion procedure for reference station "ART2". | 23 |
| 4.4 | Values of the best fit and final parameter model for reference station "ART2". | 23 |
| 4.6 | Values of the best fit and final parameter model for reference station 'ATH5'. | 25 |
| 4.5 | Initial parameter model for space exploration in the joint inversion procedure for reference station 'ATH5'. | 25 |
| 4.7 | Initial parameter model for space exploration in the joint inversion procedure for reference station 'SEIS'. | 27 |
| 4.8 | Values of the best fit and final parameter model for reference station 'SEIS'. | 27 |
| 4.9 | Initial parameter model for space exploration in the joint inversion procedure for reference station 'SIA'. | 29 |
| 4.10 | Values of the best fit and final parameter model for reference station 'SIA'. | 29 |
| 4.11 | Initial parameter model for space exploration in the joint inversion procedure for reference station "VSK1". | 31 |
| 4.12 | Values of the best fit and final parameter model for reference station "VSK1". | 31 |



| | | |
|------|--|-----|
| 4.13 | Propagation path parameters results as derived by the simple attenuation model created to investigate the results from the two software under examination, 'HV-Inv' and Geopsy-Dinver. | 40 |
| 4.14 | Site categorisation according to the EC8 (CEN 2004[1]). | 58 |
| 4.15 | Standard site categorisation according to 2024 draft of EC8 | 61 |
| 4.16 | Site categorisation based on $V_{s,H}$ and f_0 according to EC8 2024 draft. | 61 |
| A.1 | Categorization of sites based on the peak Frequency f_p and peak Amplitude A_p of Horizontal-to-Vertical Spectral Ratios of Earthquakes (eHVSRS). This categorization was used for log-average Vertical Amplification Correction Functions (VACFs) calculation in each category and depicted in figure 4.22a. | 96 |
| A.2 | Categorization of sites based on the peak Frequency f_p and peak Amplitude A_p of Vertical-to-Horizontal Spectra Ratios of Earthquakes (eVH-SRS). This categorization was used for log-average Vertical Amplification Correction Functions (VACFs) calculation in each category and depicted in figure 4.22b. | 97 |
| A.3 | Log-average Vertical Amplification Correction Functions (VACFs) for all 152 stations used in the present study (figure 4.24). | 98 |
| A.4 | Fundamental frequency, f_0 , for all 152 stations. | 99 |
| A.5 | The longitude and latitude as well as the total records at the 152 stations used in the present study. | 100 |
| A.6 | Categorization of sites according to 2024 draft EC8, based on the standard categorisation shown in Table 4.15 (second column) and based on $V_{S,H}$ and f_0 categorisation shown in Table 4.16 (third column). The categories inside the parenthesis are based on the standard deviation of $V_{S,H}$ and f_0 | 102 |



Chapter 1

Introduction

Earthquakes as devastating natural disasters, emit seismic waves which propagate from the seismic source to the Earth's surface through different soil layers and have significant impacts on both natural and anthropogenic environment. The probability of considerable damages, especially in seismically active regions like Greece, renders seismic hazard assessment crucial, factor to evaluate the seismic risks on specific sites. Local geology conditions affect both horizontal and vertical components of seismic waves. The seismic ground motion is being influenced by three factors, namely the seismic source, the propagation path and the site properties. A key aspect of site properties evaluation is to efficiently estimate the Site Amplification Factor (SAF) as a function of frequency.

Various methods exist for estimating horizontal SAF (HSAF), each with its own advantages and limitations. For example, the approaches of Takahashi and Hirano, [80]; Aki, [4]; Kawase, [37]; Nagashima et al., [51], [50] rely on detailed geological borehole data and sensors installed on surface to accurately investigate the subsoil structure. However, this method faces challenges in calculating the shear wave velocities (V_s) down to seismological bedrock. Other empirical methods that involve the borehole spectral ratio method (eg. Steidl, [78]; Satoh et al., [75], Tao and Rathje, [81]) have limitations, such as the effects of reflected waves between the surface and the borehole sensors. In general, empirical methods that rely on data observed at reference sites located on hard rock are often challenging, mainly because of the definition of this site, as a true bedrock.

Prior research has highlighted the necessity to reliably estimate site factors in order to assess seismic hazard. The evaluation of these factors contribute to generation of ground-motion prediction equations (GMPEs), via regression analysis of recorded data. Recent studies (Rodriguez-Marek et al., [70]; Kotha et al., [46]) have upgraded the evaluation of seismic hazard at a specific site. However, relying solely on V_{S30}

proxy, which is insufficient to fully describe the frequency-dependent amplification due to the dynamic properties of soil (eg. Lee and Trifunac, [47]) demonstrated that V_{S30} is not a significant site parameter in empirical GMPEs aimed at predicting amplification of strong seismic motion.

During the last decades, the so called Generalized Inversion Technique (GIT) has been developed as an efficient tool in order to predict site ground motion and to better understand the three fundamental factors (seismic source, propagation path and site conditions). GIT allows the evaluation of empirical site response in frequency domain, especially in regions of low to moderate seismicity. First introduced by Andrews, [5] and then further applied by Castro et al., [20], Iwata and Irikura, [34], and Kato et al., [36], GIT is based on the assumption that Fourier Amplitude Spectra (FAS) on surface can capture the three fundamental factors: seismic source, propagation path, and site conditions at a region of interest.

Other studies have succeeded in further understanding seismic hazards assessment. Kawase and Matsuo, [40] used earthquake records to separately calculate the basic properties of the seismic source, propagation path, and site amplification by employing a well-established separation method to derive SAFs from spectral inversion and S-wave velocity (V_s) structures using the 1D wave propagation theory. Kawase, [38] examined high peak ground acceleration (PGA) records from the 2003 Tokachi-Oki earthquake the non-linearity of site effects and compared them to low PGA records. Driven by Kawase and Matsuo's, [40] study, Nakano et al., [58] calculated strong-motion factors (source, path, and site conditions) by a spectral inversion analyses for over 77,000 source-station pairs of records. To improve the evaluation of seismic site responses Klin et al., [44] introduced the *GITANES* Matlab package, a flexible and user-friendly tool for GIT and, particularly, useful for microzonation studies and site specific seismic hazard assessment. To determine parameters through iterative improvements Grendas et al., [27] applied a non-linear Gauss-Newton inversion method to greek accelerometric data. Building on this and in order to investigate the three fundamental factors mentioned above, Grendas et al., [29] presented a revised parametric GIT algorithm of Drouet et al., [22], which has been used in this dissertation.

Jeong et al., [35] applied GIT to analyse the source, path, and local site properties of 90 earthquakes in Fort Worth Basin, Texas, an induced seismicity region, utilising 66 temporary stations and based on low magnitude earthquakes. The results of that study presented great site amplification due to the sedimentary basin in the area and steady attenuation properties (γ , Q). On the other hand, in the western Sichuan region of China, Dang et al., [21] utilised GIT for 62 earthquakes with moderate to high magnitudes from $4.3 \leq M_w \leq 6.4$, from 55 strong-motion stations to determine the three aforementioned factors. Their results highlighted significant differences in SAFs derived from GIT and H/V methods. Trying to investigate the variability and reliability of different GIT implementations, Shible et al., [77] performed multiple

inversions on synthetic and real data.

Ito et al., [33] based on the Diffuse Field Assumption (DFA), employed GIT to review the development and validation of horizontal-to-vertical spectra ratio of earthquakes recordings (eHVSR) as a substitute for HSAF by suggesting a Vertical Amplification Correction Function (VACF), first proposed by Kawase et al. (2018) [42]. Maragkakis, [49], used data from 152 accelerometer stations and 8428 records from 368 earthquakes to determine a VACF for the greek area, based on Ito et al., [33] study. In this dissertation, based on the two aforementioned studies, VACFs were calculated, among others, for the same 152 stations as in [49], following the steps of Ito et al., [33], but fixed on greek data. Furthermore, in order to investigate differences or/and similarities between the horizontal-to-vertical spectra ratio of ambient noise and earthquake recordings for sites in Japan (mHVSR and eHVSR, respectively), Kawase et al., [41] proposed an empirical spectral ratio the, so called, earthquake-to-microtremor ratio (EMR), which was also calculated in this study.

The application of GIT for calculation of HSAFs at specific sites, as well as for site characterization and the estimation of VACFs, assumes the existence of Fourier Amplitude Spectra (FAS) data on the surface and the estimation of SAFs at the desired bedrock (seismological and/or engineering). Calculating these SAFs requires the development of 1D profiles of shear wave velocity with depth (V_{SZ} profiles). These V_{SZ} profiles are derived from the inversion of mHVSR method (Nakamura [52], [53], [55]) and dispersion curve data. Exploring the reliable application of mHVSR curve and dispersion curve, joint inversion based on DFA theory. Garcia-Jerez et al, [24] developed a software 'HV-inv' and tested it in real data in El Ejido town, South East of Spain (Garcia-Jerez et al., [25]).

Diffuse Field Assumption (DFA) proposed by Sánchez-Sesma et al., [71], [74]; Piña-Flores et al., [67] assumes that the ambient noise field consists of various wave types, including body waves (P- and S-waves) and surface waves (Rayleigh and Love waves), generated by natural and anthropogenic sources and propagate through the Earth's subsurface in all directions. In a diffuse field, wave energy reaches an equilibrium where the distribution of energy among different wave types is equipartitioned, while the equilibrium state allows for a reliable extraction of the Green's function from ambient noise recordings, as the noise field can be treated as statistically homogeneous and isotropic. DFA has been proven to be valid up to seismological bedrock. In the present study, the validity of the DFA theory for engineering bedrock is assumed, as well.

As already mentioned, for seismic hazard assesment the local site condition investigation is crucial. Local geology properties and V_s contrast between layers, affect amplification of upgoing seismic waves from bedrock to surface —the greater the contrast, the higher the amplification. Modern seismic codes have adopted this relationship for site characterization based on V_s . A simple and straight forward site

categorization, based on V_{S30} was established by Part 1 of Eurocode 8 (EC8-1, [1]), proposing five standard ground types: A, B, C, D, and E. Alternative parameters according to EC8-1 such as the number of blows of the Standard Penetration Test of 30cm thickness (NSPT) and the undrained shear strength of soil (c_u). However, V_{S30} cannot capture the complexity of site amplification effects as many researchers have pointed out (e.g., Castellaro et al. [19]; Gallipoli and Mucciarelli, [23]; Lee and Trifunac [47]). To address these issues and with the primary objective of reducing soil type categorisation uncertainties, the EC8-1 criteria were reassessed and improvement was made in elastic design spectra in the draft version of Eurocode 8. Site categorization was achieved using two new proxies related to seismic hazard: the depth of engineering bedrock, $H_{0.8\text{km/s}}$, and the corresponding shear wave velocity, $V_{S,H}$. Paolucci et al. [64] conducted empirical analyses using European and Japanese strong motion datasets to evaluate the site categorization and site amplification factors (SAFs) in the 2024 draft of Eurocode 8. The present study builds on old and new refined criteria by utilising Horizontal Site Amplification Factors (HSAFs) derived from the Generalized Inversion Technique (GIT) after classifying 152 sites of accelerometer stations used, according to both the current EC8 and the 2024 draft version.



Chapter 2

Methodology

The methodological approach employed in this study is outlined through a schematic representation in Figure 2.1, presenting the sequential steps undertaken. In a first step the data set of horizontal-to-vertical spectra ratio of ambient noise (mHVSRS) and Dispersion Curves (DCs) were acquired. The data of six scattered reference stations in Greece were, previously, measured and exploited within the study conducted by Theodoulidis et al. (personal communication, 2024), in order to construct the V_{SZ} profile models for each station. The 1D theoretical site spectral amplification factors, $SAF_s^{theoretical}$, for the two sets of V_{SZ} profile models at the reference stations were calculated, to investigate similarities and differences between the two different methods used, for two cases; (a) with respect to engineering bedrock and (b) with respect to seismological bedrock. The engineering bedrock is considered as the depth where shear wave velocity reaches 0.8 km/s, while the seismological bedrock is where shear wave velocity reaches 3 km/s. A crucial step before the Generalized Inversion Technique (GIT) application was the deconvolution (correction) of the observed Fourier spectra on the surface to the spectra in the desired bedrock, by implementing the $SAF^{theoretical}$ results using two different software packages, 'HV-Inv' and Geopsy-Dinver. During GIT, an homogeneous attenuation model in the examined region was initially adopted for all available scenarios, so that a comparison between the results is feasible and reliable. Subsequently, an inversion with a spatially heterogeneous attenuation model was carried out, in order to calculate the desirable factors for depths $H_{0.8\text{km/s}}$ and $H_{3\text{km/s}}$. The results for seismic source, propagation path, and site factors (SAFs) were examined, and the corresponding Vertical Amplification Correction Functions (VACFs) were calculated for all stations used in this study (152 in total), as well as the vertical-to-horizontal spectral ratio (V_bH_bR) at the six reference sites, both for engineering and seismological bedrock.

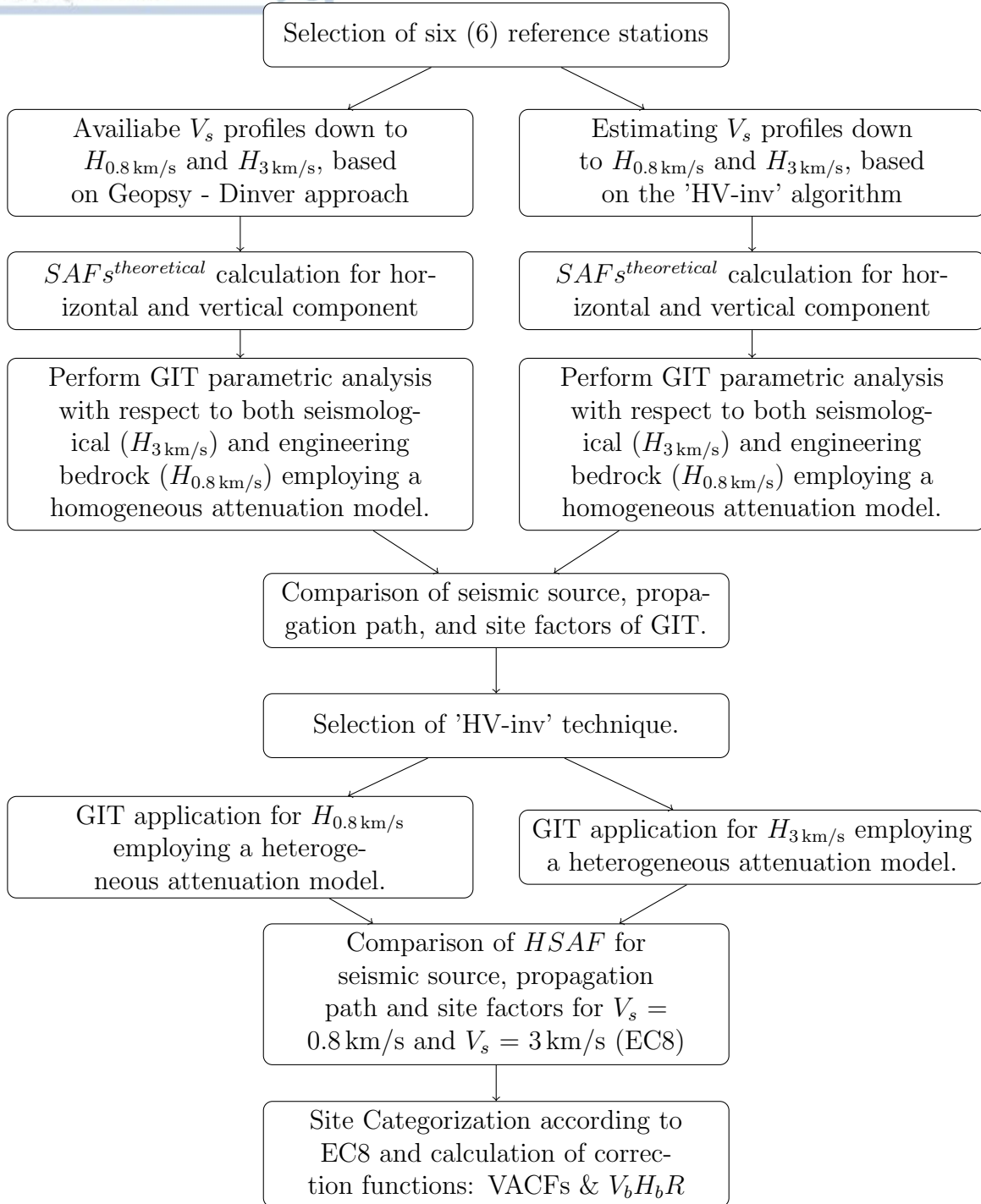


Figure 2.1: A schematic flowchart that shows the steps of this thesis.

2.1 Inversion of HVSR spectral ratios and Dispersion Curves under the Diffuse Field Assumption

2.1.1 Horizontal-to-Vertical Spectral Ratio technique (HVSR)

The Horizontal to Vertical Spectral Ratio (HVSR) technique, pioneered by Nogoshi and Igarashi [60], [61], [62] suggested that microtremors were mostly composed of Rayleigh waves. This technique was popularised by Nakamura ([52], [53], [54], [55], [56], [57]) who concluded that microtremors consist not only of surface waves, but also body waves and changed radically the way that seismic site effects can be evaluated. The HVSR technique offers a relatively simple but yet effective tool for understanding site response due to seismic excitation. HVSR entails the estimation of the site period or fundamental frequency (f_0), through ambient noise (microtremor) recordings analysis of a site. At the same time, HVSR efficiently provides insights into the amplification potential of seismic waves due to local geology and in general certain dynamic characteristics of soil, whereas is applicable in regions even with low seismicity. Nakamura ([52], [53], [55]) suggested that, the fundamental frequency, f_0 , as well as the amplification of the seismic motion, A_0 , can be calculated via HVSR, regardless the impact of Rayleigh waves dominating the seismic signals. Also, from the f_0 and the average shear wave velocity (V_s) of sedimentary layers overlying the rock whose depth (H) can be estimated from equation: $H = V_s/4 \cdot f_0$.

HVSR technique, also known as Quasi-Transfer Spectra (QTS) method, in sedimentary basins (figure 2.2), aids in understanding the energy distribution of both body and surface waves. On the surface of the sedimentary basin, the horizontal spectra, H_f , and vertical spectra, V_f , could be defined as:

$$\begin{aligned} H_f &= A_h \cdot H_b + H_s \\ V_f &= A_v \cdot V_b + V_s \end{aligned} \quad (2.1)$$

where H_b and V_b are the corresponding horizontal and vertical spectra on the bedrock basin, A_h and A_v are the amplification factors of the vertically propagating body waves, and H_s and V_s are the spectra of the horizontal and vertical motion, of the Rayleigh surface waves, respectively (Nakamura [55]). The QTS equation for the

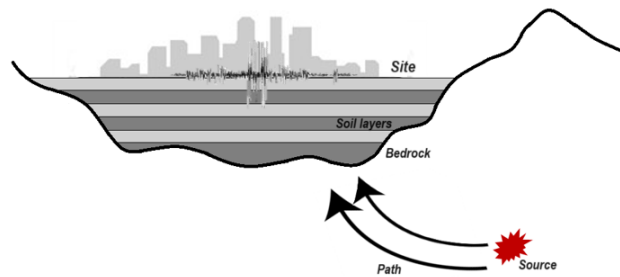


Figure 2.2: Illustration of the source of waveform, the path and the site effects in sediment formations.

sedimentary basin that is dominated by both kind of waves is:

$$QTS = \frac{H_f}{V_f} = \frac{A_h \cdot H_b + H_s}{A_v \cdot V_b + V_s} = \frac{H_b}{V_b} \left[\frac{A_h + \frac{H_s}{H_b}}{A_v + \frac{V_s}{V_b}} \right] \quad (2.2)$$

On rock formation, H_b/V_b is considered equal to 1, for frequencies 0.2 to 20 Hz. If the amount of surface waves is very low and body waves are dominant, then it is considered that $H_s = V_s = 0$ and $QTS = A_h/A_v$. On the other hand, when Rayleigh waves influence significantly the ground motion then $A_h = A_v = 0$ and $QTS = H_s/V_s$.

2.1.2 Dispersion Curves

The horizontal component of seismic motion includes both Rayleigh and Love surface waves, whereas only Rayleigh waves affect the vertical component. Analysis on surface waves usually focuses on the vertical component, leading to primarily portrait the dispersion characteristics of Rayleigh waves. Produced by surface waves, dispersion curves play a crucial role in understanding the properties of seismic waves propagation across different surface layers on earth, since they depict the variation of seismic wave velocity with frequency. These curves are decisive in providing detailed insights into the subsurface layering and geophysical properties of geological formations. The velocity of surface waves (Rayleigh, Love waves) depends on the frequency and mechanical properties of the strata. Low-frequency waves tend to penetrate deeper and are, consequently, influenced by properties of deeper layers, while higher-frequency waves are affected by the shallower sedimentary strata. By analyzing the variation of surface wave velocity with frequency, it's possible to infer critical information about the subsurface structure, including layer thickness, shear wave velocity, as well as other geophysical properties.

Passive data accumulation, from which dispersion curves could be calculated, can be measured using a variety of geophysical methods such as the Multichannel Analysis of Surface Wave (MASW) (Park et al. [65]), the High-Resolution Frequency-Wavenumber (f-k) Method ((Capon, [18], Asten and Henstridge, [8], Wathelet et al., [87]), the spatial autocorrelation method (SPAC) (Aki, [3], Ohori et al. [63], Roberts and Asten, [69]), among others. In the present study, the dispersion curves of the surface waves have been extracted using the MASW, an active seismic method.

2.1.3 Inversion under the Diffuse Field Assumption (DFA)

The aforementioned techniques are a cornerstone in the analysis of subsurface structures, in shear wave velocity (V_{SZ}) profiles generation, which are crucial for site

response estimations at a target site, especially in engineering seismology. Data consisting of HVSR and Dispersion Curves were sourced from the research conducted by Theodoulidis et al. (personal communication, 2024), in which measurements were conducted at six station sites in Greece, considered as “rock” reference sites. According to Steidl et al., [78] reference site response as a half-space, i.e. a site with amplitude close to one, howbeit, as it is emphasised in that study, every site has a different response associated its geology. Local geology could be responsible for many ‘rock’ sites displaying amplification factors with higher amplitude values.

Both, HVSR and dispersion curve can be used in the inversion analysis. The simplicity, non-invasiveness, cost-effectiveness, and efficiency of the HVSR technique, particularly its capacity to unveil the fundamental frequency (f_0) of surficial geological formations, lead to a deeper exploration of how seismic waves interact with local geological features, through the analysis of ambient noise measurements. While HVSR provides the f_0 of surface layers, array-based techniques (MASW, AVA) offer a more detailed picture of the variation of elastic parameters in 1D deeper structures, complementing the information obtained from HVSR with Dispersion curve. The combination of these two methods allows for a deeper understanding of the behavior of seismic waves and, also, site response under seismic excitation. Integrating both approaches in a combined inversion framework enhances resolution in lower frequency ranges and is particularly effective to accurately determine interfaces of deeper geologic layers. A suited framework for modelling is the Diffuse Field Assumption (DFA), proposed by Sánchez-Sesma et al., [73], and Piña-Flores et al. [67].

The DFA relies on diffuse field illumination, characterised by multiple scattering phenomena, leading to the theory that ambient noise wavefield consists of all types of body and surface waves (Sánchez-Sesma et al., [74]). It is accepted that the fundamental frame of DFA is that all type of seismic wave (body and surface) contributes to the overall energy due to the equipartition of energy. This assumes that the energy is distributed equally through a homogeneous crust, while this assumption may not be totally valid for the overlying heterogeneous formations. Furthermore, the DFA theory proposes that, within a diffuse elastic wavefield, the autocorrelation in the frequency domain is proportional to the imaginary part of Green’s function when the source and receiver are in the same position (Sánchez-Sesma et al., [71], [73]; Pertou et al, [66]). The later highlights the practicality of this assumption in HVSR understanding, which can be expressed in terms of directional energy densities (DEDs), that are subsequently linked to the imaginary component of the Green’s functions. Equation 2.3 (Sánchez-Sesma et al., [72]) links the ‘average’ measurements stated on the left part of 2.3 with an intrinsic property of the medium on the right part of equation, showing the possibility of mHVSR inversion taking into consideration all

types of body and surface waves.

$$\begin{aligned}
 [H/V](\omega) &= \sqrt{\frac{E_{EW}(\chi, \omega) + E_{NS}(\chi, \omega)}{E_{\nu}(\chi, \omega)}} \\
 &= \sqrt{\frac{Im[G_{11}(\chi, \chi; \omega) + Im[G_{22}(\chi, \chi; \omega)]]}{Im[G_{33}(\chi, \chi; \omega)]}}
 \end{aligned} \tag{2.3}$$

The DEDs of the horizontal components are E_{EW} and E_{NS} , while for the vertical component is E_{ν} according to Arai and Tokimatsu, [7]. The inversion of HVSR curve, in this study, was achieved with 'HV-Inv' software (Garcia-Jerez et al, [24].) This software, also, allows for a joint inversion of mHVSr and Dispersion Curve data.

2.2 Theoretical Site Spectral Amplification Factors ($SAFs^{theoretical}$)

According to DFA, within the crust, while the waves undergo multiple scattering, all the way from the source to the target site, there is an equal distribution of energy among the 3 components. In order to characterize the site effects, it is crucial to understand the impact of the uppermost sedimentary layers on body waves as they are reflected and refracted when reaching the interface between the homogeneous half space (crust) and the sedimentary layers. A crucial method in this analysis involves the use of Transfer Functions, TF s, the spectral ratio and the phase difference between the surface and the bedrock, which quantify the amplification or deamplification of the bedrock seismic motion per frequency, as it interacts with the uppermost geological layers.

Generally, TF s are widely used in Seismology to describe how seismic ground motion varies at different depths within geological layers. Despite their importance, due to the mathematical complexities of TFs they are limited to simple scenarios involving only two or three layers. This lack of comprehensive knowledge, particularly regarding the impact of adding more layers, impedes advancement in certain research areas, compelling scientists to rely on costly analyses.

Kawase et al. [39] calculated the theoretical eHVSr based on DFA at the surface ($z = 0$) of seismic motion in to transfer function as:

$$eHVSr = \frac{H(0, \omega)}{V(0, \omega)} = \sqrt{\frac{Im[G_{horizontal}^{Eq}(0, 0; \omega)]}{Im[G_{vertical}^{Eq}(0, 0; \omega)]}} = \sqrt{\frac{\alpha_H}{\beta_H} \frac{TF_{horizontal}(0, \omega)}{TF_{vertical}(0, \omega)}} \tag{2.4}$$

where G^{Eq} is the Green's function for seismic source, ω is the circular frequency, α_H is the velocity of the P-wave in half-space, and β_H is the S-wave velocity and $TF(0,\omega)$ is the transfer function of the corresponding body wave. By studying 2.4, the importance of taking into consideration the entire basin structure, extending all the way to the seismological bedrock arise, since the eHVSr depends on the ratio α_H/β_H and the TF s of body waves from bedrock to surface. In present study, it was performed only the calculation of the spectral ratio component of the TFs, thereby determining the 1D theoretical Site Amplification Factors, denoted as $SAFs^{theoretical}$, after the extraction of V_{SZ} profiles, using the 'PSVSH-1D' software (Bard P.-Y., personal communication, 2024) and is followed by the deconvolution of observed on surface Fourier amplification spectra of earthquake records.

2.3 Generalized Inversion Technique (GIT)

Determining Site Amplification Factors (SAFs) at the surface of a site is essential in assessing the site response in case of seismic excitation. The Generalized Inversion (GI) is a pivotal methodology in investigating, simultaneously three fundamental factors forming seismic ground motion, namely, seismic source, propagation path, and empirical site TF. The method of GIT was proposed and, initially, applied by Andrews [5], who applied a non-parametric method where the source and site parameters are calculated after the correction of attenuation path considering only the geometrical factor, followed by Iwata and Irikura,[34] and Castro et al. [20]. The latter incorporated the additional element of the inelastic losses of ground motion into the attenuation term. GIT allows the steady calculation of SAFs, with respect to the surface projection of the seismological bedrock at a reference site, in well studied areas where numerous earthquakes are observed.

The application of GIT analysis requires ground motion data from numerous earthquakes observed at many sites. However, for optimal utilization of GIT, moderate to large earthquakes are essential, as these allow for more precise determination of magnitude, source locations and longer propagation paths. Within this framework of GIT, the Fourier Amplitude Spectra (FAS) of the horizontal component of S-waves portion, Fs_{ij} of an observed earthquake i at a site j , are defined by the following equation:

$$\log(Fs_{ij}) = \log(Ss_{.i}) + \log(Ps_{.ij}) + \log(Hs_{.j}) \quad (2.5)$$

where $Ss_{.i}$ is the sum of the source term of an earthquake, $Ps_{.ij}$ the propagation path term and $Hs_{.ij}$ (HSAF, general term for the site amplifications in the horizontal direction) is the horizontal site amplification factor for the S waves. Equivalently,

Gs_{ij} is the vertical motion of S waves in FAS on the surface given by:

$$\log(Gs_{ij}) = \log(Ss_{ij}) + \log(Ps_{ij}) + \log(V_b H_b R) + \log(Vs_{ij}) \quad (2.6)$$

where Vs_{ij} (VSAF , general term for the site amplifications in the vertical direction) is the vertical site amplification factor for the P waves. $V_b H_b R$ is a correction coefficient that can convert the horizontal (S-waves) amplitude into vertical (P-waves) amplitude and it is deemed to correspond to the inverse of the $H_b V_b$ ratio of the incident waves at the seismological bedrock, according to the DFA regime. According to equation 2.6, it is assumed that the seismic motion propagates in the form of shear waves and transforms into primary waves just below the observation site.

From equations (2.5) and (2.6) the observed on surface (s) eHVSR is given by:

$$sEHVSR = \left\langle \frac{Fs_{ij}}{Gs_{ij}} \right\rangle = \left\langle \frac{Hs_{ij}}{Vs_{ij} \cdot V_b H_b R} \right\rangle \quad (2.7)$$

while sHSAF is expressed as:

$$sHSAF = \left\langle Hs_{ij} \right\rangle = sEHVSR \cdot \left\langle Vs_{ij} \cdot V_b H_b R \right\rangle \quad (2.8)$$

the $\langle \rangle$ symbol represents the logarithmic average operation. Ito et al.[33] from the last formula of equation (2.7) have determined a Vertical Amplification Correction Function, VACF, representing the logarithmic mean of the spectral ratio between the vertical amplitude at the ground surface and the horizontal amplitude at the outcrop of the seismological bedrock and it is calculated by the simple equation:

$$HSAF = eHVSR \times VACF \quad (2.9)$$

The GIT algorithm employed in this study is developed by Grendas et al.[29], which leverages a parametric approach that incorporates the distance- and region-dependent attenuation parameters related to geometrical spreading and anelastic attenuation effects. The foundation of the GIT algorithm is based on the Gauss-Newton iterative inversion method, which allows a simultaneous inversion of the seismic moment and corner frequency against stress drop, while investigating in the frequency domain, the seismic source, propagation path, and site properties. Furthermore, using the same dataset the algorithm implemented allows the simultaneous generalized inversion for horizontal and vertical component.

The algorithm hinges on solving a system of equations generated from the logarithmic values of the S wave Fourier spectra, z_{ijk} , from recordings of earthquakes, i and stations j , for k frequencies (eq.2.10)

$$z_{ijk} = m_{0_i} - \log_{10}\left[1 + \left(\frac{f_k}{f_{c_i}}\right)^2\right] - \gamma(r_{ij})\log_{10}(r_{ij}) - \sum_1^n \frac{\pi r_{ij} f_k}{\ln(10) Q_{sn} f_k^{\alpha_n} v_{sn}} + s_{jk} \quad (2.10)$$

where $m_{0_i} = \log_{10}(M_{0_i} \times \frac{2R_{\theta\phi}}{4\pi\rho\beta^3})$, in which M_0 the seismic moment, $R_{\theta\phi}$ the source radiation pattern, which is equal to 0.55 (Boore and Boatwright, [10]), $\beta = V_s = 3.5$ km/s the average S wave velocity in the crust, $\rho = 2800$ kg/m³ the average density and $s_{jk} = \log_{10}(S_{jk}(f_k))$, in which $s_{jk}(f_k)$ the distance- and frequency-dependent site spectral amplification. Furthermore, in eq. 2.10, f_c is the corner frequency, r_{ij} the hypocentral distance, while γ the geometrical spreading attenuation factor. $\gamma(r_{ij})$ as the distance-dependent geometrical spreading attenuation factor, contributes to the advancement of the inversion results. n represents every cell in the region of interest and factor Q_{sn} is the S wave quality factor for the corresponding cell and parameter α_n which sets dependence of the quality factor on frequency.

Every term of eq.(2.10) refers to a different factor, the first two terms represent the seismic source, the third and fourth term are related to the propagation path, while the last one is linked with the site characteristics. For each earthquake analyzed in 2.10, an equivalent number of supplementary equations are integrated into the equation system. These additions are implemental in modulating the interaction between the seismic moment and corner frequency for each earthquake, which is achieved through the application of Brune's stress drop, $\Delta\sigma$, formula (Brune, [17], [16]):

$$\Delta\sigma_i = \frac{7}{16} M_{0_i} \left(\frac{f_{c_i}}{0.37\beta}\right)^3 10^{-5} \quad (2.11)$$

where β is the S wave velocity.

In general, through this iterative process, an initial, reasonable set of parameter models is facilitated, aiming to minimize the misfit and achieve a stable solution. To ensure consistency, GIT have been applied concurrently to both the horizontal and vertical components (Ito et al. [33]).



Chapter 3

Data Used

This chapter is dedicated to the description of the data used in this study. The site characterization method analyzed in Chapter 2.1, was applied to six (6) reference stations that according to geological conditions were classified as "rock" sites. The geophysical data were obtained after conducting measurements at classified rock sites across Greece. Additionally, this chapter outlines the criteria used to compile the observed Fourier Amplitude Spectra (FAS) dataset. Finally, it describes the process applied to determine the fundamental frequency, f_0 , for all stations included in the FAS catalogue.

3.1 HVSR and Dispersion Curve data

The accelerometric network employed in this study is part of the Hellenic Unified Seismological Network (HUSN) and is mainly operated by the Institute of Engineering Seismology and Earthquake Engineering (ITSAK) as well as the Geodynamic Institute of the National Observatory of Athens (GEIN-NOA). Theodoulidis et al., [83], performed geophysical measurements within a proximity of less than 100 meters from accelerometric stations of the HUSN network, where the V_{S30} were estimated to be equal to or greater than 800 m/s. Prior to this study ([83]), these stations were classified as rock sites according to geological maps provided by I.G.M.E. (Institute of Geology and Mineral Exploration). Additionally, HSAFs and HVSRs measurements from previous studies by Grendas et al. ([27], [29]), Maragakis [49], and Theodoulidis et al. [84], helped establish the criteria of stations located on rock formations (reference stations). These criteria include, firstly, a predominantly flat HVSR amplification and, secondly, a low average spectra amplification within a selected frequency range.

Among the total of 17 stations that met one or both of the aforementioned specified criteria, six were chosen for site characterisation, which will be referred to as reference stations. These include 'AIG2' (Aigion, 38.2417, 22.0726), 'ART2' (Arta, 39.1474, 20.99368), 'ATH5' (Athens, 37.9754, 23.7371), 'SEIS' (Thessaloniki, 40.6318, 22.9628), 'SIA1' (Siatista, 40.2573, 21.5534), and 'VSK1' (Vasilikiades, 38.4091, 20.5640). Geological maps of the accelerometric stations classified the geologic formations into five time periods: Holocene, Pleistocene, Quaternary undivided, Tertiary, and Mesozoic/Paleozoic, as delineated by Stewart et al., [79].

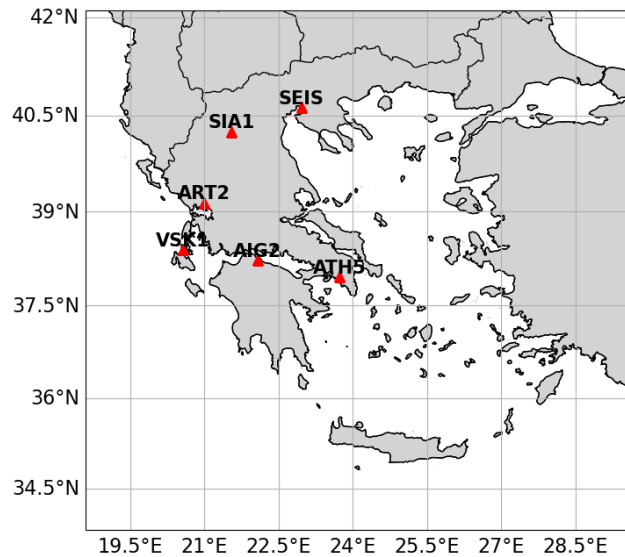


Figure 3.1: Map of reference station locations

Geophysical and seismic measurements were conducted at a distance less than 100m from the aforementioned stations, aiming to obtain the geophysical data, i.e. the dispersion and mHVSR curves. Both the Multichannel Analysis of Surface Wave (MASW) method and the Ambient Vibration Array (AVA) method, were performed during the study of Theodoulidis et al., [83]. MASW is an active method that allows the analysis of the surface waves dispersion, by using linear arrays to record the S-waves. Data of MASW method were used to generate the experimental dispersion curves. While AVA geophysical passive method is a non-invasive seismic technique, based on ambient noise measurements by deploying a network of seismographs around the site of interest. This method was used to acquire the mHVSR data, at all six sites within a frequency range of 0.3 Hz to 30 Hz. With an exception of the SEIS and SIA1 stations, for the rest of them the mHVSR curves emerge flat with their amplitude not exceeding two. With passive geophysical methods the low-frequency information can be captured, whereas, active geophysical methods focus on high-frequency. However, there are challenges with obtaining low-frequency data because the vertical component often diminishes, resulting, some of the dispersion curves samples to begin at higher frequencies while others start at lower frequencies

3.2 Fourier Amplitude Spectra of S-waves

Maragkakis, [49], created a catalogue of earthquakes recorded by accelerographs belonging to the HUSN, with magnitude $M \geq 4$, for 3 time periods: 1973-1999, 2000-2009 and 2010-2018. The final catalogue consisted of 20517 waveforms, corresponding to 772 seismic events, recorded at 262 stations all over Greece, with moderate magnitudes, ranging from 4 to 7, and focal depth $H \leq 40$ km.

In this study, were used only earthquakes whose hypocentral distances did not exceed 300 km ($R_{hyp} \leq 300$ km), after picking of P and S wave arrival times. However, in order to compile the Fourier Amplitude Spectra dataset for S-waves, used in the generalized inversion approach later, further criteria were imposed. Earthquake records were chosen with magnitude ranging from $4 \leq M < 6$ to conform with the point source model established by Brune, [17] and for focal depth $H \leq 40$ km. The hypocentral distance is constrained between $12 \leq R_{hyp} \leq 300$ km, because in case of large hypocentral distances and big magnitude earthquakes were included, the data records would be duplicated. Lastly, the Peak Ground Acceleration, PGA, was limited below or equal to 200 cm/s^2 . The records selected had all three component data complete and exhibited ambient noise before P-wave arrivals. Moreover, each seismic event should have been recorded in, at least, three stations, and each station should have a minimum of three earthquake records. Implementing all conditions above, resulted in a catalogue of Fourier Amplitude Spectra of S-waves from 372 earthquakes recorded at a total of 152 stations.

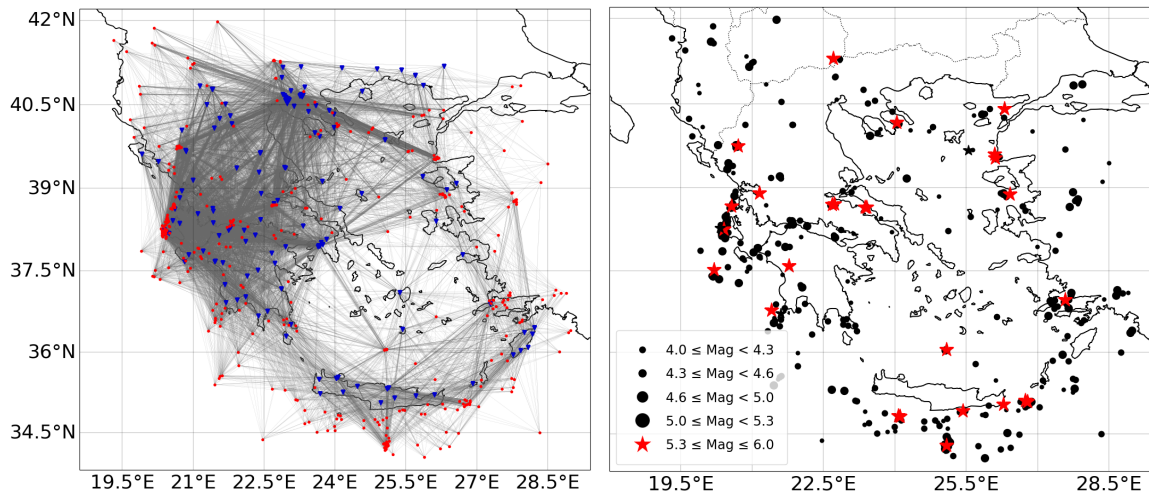


Figure 3.2: Map showing the earthquakes selected for this study (right) as well as the ray paths (left) derived between the hypocenters (red) and the recording stations (blue).

The study area is defined by a longitudinal range from 18.26° to 29.40°E and a latitudinal range of 33.80° to 42.20°N . The map in figure 3.2 (left) displays the ray paths between the hypocenter and the station of each earthquake. In the right part of the same figure (3.2) the selected earthquakes are shown in terms of their magnitude.

3.3 Fundamental Frequency Analysis to Estimate Bedrock Depth

As previously mentioned in 3.2, a total of 152 stations installed all over Greece were utilized, in order to determine their fundamental frequency, f_0 , to calculate their depth range, stemming from the equation: $H = V_s/4 \cdot f_0$, where H represents the depth down to bedrock and V_s the average shear waves velocity of the overlying soil layers.

For these calculations, ambient noise data were utilized, sourced from accelerographs operated by the Institute of Engineering Seismology and Earthquake Engineering (I.T.S.A.K.) and the HUSN network, from in-situ measurements by a 24 bits digitizer CityShark coupled with LE3D 5sec seismometer as well as from the Horizontal-to-Vertical spectral ratio from earthquake recordings (eHVSR). From the eHVSR data only time windows selected that captured surface waves and ambient noise. Overall, accelerometers were employed at 116 stations, velocimeters at 21 stations, and eHVSR data were used at 15 stations to obtain the mHVSR or eHVSR curves. Time windows of minimal anthropogenic noise were selected for the waveforms from the accelerometer stations, with a total duration of 60 minutes. On the contrary, time duration of velocity-sensitivity instruments ambient noise measurements was 30 minutes. While, for the stations relying solely on eHVSR data all available waveforms were used to derive an average curve ± 1 std.

Analysis of these waveforms was conducted using the open-source software Geopsy [2], dedicated for signal display and processing. Due to the varied duration of waveforms, the window lengths for the analysis also differed: 80 to 120s for accelerometer data, 40 to 80s for data from velocity-sensitivity instrument. However, in both methods according to the reliability criteria, a consistent relationship is applied according to the SESAME guidelines: $n_s = I_w \cdot n_w \cdot f_0$, where n_s is the number of significant cycles, I_w is the windows length and n_w is the number of windows selected for averaging the HVSR curve. While for the eHVSR data the windows length are quite narrow ranging from 25 to 50s, the waveforms were sufficient to get a reliable average f_0 value. All other parameters set in GEOPSY, such as: anti-triggering on filtered signals, smoothing type and constant, window type, among others, remained consistent for each type of waveforms.



Chapter 4

Data processing and results

Chapter 4 is dedicated in describing the steps and the final results of each method used as analysed in Chapter 2. The first step was the joint inversion of HVSR and dispersion curve data for six stations installed on surface 'rock' formations, followed by computing their spectral amplification factors from the derived 1D- V_{SZ} profiles. Additionally, the spectral amplification factors from an alternative approach (Geopsy - Dinver) were estimated, enabling a comparative analysis of the 1D theoretical Site Amplification Factors for the six reference stations ($SAF_s^{theoretical}$) generated through each technique. Next step was the correction (deconvolution) of the observed Fourier Amplitude Spectra (FAS) of earthquake recordings on the surface, down to the seismological and engineering bedrock, where V_s equals 3 km/s and 0.8 km/s, respectively. The deconvoluted FAS were used as input to the Generalized Inversion (GI), from which the three fundamental factors of seismic source, propagation path, and site effect have been calculated. The empirical Site Amplification Factors (SAFs) originated from the Generalized Inversion Technique (GIT) application, were estimated for 152 stations of the accelerometric network of HUSN, were grouped according to the current Eurocode 8 and the 2024 draft of Eurocode 8 (EC8). Additionally, the SAFs computed for the horizontal (HSAFs) and vertical (VSAFs) components were employed in the Vertical Amplification Correction Functions (VACFs) estimation. The latter can be used to blindly estimate the HSAF, based directly on eHVSR. Finally, the Earthquake-to-Microtremor Ratio (EMR) was calculated based on the previously determined eHVSR and mHVSR at the 152 stations, as well as the $V_b H_b R$ (VHSR) coefficient. The $V_b H_b R$ coefficient is taken into account for the conversion of the horizontal (S-wave) amplitude into vertical (P-wave) amplitude, aiming at a three-stage correction of the easy measured mHVSR in order to derive the HSAF at a specific examined target site.

4.1 Joint Inversion of mHVSR and Dispersion Curve

An open-source program named 'HV-Inv' developed by Garcia-Jerez et al. [24] has been employed for the joint inversion of ambient noise HVSRs and Dispersion Curves (DCs), to generate 1D V_{SZ} profiles. The software, 'HV-Inv', is designed for both forward modeling and inversion operations, while supporting the joint inversions of mHVSR and dispersion curve. This inversion is based on the Diffuse Field Assumption (DFA) theory, which exploits the newly established correlation between HVSR of ambient noise and the elastodynamic Green's function.

4.1.1 'HV-Inv' algorithm for 1D V_{SZ} profiles

HV-Inv code is written in Matlab[®] and offers a diverse selection of both global (heuristic) inversion techniques, as well as local inversion methods. The three main global inversions are Monte Carlo Sampling (MSC) [32], Simulated Annealing method (SA) [43], and Modified Simulated Annealing (MSA) [48], while the local inversion methods include Interior Point (IP) [86] and Simplex Downhill (SD)[59]. The software, also, allows both independent and joint inversion of mHVSR and dispersion curve. In general, joint inversions yield models with greater constraints and offer genuine sensitivity to velocity values, by enabling the resolution of frequency bands, leading to more efficient detection of deeper subsurface formations. However, it is essential to acknowledge that parametric analysis has indicated instances where misfits exhibit more pronounced minima for joint inversion, although misfits naturally tend to rise with an increased volume of data, resulting higher misfit values, which are defined of a model m by equation 4.1.

$$\begin{aligned}
 misfit(\mathbf{m}) = & \frac{1}{2n} \sum_{i=1}^n \frac{(HVSR_{obs}(\omega_i) - HVSR_{th}(\omega_i, \mathbf{m}))^2}{\sigma_{HVSR}^2(\omega_i)} \\
 & + \frac{1}{2m} \sum_{i=1}^m \frac{(c_{obs}(\omega_i) - c_{th}(\omega_i, \mathbf{m}))^2}{\sigma_c^2(\omega_i)}
 \end{aligned} \tag{4.1}$$

where n and m are the number of samples for the HVSR and the dispersion curve, respectively. HVSR stands for horizontal-to-vertical spectra ration, c is the phase velocity and σ_c and σ_{cHVSR} is the standard deviation of c and HVSR, respectively, whereas subscripts *obs* and *th* stands for observed and theoretical, respectively.

In order to identify the parametric model of the investigated site that best represents the data, many parameter models have been examined, specifying details such as the number of layers, their thickness, velocities (V_P and V_S), densities and the

Poisson ratio. Given the rock nature of the sites under examination, these models were tailored accordingly. The first step was to generate a model derived by analyzing the mHVSr curve, curve in order to estimate the fundamental f_0 .

Based on this value of f_0 and the equation 4.2, a range of thickness or velocities can be estimated, depending on which of them is presumed.

$$H = \frac{V_s}{4 \cdot f_0} \quad (4.2)$$

Therefore, knowing the fundamental frequency (f_0) and specifying a shear wave velocity range, a corresponding range of thickness values can be ascertained, contrariwise, by defining a range of thicknesses, the corresponding velocity range could be estimated. In instances where the aforementioned method could not achieve a satisfactory joint inversion, random models were created, featuring various layers and a broad spectrum of parameters, aiming to systematically converge towards an optimal model.

4.1.2 V_{SZ} profiles generation for the reference stations

The first reference station, 'AIG2', is located in the General Hospital of Aigio, Peloponnese, in the Gulf of Corinth. This area is one of the most seismically active regions in Greece and Europe. According to Apostolidis et al. [6], the geological composition of the region includes two top thin layers of superficial deposits from the Holocene era, consisting of clays, gravels, and clayey sand and low V_s values ranging between 100 and 500 m/s. Underneath, there's a layer approximately 30 to 40 m thick, characterized by recent coastal deposits, followed by a layer of conglomerates, which is distinguished by higher V_s , exceeding 0.8 km/s. Therefore, from geological point of view the station lies at the interface where Holocene formations meet the Pleistocene deposits, meaning that a distinct contrast is expected in the V_s model.

The fundamental frequency is indistinguishable from the experimental HVSr curve, whose amplitude varies from 1.2 to 2, throughout the frequency range and therefore no further information can be inferred about the deeper structure. Table 4.1 shows the best parameter model that was adopted, derived after repeated inversions before concluding in the best-fit model shown in Table 4.2.

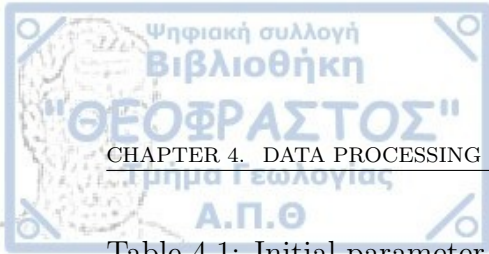


Table 4.1: Initial parameter model for space exploration in the joint inversion procedure for reference station "AIG2".

| Layer | Thickness (m) | V_p (m/s) | V_S (m/s) | Density (kg/m ³) |
|-----------------|-----------------|-------------------|-------------------|------------------------------|
| 1 st | 1.00 - 3.00 | 500.00 - 1000.00 | 300.00 - 600.00 | 1500.00 - 2000.00 |
| 2 nd | 5.00 - 10.00 | 800.00 - 1600.00 | 400.00 - 900.00 | 1500.00 - 2100.00 |
| 3 rd | 20.00 - 30.00 | 1000.00 - 2000.00 | 600.00 - 1000.00 | 1600.00 - 2200.00 |
| 4 th | 300.00 - 400.00 | 1500.00 - 4500.00 | 1000.00 - 2500.00 | 1700.00 - 2400.00 |
| 5 th | 320.00 - 380.00 | 2000.00 - 5000.00 | 1000.00 - 2500.00 | 1800.00 - 2500.00 |
| Half-space | - | 3500.00 - 6100.00 | 2000.00 - 3500.00 | 2000.00 - 2700.00 |

Table 4.2: Values of the best fit and final parameter model for ref. station "AIG2".

| Layer | Thickness (m) | V_p (m/s) | V_S (m/s) | Density (kg/m ³) |
|-----------------|---------------|-------------|-------------|------------------------------|
| 1 st | 2.70 | 735.00 | 425.00 | 1995.00 |
| 2 nd | 7.20 | 1090.00 | 630.00 | 2100.00 |
| 3 rd | 22.30 | 1335.00 | 770.00 | 2200.00 |
| 4 th | 350.00 | 2255.00 | 1200.00 | 1900.00 |
| 5 th | 340.00 | 2360.00 | 1330.00 | 2090.00 |
| Half-space | - | 5595.00 | 3225.00 | 2890.00 |

The model derived from the joint inversion analysis reveals the presence of two relatively thin layers characterized by low V_S , but higher than Apostolidis et al. [6] calculated. These were succeeded by a layer extending to a thickness of ~ 22 m, thinner than [6] derived, with a slightly higher V_S , followed by two substantially thicker layers, where $V_S > 1000$ m/s. The model concludes with the halfspace, where the shear wave velocity signifies the transition to the seismological bedrock (figure 4.1c). The inverted HVSr and DC exhibit sufficient agreement with the observed ones as shown in figure 4.1a and 4.1b, whereas the overall best misfit equals to 9.66.

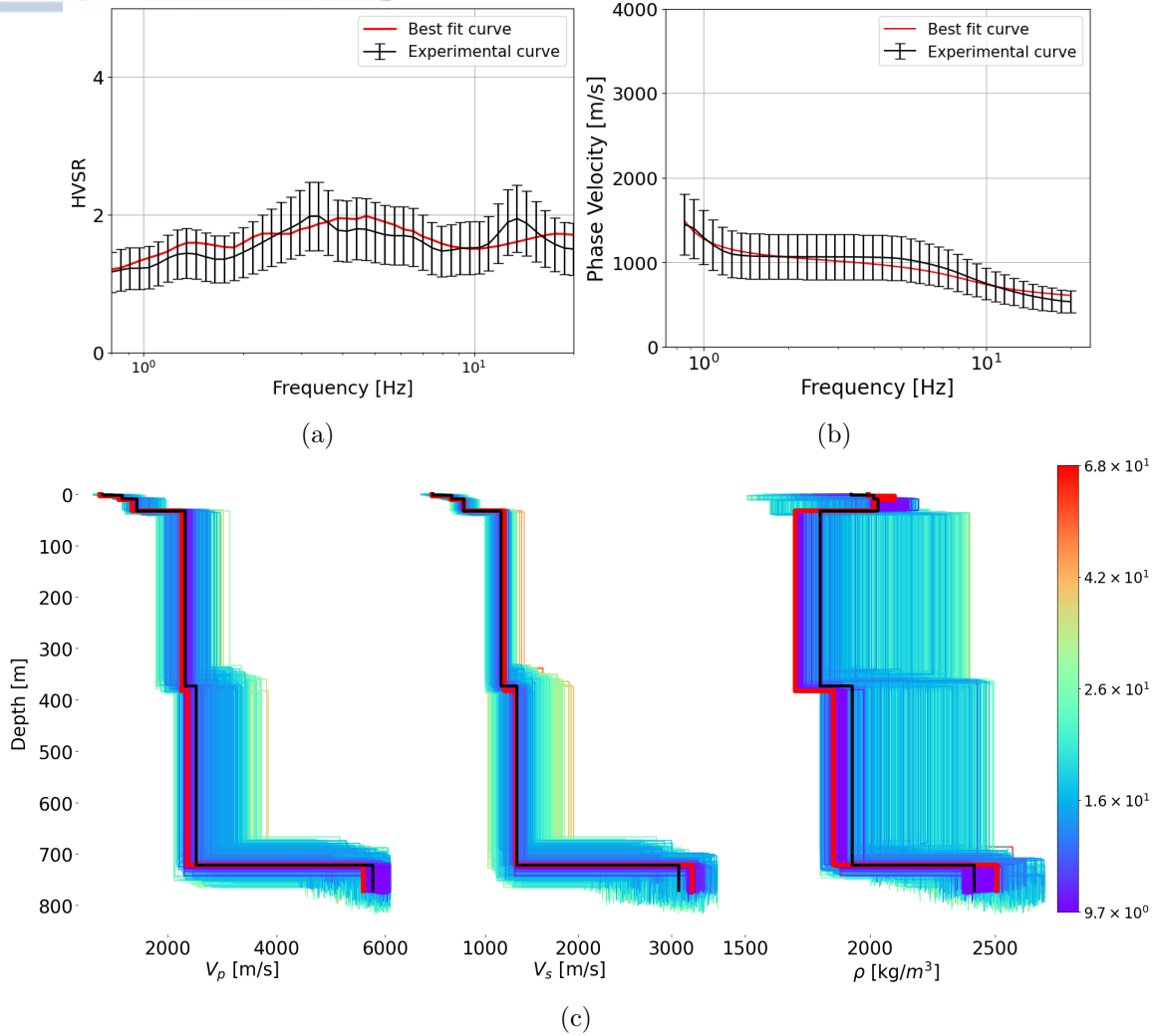


Figure 4.1: Results of joint inversions of empirical mHVSr and dispersion curves for the reference station 'AIG2'. Black line error bars in 4.1a and 4.1b represent the experimental mHVSr and dispersion curve, respectively, with assumed standard deviation 40%, while the red lines represent the corresponding theoretical ones. In 4.1c, the coloured lines show the forward calculations for the velocity models, the black line represents the mean model, while the red line the best fitting model for V_P , V_S (m/s) and density (kg/m^3), from left to right.

Located at the General Hospital of Arta, Greece, the reference station 'ART2' is positioned atop Mesozoic and Paleozoic limestone formations, implying a high degree of stiffness due to the geological age of the formations. The geology itself evinces a hard rock site, leading to set high V_s for the lower formations, as it is verified also by the inversion results (Table 4.3 and Table 4.4). The initial mHVSr and dispersion curves, figure 4.2a and 4.2b, respectively, present a slight peak at lower frequencies and

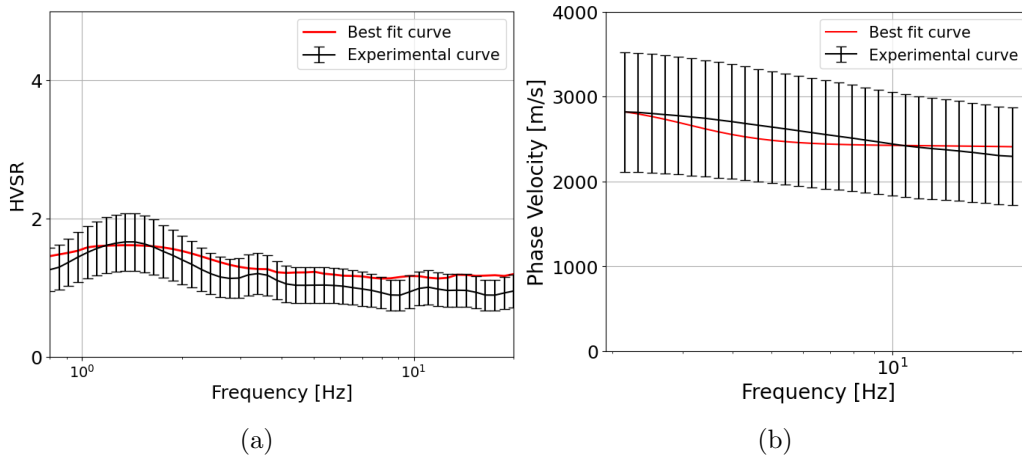
a minimum reduction of phase velocity throughout the frequency range, confirming that reference station 'ART2' is located on hard rock site. The inverted HVSR and DC are depicted in the aforementioned figures, and the V_{PZ} , V_{SZ} and ρ_Z profiles in figure 4.2c, present a best misfit of ~ 18 .

Table 4.3: Initial parameter model for space exploration in the joint inversion procedure for reference station "ART2".

| Layer | Thickness (m) | V_p (m/s) | V_S (m/s) | Density (kg/m ³) |
|-----------------|-----------------|-------------------|-------------------|------------------------------|
| 1 st | 0.00 - 2.00 | 400.00 - 3000.00 | 200.00 - 1000.00 | 1700.00 - 2000.00 |
| 2 nd | 2.00 - 50.00 | 2000.00 - 6000.00 | 1000.00 - 2800.00 | 1900.00 - 2300.00 |
| 3 rd | 200.00 - 500.00 | 2500.00 - 6000.00 | 1500.00 - 3000.00 | 2100.00 - 2500.00 |
| Half-space | - | 5000.00 - 6500.00 | 3000.00 - 3400.00 | 2400.00 - 2900.00 |

Table 4.4: Values of the best fit and final parameter model for reference station "ART2".

| Layer | Thickness (m) | V_p (m/s) | V_S (m/s) | Density (kg/m ³) |
|------------|---------------|-------------|-------------------------------|------------------------------|
| 1 | 1.00 | 1510.00 | 865.00 | 1700.00 |
| 2 | 4.25 | 4365.00 | 2500.00 | 2095.00 |
| 3 | 351.00 | 4595.00 | 2650.00 </td <td>2120.00</td> | 2120.00 |
| Half-space | - | 5675.00 | 3275.00 | 2500.00 |



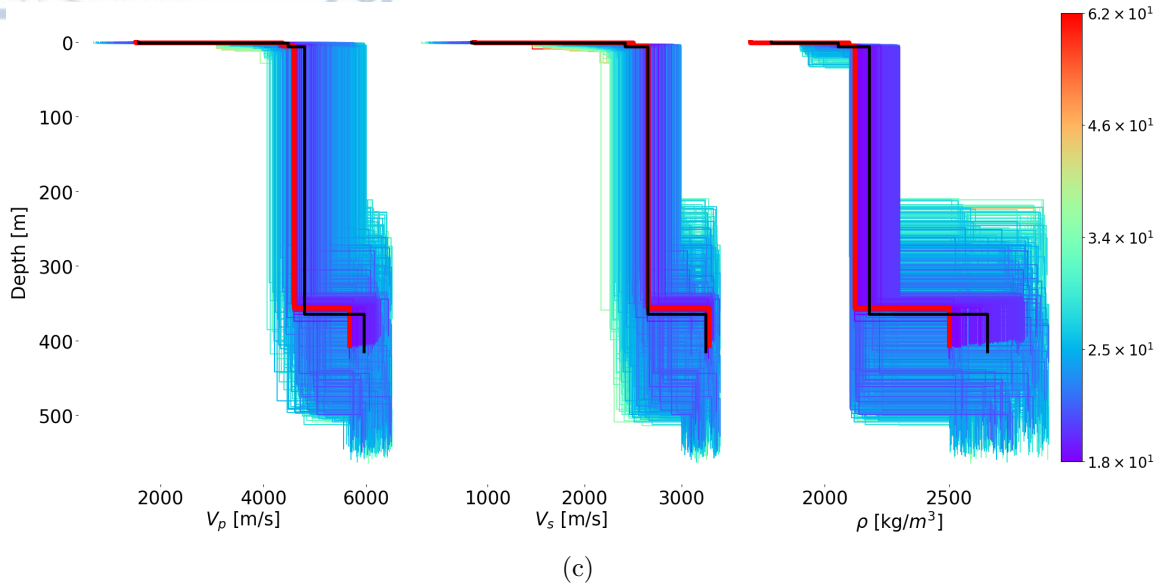


Figure 4.2: Results of joint inversions of empirical mHVSr and dispersion curves for the reference station 'ART2'. Black line error bars in 4.2a and 4.2b represent the experimental mHVSr and dispersion curve, respectively, with assumed standard deviation at 40%, while the red lines represent the corresponding theoretical ones. In 4.2c, the coloured lines show the forward calculations for the velocity models, the black line represents the mean model, while the red line the best fitting model for V_p , V_s (m/s) and density (kg/m^3), from left to right.

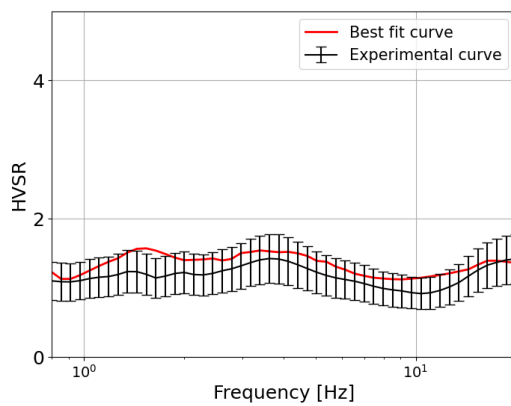
'ATH5' station, is located in Athens, Greece, positioned above formations of Tertiary geologic period. Nonetheless, the broader region exhibits a more complex geological composition, with neighbour formations classified in Holocene, Pleistocene and Mesozoic - Paleocene periods. The initial parameter model in Table 4.5, was constructed by gradually adding more thin layers in the first few meters until reaching the final model where the misfit lowers down to ~ 15 . From the final V_{SZ} profile in Table 4.6, emerges that V_s reaches approximately 0.8 km/s already from the first layers, meeting the engineering bedrock. The inverted HVSr curve in Figure 4.3a displays greater amplification in higher frequencies compared to the observed mHVSr, which is likely the primary cause of the higher misfit between the HVSr curves. The observed and theoretical DCs, as well as the derived profiles are shown in Figure 4.3b and 4.3c, respectively.

Table 4.6: Values of the best fit and final parameter model for reference station 'ATH5'.

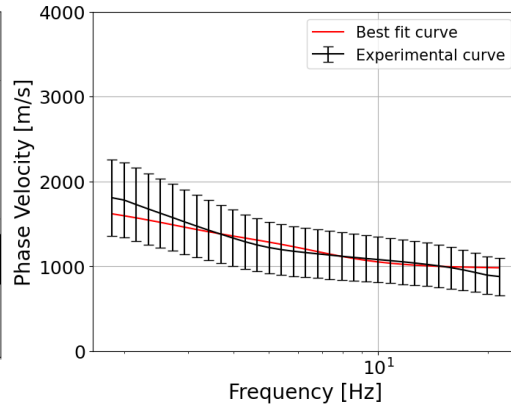
| Layer | Thickness (m) | V_p (m/s) | V_S (m/s) | Density (kg/m ³) |
|-----------------|------------------|----------------|----------------|---------------------------------|
| 1 st | 1.34 | 1260.00 | 725.00 | 2100.00 |
| 2 nd | 0.72 | 1345.00 | 775.00 | 2100.00 |
| 3 rd | 55.70 | 1885.00 | 1090.00 | 2500.00 |
| 4 th | 183.50 | 3430.00 | 1665.00 | 1900.00 |
| 5 th | 720.84 | 4200.00 | 1920.00 | 2000.00 |
| 6 th | 37.33 | 4810.00 | 2310.00 | 2535.00 |
| Half-space | - | 6160.00 | 3470.00 | 2895.00 |

Table 4.5: Initial parameter model for space exploration in the joint inversion procedure for reference station 'ATH5'.

| Layer | Thickness (m) | V_p (m/s) | V_S (m/s) | Density (kg/m ³) |
|-----------------|------------------|-------------------|-------------------|---------------------------------|
| 1 st | 0.50 - 2.00 | 900.00 - 1500.00 | 500.00 - 750.00 | 1700.00 - 2100.00 |
| 2 nd | 0.00 - 2.00 | 1000.00 - 1500.00 | 600.00 - 850.00 | 1700.00 - 2100.00 |
| 3 rd | 45.00 - 70.00 | 1500.00 - 3000.00 | 800.00 - 1500.00 | 1900.00 - 2500.00 |
| 4 th | 100.00 - 250.00 | 1900.00 - 4000.00 | 1200.00 - 2000.00 | 1900.00 - 2400.00 |
| 5 th | 50.00 - 800.00 | 2000.00 - 5000.00 | 1300.00 - 2500.00 | 2000.00 - 2500.00 |
| 6 th | 20.00 - 85.00 | 4500.00 - 6000.00 | 2000.00 - 3000.00 | 2400.00 - 2700.00 |
| Half-space | - | 5000.00 - 6500.00 | 3000.00 - 3700.00 | 2600.00 - 2900.00 |



(a)



(b)

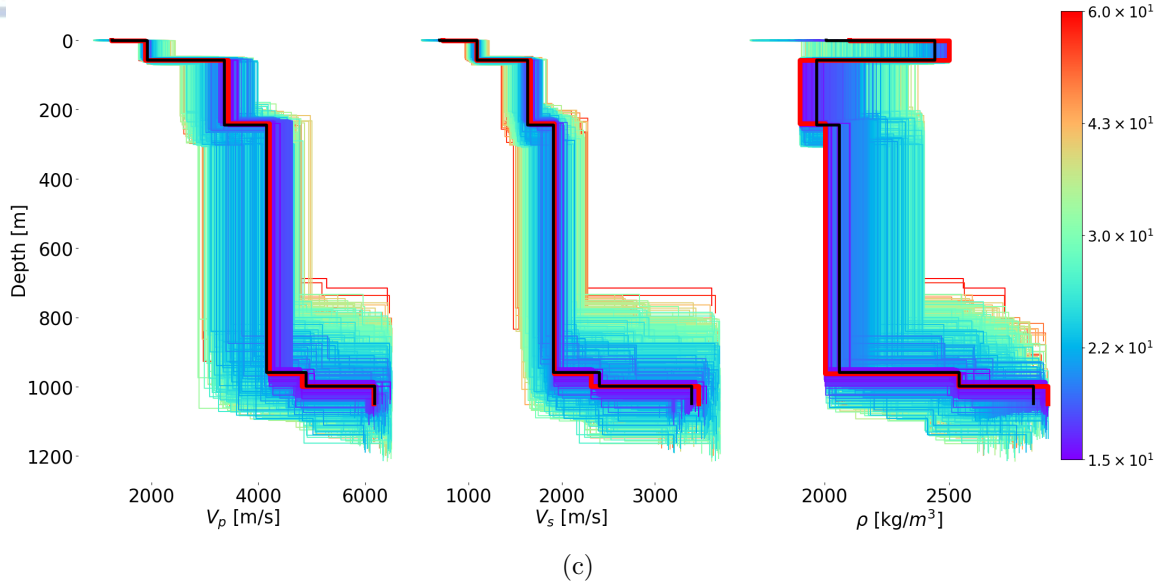


Figure 4.3: Results of joint inversions of empirical mHVSr and dispersion curves for the reference station 'ATH5'. Black line error bars in 4.3a and 4.3b represent the experimental mHVSr and dispersion curve, respectively, with assumed standard deviation at 40%, while the red lines represent the corresponding theoretical ones. In 4.3c, the coloured lines show the forward calculations for the velocity models, the black line represents the mean model, while the red line the best fitting model for V_p , V_s (m/s) and density (kg/m^3), from left to right.

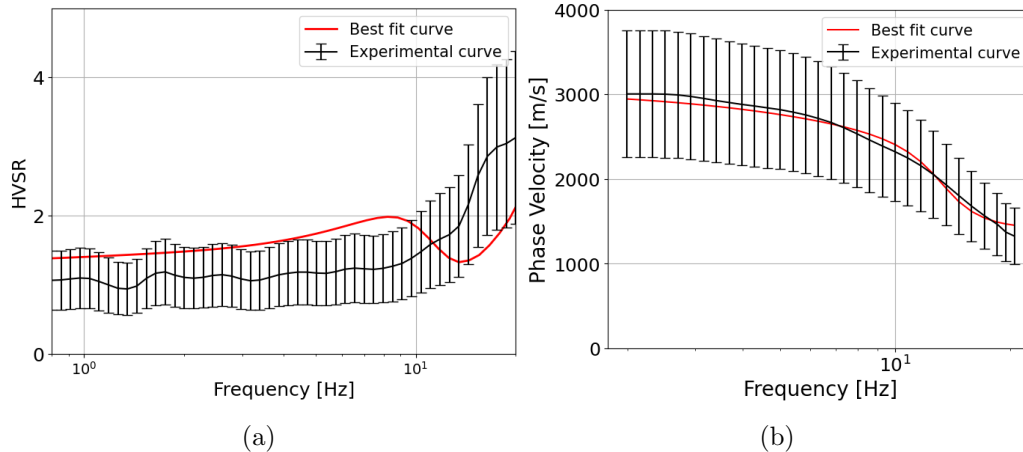
Located at the Seismological Station of Thessaloniki, 'SEIS' station is positioned above formations from the Tertiary and Mesozoic-Paleocene periods. Geological maps provided by IGME (Institute of Geology and Mineral Exploration) depict the geological formation as Mesozoic leucocratic albite-sericite-microcline gneiss. Despite the fact that the regional geology does not suggest complexity, inversion analyses of the HVSr and dispersion curves have demonstrated otherwise. Multiple initial models were utilized to satisfactorily accomplish the simultaneous inversion of data, even though, in the end, the misfit value appears higher than what was desired. Throughout the parametric investigation, the best fitting parametric model is presented in Table 4.7 and the final model in Table 4.8. While, inverted and observed DCs depict an almost perfect agreement (figure 4.4b), theoretical HVSr curve differs from the observed for frequencies ~ 5 Hz to 15 Hz, as illustrated in figure 4.4a. 'SEIS' exhibited the highest misfit among all six reference stations, equal to ~ 36 , which can be attributed to the difference of observed and inverted HVSr. The V_p and V_s profiles in figure 4.4c, present a gradual increase of velocity with depth, while the density model (figure 4.4c right) fluctuates in the top soil layers.

Table 4.7: Initial parameter model for space exploration in the joint inversion procedure for reference station 'SEIS'.

| Layer | Thickness (m) | V_p (m/s) | V_S (m/s) | Density (kg/m ³) |
|-----------------|---------------|-------------------|-------------------|------------------------------|
| 1 st | 1.00 - 4.00 | 800.00 - 1600.00 | 500.00 - 900.00 | 1500.00 - 1800.00 |
| 2 nd | 2.00 - 8.00 | 1000.00 - 1800.00 | 600.00 - 1000.00 | 1800.00 - 2200.00 |
| 3 rd | 8.00 - 18.00 | 1500.00 - 4500.00 | 1000.00 - 2800.00 | 2000.00 - 2500.00 |
| 4 th | 8.00 - 18.00 | 1500.00 - 4500.00 | 1000.00 - 2800.00 | 2000.00 - 2500.00 |
| 5 th | 15.00 - 20.00 | 4000.00 - 5600.00 | 2500.00 - 3100.00 | 2100.00 - 270.00 |
| Half-space | - | 5500.00 - 6100.00 | 2500.00 - 3500.00 | 2000.00 - 2900.00 |

Table 4.8: Values of the best fit and final parameter model for reference station 'SEIS'.

| Layer | Thickness (m) | V_p (m/s) | V_S (m/s) | Density (kg/m ³) |
|-----------------|---------------|-------------|-------------|------------------------------|
| 1 st | 2.21 | 1335.00 | 760.00 | 1575.00 |
| 2 nd | 6.37 | 1500.00 | 865.00 | 2075.00 |
| 3 rd | 14.03 | 4320.00 | 2490.00 | 2485.00 |
| 4 th | 15.13 | 2095.00 | 1205.00 | 2320.00 |
| 5 th | 63.41 | 5320.00 | 3060.00 | 2600.00 |
| Half-space | - | 5790.00 | 3330.00 | 2100.00 |



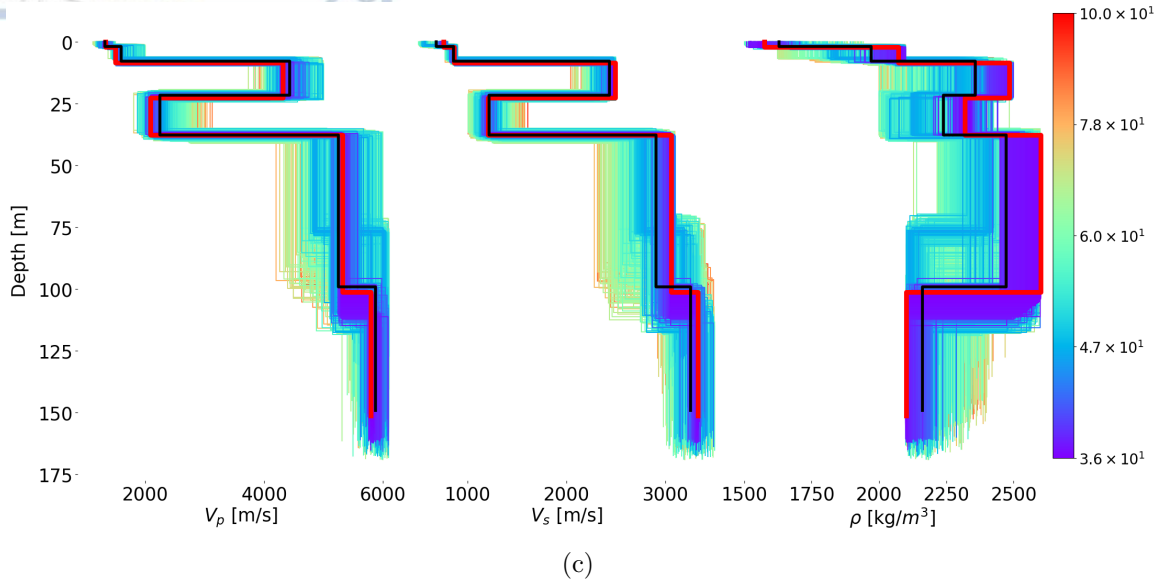


Figure 4.4: Results of joint inversions of empirical mHVSr and dispersion curves for the reference station 'SEIS'. Black line error bars in 4.4a and 4.4b represent the experimental mHVSr and dispersion curve, respectively, with assumed standard deviation at 40%, while the red lines represent the corresponding theoretical ones. In 4.4c, the coloured lines show the forward calculations for the velocity models, the black line represents the mean model, while the red line the best fitting model for V_P , V_S (m/s) and density (kg/m^3), from left to right.

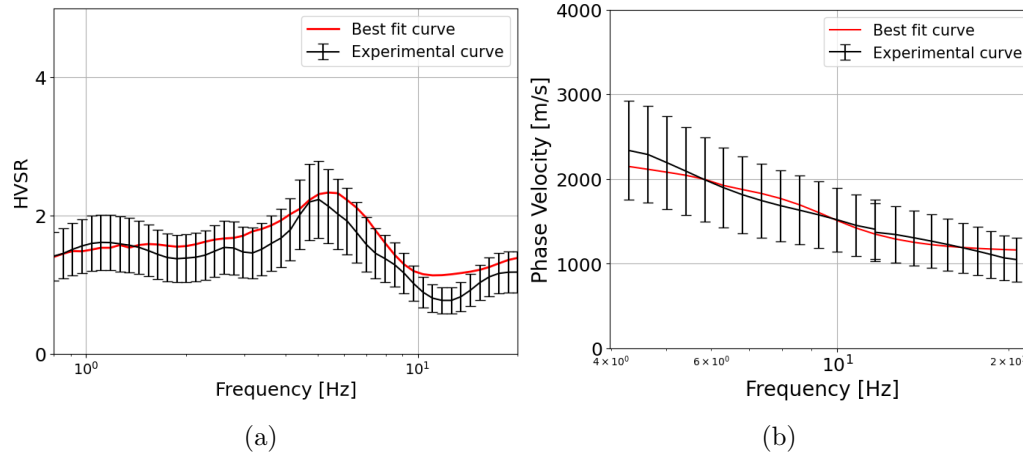
In the region of Siatista, in Western Macedonia, the station 'SIA1' is sited above limestone formation of Tertiary and Mesozoic - Paleocene age. According to IGME geological map, the Siatista area features Middle Triassic limestones, with dolomites and dolomitic limestones interacting within the geological formations. The initial parametric model in Table 4.9 provided the final profile of the station given in Table 4.10. The engineering bedrock is discernible within the first few meters, verifying station definition as reference site, whereas the seismological bedrock is detected at greater depth, more than 1.3km below the surface. Figure 4.5 shows the observed and theoretical mHVSr (4.5a) and DC (4.5b), respectively, and in 4.5c the V_{PZ} , V_{SZ} and ρ_Z profiles, from the left to right. Misfit (m) was estimated for reference station 'SIA1' equal to ~ 12 .

Table 4.9: Initial parameter model for space exploration in the joint inversion procedure for reference station 'SIA'.

| Layer | Thickness (m) | V_p (m/s) | V_S (m/s) | Density (kg/m ³) |
|-----------------|------------------|-------------------|-------------------|------------------------------|
| 1 st | 0.30 - 2.00 | 900.00 - 2000.00 | 500.00 - 900.00 | 1600.00 - 1900.00 |
| 2 nd | 45.00 - 70.00 | 1200.00 - 3000.00 | 1000.00 - 1800.00 | 1900.00 - 2100.00 |
| 3 rd | 200.00 - 400.00 | 2300.00 - 5500.00 | 1800.00 - 2500.00 | 2000.00 - 2400.00 |
| 4 th | 500.00 - 1000.00 | 4000.00 - 6000.00 | 2000.00 - 3000.00 | 2300.00 - 2700.00 |
| Half-space | - | 5000.00 - 6500.00 | 3000.00 - 3800.00 | 2500.00 - 2900.00 |

Table 4.10: Values of the best fit and final parameter model for reference station 'SIA'.

| Layer | Thickness (m) | V_p (m/s) | V_S (m/s) | Density (kg/m ³) |
|-----------------|---------------|-------------|-------------|------------------------------|
| 1 st | 0.50 | 1445.00 | 835.00 | 1715.00 |
| 2 nd | 50.08 | 2170.00 | 1250.00 | 2100.00 |
| 3 rd | 312.60 | 4760.00 | 2430.00 | 2100.00 |
| 4 th | 964.20 | 4810.00 | 2530.00 | 2455.00 |
| Half-space | - | 6215.00 | 3590.00 | 2520.00 |



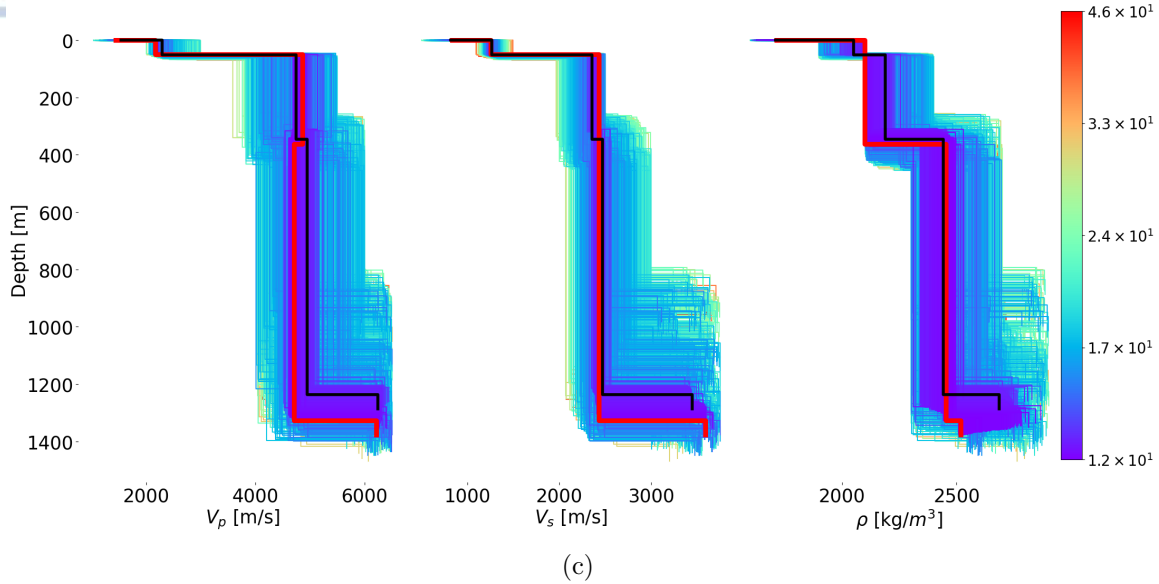


Figure 4.5: Results of joint inversions of empirical mHVSr and dispersion curves for the reference station 'SIA'. Black line error bars in 4.5a and 4.5b represent the experimental mHVSr and dispersion curve, respectively, with assumed standard deviation at 40%, while the red lines represent the corresponding theoretical ones. In 4.5c, the coloured lines show the forward calculations for the velocity models, the black line represents the mean model, while the red line the best fitting model for V_P , V_S (m/s) and density (kg/m^3), from left to right.

The reference station, VSK1, is situated in Vassilikiades, the northern part of Kefalonia island, a highly seismic active region, on its top characterized by thin-bedded limestones of Mesozoic - Paleocene formations. The observed mHVSr curve in figure 4.6a (black line) indicates the site's hardness, as it appears almost completely flat, demonstrating minimal variability across the frequency range. After testing many parametric models, the one that provided the best final profile with the smallest misfit is listed in Table 4.11, while the final model is presented in Table 4.12 and depicted in figure 4.6c. The observed mHVSr and DC are shown in black in figures 4.6a and 4.6b, respectively, while the theoretical mHVSr and DC are represented in red and the best misfit has evaluated approximately 9.5.

The joint inversion of mHVSrs and DCs is anticipated to provide more reliable results compared to the inversion that uses only one method. However, relatively high misfits were observed at each reference station, with the highest being observed at 'SEIS'. Consequently, V_{SZ} profiles for these six reference stations obtained from different sources were employed in subsequent analyses, aiming to assess the reliability of the results and their contribution to the overall findings. Theodoulidis et al. (2004, personal communication) calculated the V_{SZ} profiles for the same stations using the Geopsy software [2] and its Dinver tool, which were developed under the framework

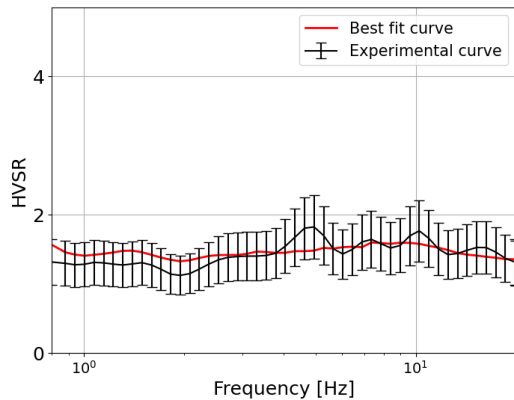
of european project SESAME [76].

Table 4.11: Initial parameter model for space exploration in the joint inversion procedure for reference station "VSK1".

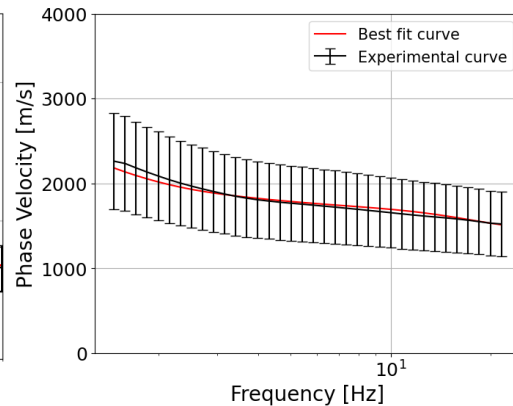
| Layer | Thickness (m) | V_p (m/s) | V_S (m/s) | Density (kg/m ³) |
|-----------------|------------------|-------------------|-------------------|---------------------------------|
| 1 st | 1.00 - 5.00 | 800.00 - 3000.00 | 300.00 - 1000.00 | 1700.00 - 2300.00 |
| 2 nd | 10.00 - 50.00 | 1000.00 - 5000.00 | 1000.00 - 2000.00 | 1700.00 - 2400.00 |
| 3 rd | 50.00 - 100.00 | 1000.00 - 6000.00 | 1100.00 - 2500.00 | 1700.00 - 2500.00 |
| 4 th | 240.00 - 500.00 | 2000.00 - 6000.00 | 1500.00 - 2800.00 | 1700.00 - 2500.00 |
| 5 th | 600.00 - 900.00 | 3000.00 - 6000.00 | 1800.00 - 3000.00 | 1900.00 - 2600.00 |
| Half-space | - | 3000.00 - 6200.00 | 2000.00 - 3600.00 | 2500.00 - 2900.00 |

Table 4.12: Values of the best fit and final parameter model for reference station "VSK1".

| Layer | Thickness (m) | V_p (m/s) | V_S (m/s) | Density (kg/m ³) |
|-----------------|------------------|----------------|----------------|---------------------------------|
| 1 st | 2.23 | 1760.00 | 860.00 | 2300.00 |
| 2 nd | 34.27 | 2800.00 | 1615.00 | 2400.00 |
| 3 rd | 82.31 | 4050.00 | 1950.00 | 2495.00 |
| 4 th | 400.00 | 4790.00 | 2220.00 | 1700.00 |
| 5 th | 765.78 | 5165.00 | 2585.00 | 1900.00 |
| Half-space | - | 6165.00 | 3550.00 | 2895.00 |



(a)



(b)

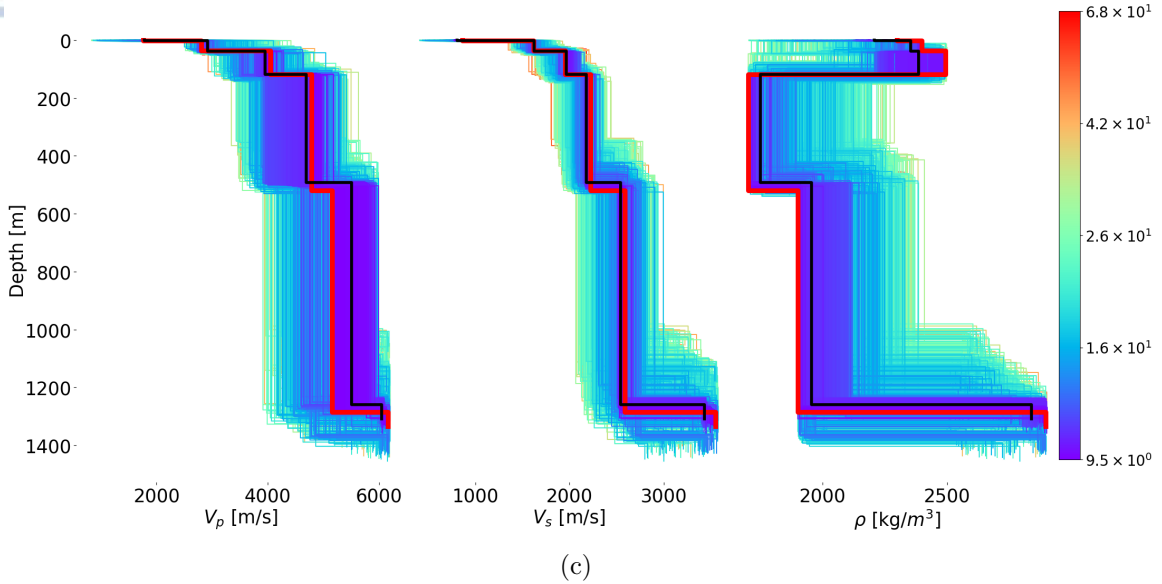
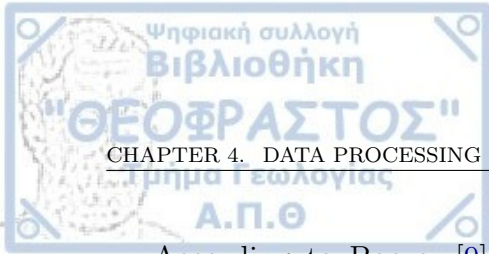


Figure 4.6: Results of joint inversions of empirical mHVSr and dispersion curves for the reference station "VSK1". Black line error bars in 4.6a and 4.6b represent the experimental mHVSr and dispersion curve, respectively, with assumed standard deviation at 40%, while the red lines represent the corresponding theoretical ones. In 4.6c, the colored lines show the forward calculations for the velocity models, the black line represents the mean model, while the red line the best fitting model for V_P , V_S (m/s) and density (kg/m^3), from left to right.

4.2 1D - Theoretical Site Spectral Amplification Factors ($SAF_S^{theoretical}$) of 6 Reference Stations

As mentioned in 2.2, for the vertically incident waves the $SAF^{theoretical}$ in the horizontal and vertical component were estimated, to adapt the surface (observed) Fourier spectra to the engineering and seismological bedrock. Therefore, to formulate the $SAF_S^{theoretical}$, the computer software $PS_V S_H-1D$ was used, which produces $SAF^{theoretical}$ for both horizontal and vertical components, by setting the values of basic parameters such as density, thickness of the layers, V_S and V_P , and quality factors Q_S and Q_P that have been stem from the models obtained through the inversion process. From the 'HV-inv' software, the final V_{SZ} profiles provides V_{PZ} , V_{SZ} and ρ_Z profiles. However, the profiles extracted from the study conducted by Theodoulidis et al. 2004 (personal communication), provides, exclusively, the thicknesses of formations and the corresponding V_S values. Thus, in order to determine the necessary parameters that the $PS_V S_H-1D$ software requires, a set of equations was employed that established the correlation between V_S , ρ , and V_P .



According to Boore, [9], the equations that describes the connection between density(ρ) and V_s are:

For $V_s < 0.30$ km/s:

$$\rho(g/cm^3) = 1 + \frac{1.53 \cdot V_s^{0.85}}{0.35 + 1.889 \cdot V_s^{1.7}} \quad (4.3)$$

For 0.30 km/s $< V_s < 3.55$ km/s:

$$\rho(g/cm^3) = 1.74V_p^{0.25} \quad (4.4)$$

where:

$$V_p(km/sec) = 0.9409 + 2.094 \cdot V_s - 0.8206 \cdot V_s^2 + 0.2683 \cdot V_s^3 - 0.0251 \cdot V_s^4 \quad (4.5)$$

Therefore, if V_s is known, then it is possible to calculate both density and V_p values, albeit with the deviation from the actual value, in order to construct the input parameter files into $PS_V S_H-1D$ software.

Incorporating the findings from Graves and Pitarka, [26], for the 1994 Northridge earthquake in Southern California, as cited in Bocher, [15], the relationship between quality factor, Q_s , and shear wave velocity yields:

For $V_s < 0.30$ km/s:

$$Q_s = 13 \quad (4.6)$$

For 0.30 km/s $< V_s < 5$ km/s:

$$Q_s = -16 + 10413 \cdot V_s - 25.225 \cdot V_s^2 + 8.2184 \cdot V_s^3 \quad (4.7)$$

and

$$Q_p = 2 \cdot Q_s \quad (4.8)$$

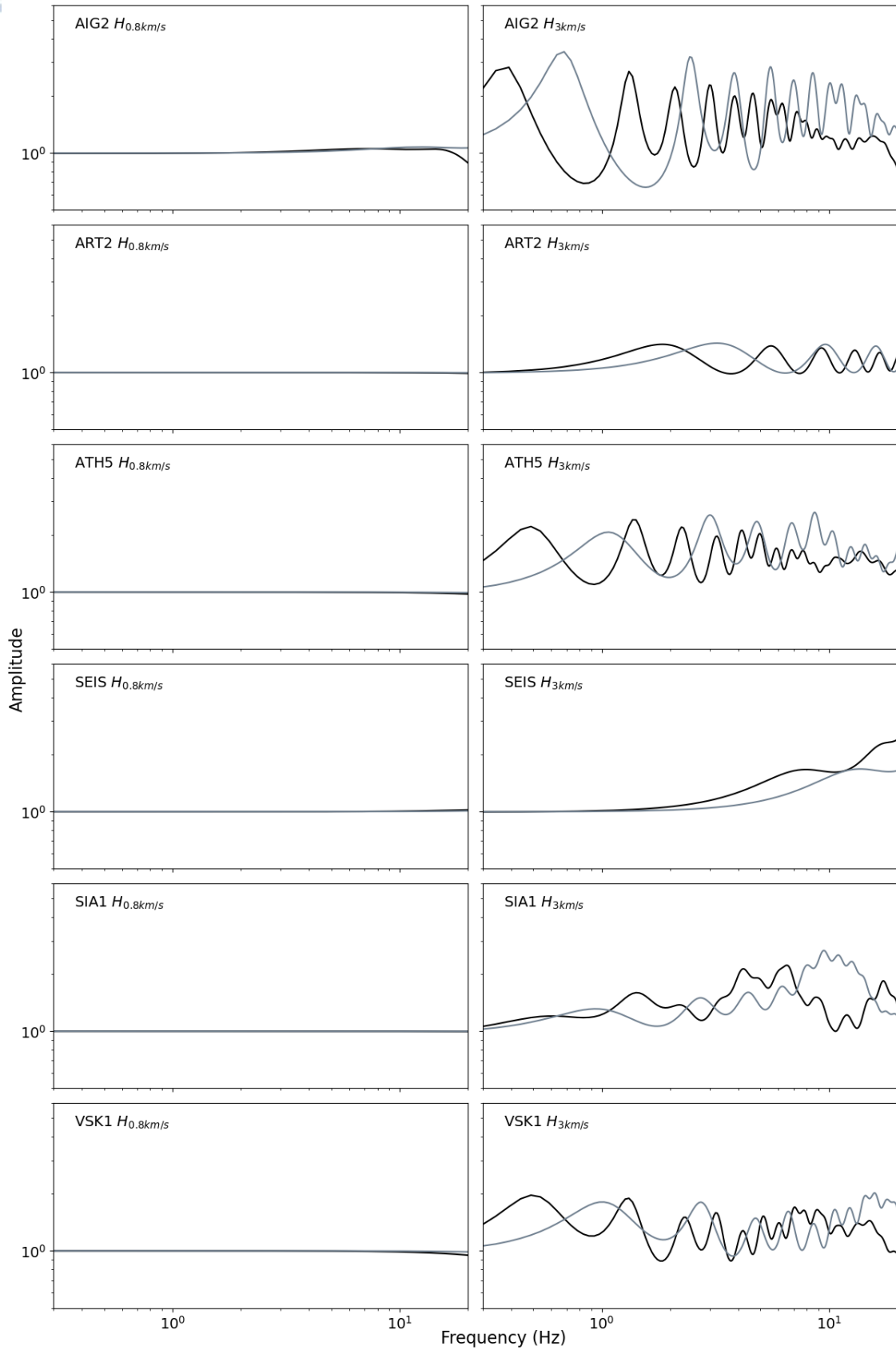
The $SAF^{theoretical}$ have been generated based on the profiles coming from 'HV-inv' ($SAF_{HV-Inv}^{theoretical}$) and Geopsy-Dinver ($SAF_{G-D}^{theoretical}$) down to depth (H) where shear

wave velocity V_s attained 0.8 km/s and signify the engineering bedrock. In the present study it is symbolised as $H_{0.8\text{km/s}}$, and at depth —typically the halfspace— where V_S reached 3 km/s is symbolized as $H_{3\text{km/s}}$. Henceforth, when referring to $H_{0.8\text{km/s}}$ and $H_{3\text{km/s}}$, it is in the context of these methodologies. The resulted $SAF^{theoretical}$ from the output of 'HV-inv', are shown in Figure 4.7, organized in alphabetical order by station, the $SAF^{theoretical}$ of $H_{0.8\text{km/s}}$ on the left side, while on the right side of $H_{3\text{km/s}}$. $SAF^{theoretical}$ were submitted to Konno-Ohmachi smoothing algorithm (Konno & Ohmachi, [45]), which is designed to achieve a "uniform-span" smoothing of spectra on a logarithmic scale. The smoothing coefficient of the Konno & Ohmachi equation was set to 60% (lower coefficient results in greater smoothing).

The goal of comparing the $SAFs_{HV-Inv}^{theoretical}$ against $SAFs_{G-D}^{theoretical}$ is visualise how amplification varies with depth at each reference station, as well as identifying stations' amplification level between horizontal and vertical components. Distinct variations were evident in the $SAF^{theoretical}$ of $H_{0.8\text{km/s}}$ versus $H_{3\text{km/s}}$ at each station. For the engineering bedrock, amplification is virtually absent, as indicated by curves that remain around 1 with slight fluctuations at higher frequencies, mainly above 10 Hz. On the contrary, for seismological bedrock there's an observable fluctuation in amplification as frequencies escalate.

The produced V_{SZ} profiles from Geopsy-Dinver were normalised to create the respective $SAF^{theoretical}$ and plot them against the corresponding $SAF^{theoretical}$ unsmoothed created by V_{SZ} profiles from 'HV-inv' software. This comparison (figure 4.8) aims to distinguish the amplification differences between the two approaches. For $H_{0.8\text{km/s}}$, the horizontal component of $SAFs_{G-D}^{theoretical}$, exhibits minor discrepancies when compared to the same component derived from an alternate method, showing increased deamplification at higher frequencies at stations AIG2, ATH5, SIA1 and VSK1, and a higher amplification at SEIS. On the other hand, when the $SAF^{theoretical}$ refer to the seismological bedrock, $H_{3\text{km/s}}$, for horizontal and vertical components, there is an evident change in amplification with the increase of frequency.

Given that the $SAF^{theoretical}$ have been calculated to indicate the amplification at various frequencies at a specific depth, it is now feasible to deconvolve the Fourier Amplification Spectra (FAS) on the surface and adapt them to engineering and seismological bedrock, where the shear wave velocity reaches 0.8 km/s and 3 km/s, respectively. This adaption is succeeded at the six reference stations, by dividing the vertical and horizontal FAS recorded on surface, with the respective computed $SAFs^{theoretical}$. The corrected FAS are, then, used as input to Generalized Inversion method to calculate three crucial factors: the effects of seismic source, the propagation path and the local site conditions.



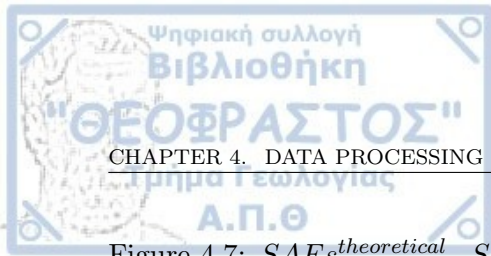
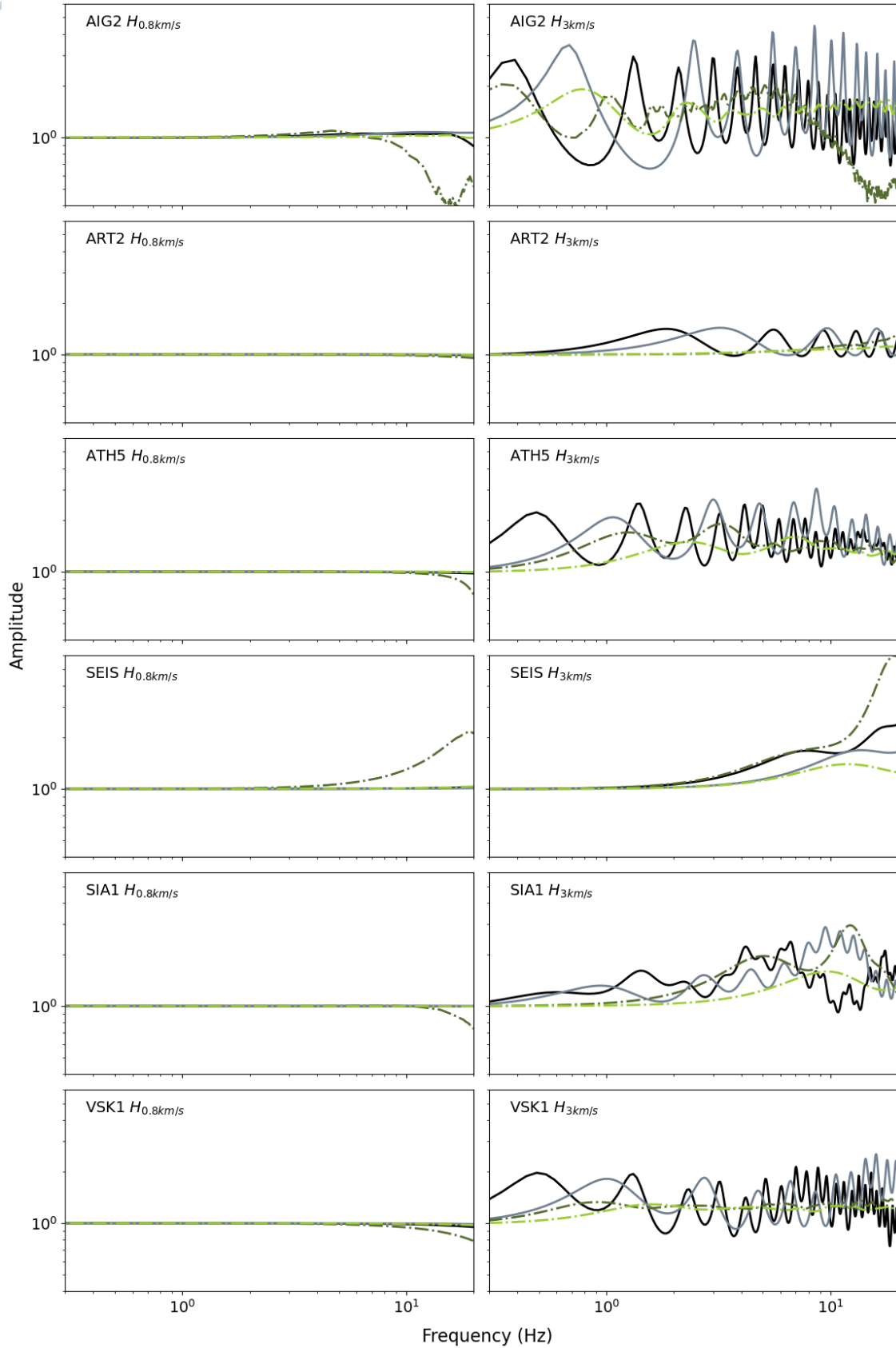


Figure 4.7: $SAF_{HV-Inv}^{theoretical} \cdot SAF^{theoretical}$ for depths where the V_s reaches 0.8 km/s (left), and 3 km/s (right). Horizontal component is represented by the black line, while the vertical component by the grey line.



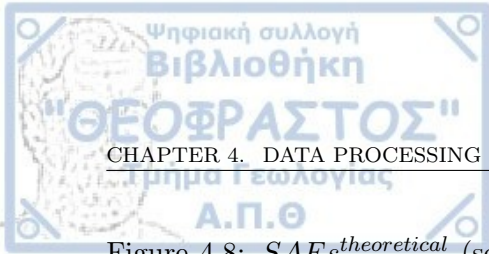


Figure 4.8: $SAFs_{HV-Inv}^{theoretical}$ (solid lines) and $SAFs_{G-D}^{theoretical}$ (dashed lines). $SAFs^{theoretical}$ for depths, where the V_s reaches 0.8 km/s (left), and 3 km/s (right). Black line represent horizontal $SAFs_{HV-Inv}^{theoretical}$ and dark blue horizontal $SAFs_{G-D}^{theoretical}$. Grey line represent vertical $SAFs_{HV-Inv}^{theoretical}$ and light blue line vertical $SAFs_{G-D}^{theoretical}$

4.3 Generalized Inversion Technique (GIT)

As mentioned in Chapter 2.3, GIT is a cornerstone in seismic research, which allows a deeper comprehension of three crucial factors that affect the seismic motion: the seismic source, the propagation path and the site properties. These factors were pivotal in better understanding the complexities of seismic ground motion. GIT is categorized into two main approaches: nonparametric and parametric. The parametric GIT, which is the focus of this study, can operate independently of reference site conditions by leveraging theoretical functions for the factors of seismic source and attenuation path. Using S wave Fourier spectra, the GIT algorithm applied in this study, developed by Grendas et al. [29], is based on a Gauss-Newton iterative inversion method, as described by Tarantola, [82], inverting for source, path, and site factors simultaneously, allowing synchronous inversion of M_0 and f_c versus stress drop. The objective of the algorithm is to converge towards a solution that minimizes the deviation between the observed data and computed ones by the inverted models and the differences between the initial and final model parameters, considering their a priori covariances.

An evaluation is conducted in order to determine which of the two software packages, 'HV-inv' or the Geopsy-Dinver, is most suitable to obtain the V_{SZ} profiles for the final calculation of the three parameters mentioned. The Generalized Inversion (GI) is performed four times using a simple attenuation model tailored to the study area and the results of these inversions were compared to identify the most reliable approach. Following the validation of the selected software, a final GI was performed to accurately determine the source, path and site factors, extending to the engineering and seismological bedrock.

4.3.1 Selection of V_{SZ} profiles of reference stations for GIT implementation

To settle on the approach, either the 'HV-Inv' or the Geopsy-Dinver software, which will ultimately be used to calculate the three factors through GIT. The generalized inversion was conducted four times, on the deconvolved FASs from both software packages, with respect to the seismological and engineering bedrock, employing

an homogeneous attenuation model. This model simplifies the area of interest into a single cell and the anelastic attenuation factor was calculated only once. Within the cell the epicentral distance extends over to 1000 km, and uniformly assesses the geometrical spreading coefficient, γ . In this setup, the iterations were restricted to fifteen, while the horizontal components of corrected FASs for horizontal components of the reference stations were defined as site references. Although the initial parameters set were quite simple, this model can be considered satisfying to select the final best software for present study purposes.

From seismic source factor, the moment magnitude, M_w and the corner frequency, f_c have calculated. The moment magnitude derived from GIT, $M_{w(inv)}$ versus the observed moment magnitude, $M_{w(init)}$ are presented in 4.9 (top) and corner frequency, f_c versus the $M_{w(inv)}$ are shown in 4.9 (bottom). The comparison of these calculated factors is conducted between 'HV-Inv' and Geopsy-Dinver for $H_{0.8\text{ km/s}}$ and $H_{3\text{ km/s}}$, using the same bedrock as a reference. The analysis indicates that there are no noticeable differences between the two software, that would direct the investigation towards one of them.

Table 4.13 shows the results of three factors related to attenuation, the geometrical spreading coefficient, γ , the quality factor, Q at a reference frequency of 1 Hz, that corresponds to Q_0 , and a parameter, α , that describes the frequency dependence of quality factor Q , along with their standard deviation. Additionally, the overall misfit of the inversion process is included. It is apparent that the differences between the two software were negligible, suggesting that the notable discrepancies observed in the V_{SZ} profiles and the $SAF^{theoretical}$ produced by 'HV-Inv' and Geopsy-Dinver, do not significantly impact the ultimate outcomes of the generalized inversion. Equally noteworthy were the minor differences observed between the results regarding $H_{0.8\text{ km/s}}$ and $H_{3\text{ km/s}}$. The overall output misfit is, basically, stable for each scenario and is sufficiently low to be considered acceptable. Ultimately, the results of the attenuation path parameters do not dictate a preference for one software over the other.

The site amplification factors (SAFs) were also calculated in this study. The Horizontal SAFs for 6 random scattered station across Greece, are depicted down to engineering bedrock in figure 4.10a, and down to seismological bedrock in figure 4.10b. In figure 4.10a, there is an almost total coincidence of the two curves in every station, while in figure 4.10b insignificant differences are detected, especially in lower frequencies. The aftermath of the above investigation is that both techniques yield similar results, that are reflection of reality, leading to the decision to utilise 'HV-Inv'.

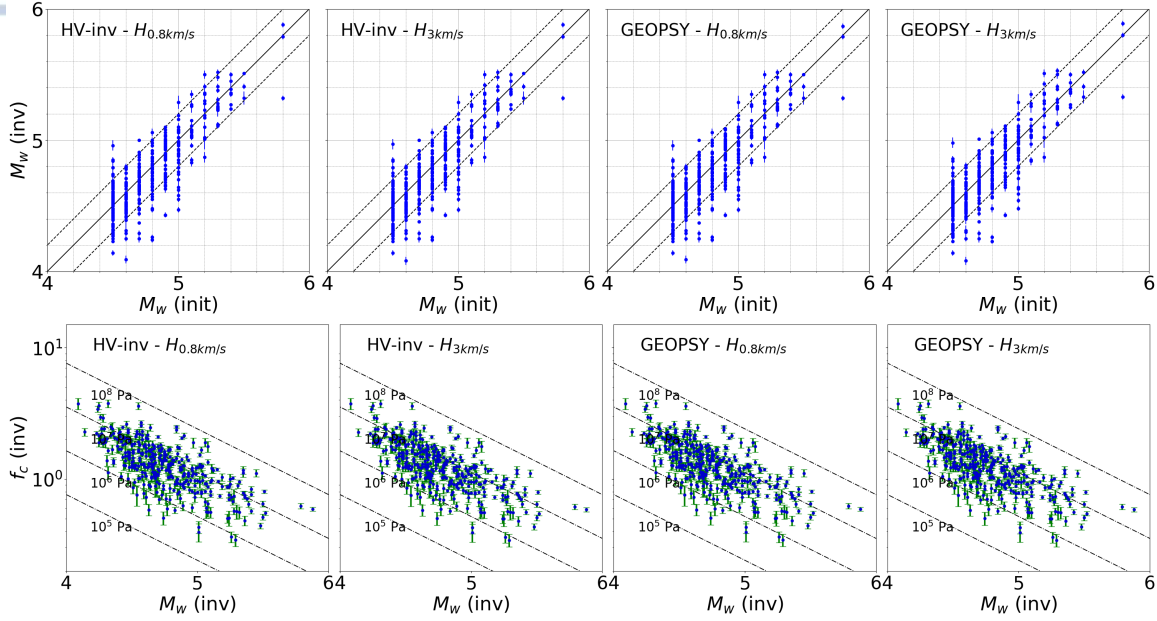


Figure 4.9: Inverted Moment Magnitude (M_w (inv)) versus inverted observed Moment magnitude (M_w (init)) (top). With dashed lines, the range of ± 0.2 of the bisector is depicted. Comparison between the inversion calculated corner frequencies, f_c and the computed M_w , alongside with the Brune's stress drop lines (bottom).

Table 4.13: Propagation path parameters results as derived by the simple attenuation model created to investigate the results from the two software under examination, 'HV-Inv' and Geopsy-Dinver.

| aa | Geopsy-Dinver ($H_{0.8km/s}$) | HV-inv ($H_{0.8km/s}$) | Geopsy-Dinver ($H_{3km/s}$) | HV-inv ($H_{3km/s}$) |
|------------|---------------------------------|--------------------------|-------------------------------|-------------------------|
| γ | 1.0851 ± 0.0008563 | 1.0855 ± 0.0008577 | 1.1034 ± 0.00087148 | 1.1099 ± 0.00086118 |
| Q_0 | 120.8795 ± 0.48065 | 121.1032 ± 0.48235 | 123.6744 ± 0.50229 | 124.2091 ± 0.50686 |
| alpha | 0.62171 ± 0.0024075 | 0.62057 ± 0.0024096 | 0.6112 ± 0.0024404 | 0.61299 ± 0.0024556 |
| min misfit | 0.27597 | 0.27592 | 0.27582 | 0.27566 |

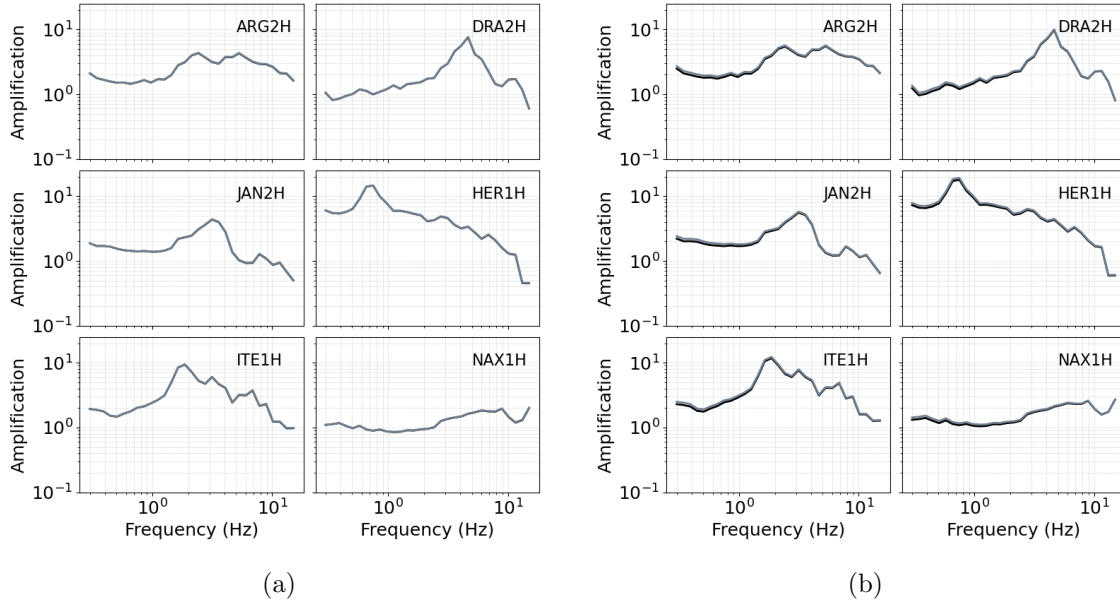


Figure 4.10: Comparison of Horizontal Site Amplification Factors (HSAF) for 6 random stations all over Greece, between 'HV-Inv' (grey line) and Geopsy-Dinver (black line), with respect to engineering bedrock (4.10a) and seismological bedrock (4.10b)

4.3.2 Final GIT for Source, Path, and Site Factors Determination

The adjusted FAS derived from $SAF^{theoretical}$ estimated through 'HV-Inv', with respect to engineering bedrock and seismological bedrock constitute the final datasets for the GIT analysis. To reduce the misfit between actual data and the outcomes of the inverted model, as well as improving the accuracy of the investigated parameters, a more refined attenuation model was developed. To this purpose, the study area was divided into $n = 285$ cells, and the seismic ray paths were segmented into smaller sub-ray paths corresponding to distinct cells, so that the anelastic attenuation factor ($Q(f)$) would be assessed for every cell separately. Regarding the geometrical spreading factor, γ , another attenuation dependent parameter, was investigated for epicentral distances set between 10 - 300 km, with intervals of 10 km. In this setup, the iterations count to ninety, whereas the standard deviation of quality factor Q remained at ± 0.5 and the horizontal components of $SAF^{theoretical}$ were defined as site references, which means that SAFs(f) were forced set to be unity.

4.3.2.1 Seismic Source Factors

As mentioned in 3.2, 372 shallow earthquakes were analysed and located within the designated area, with the observed moment magnitudes ranging from 4.5 to 5.8 ($M_w(\text{init})$) (figure 3.2b). The inverted moment magnitudes derived from the GIT ($M_w(\text{inv})$) versus the $M_w(\text{init})$, are plotted in figure 4.11, when the adjustment of FAS occurred down to the engineering bedrock ($H_{0.8\text{ km/s}}$, left) and to seismological bedrock ($H_{3\text{ km/s}}$, middle).

The logarithmic value of seismic moment, M_o , is calculated from the moment magnitudes, M_w according to Hanks and Kanamori, [31]:

$$\log_{10}(M_o) = 1.5M_w + 9.1 \quad (4.9)$$

The inverted moment magnitudes, generally fall within the ± 1 std, with some exceptions in both engineering and seismological bedrock cases. Nonetheless, it is evident that inverting the two data sets does not significantly impact the seismic source factors. The homogeneity of the two bedrock cases is evident in figure 4.11 (right), where the output $M_w(\text{inv}) - H_{3\text{ km/s}}$ is plotted against $M_w(\text{inv}) - H_{0.8\text{ km/s}}$, following almost perfectly the bisector, while the inconsiderable disparities are depicted in the inset plot of $M_w(\text{inv})$ ratio versus the number of data (= 372).

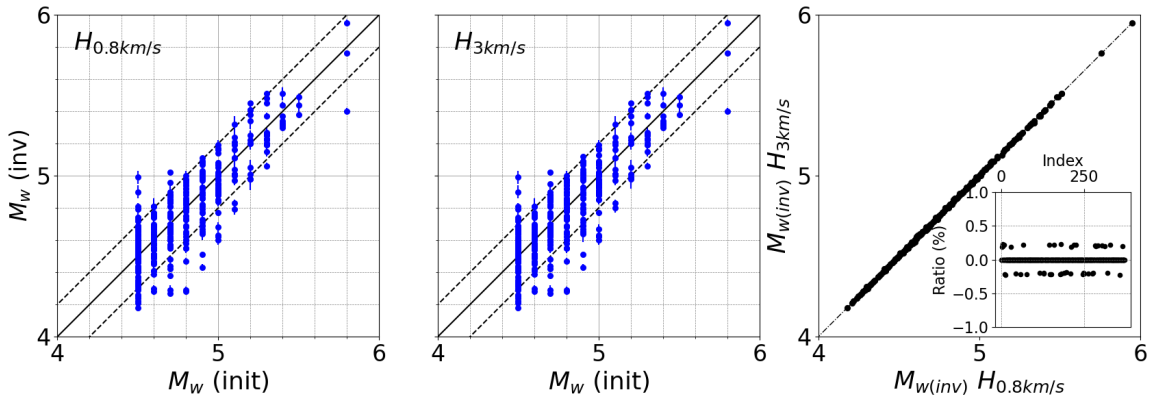


Figure 4.11: Comparison between Inverted Moment Magnitude ($M_w(\text{inv})$) and observed Moment Magnitude ($M_w(\text{init})$). For engineering bedrock $H_{0.8\text{ km/s}}$ (left) and seismological bedrock $H_{3\text{ km/s}}$ (middle). With dashed lines, the range of ± 0.2 of the bisector is depicted. On the right plot direct comparisons between the two bedrock delineations are presented, featuring the $M_w(\text{inv})$ for $H_{0.8\text{ km/s}}$ and $H_{3\text{ km/s}}$, with a bisector as a reference line, and the corresponding ratio (%) according to $\left(\frac{M_w H_{3\text{ km/s}}}{M_w H_{0.8\text{ km/s}}} - 1 \right) \cdot 100\%$ versus the number of data

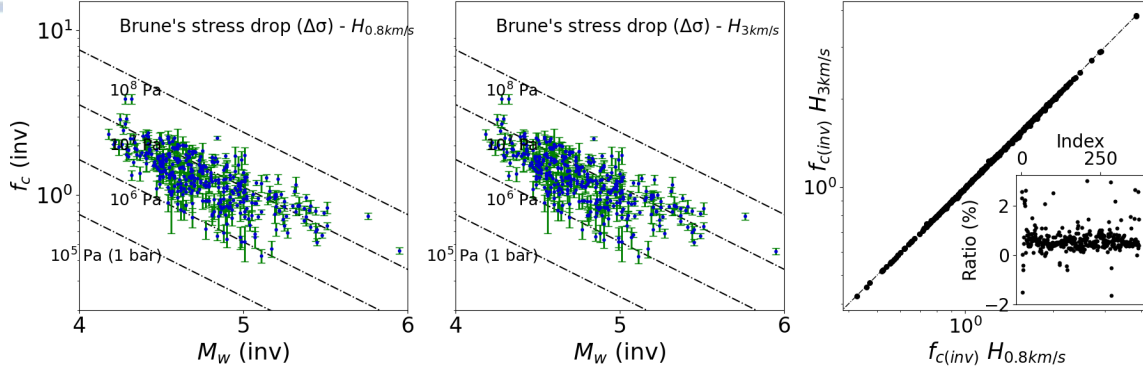


Figure 4.12: Comparison of the computed corner frequencies, f_c , and the inverted M_w , alongside with the Brune's stress drop lines. For engineering bedrock $H_{0.8\text{km/s}}$ (left) and seismological bedrock $H_{3\text{km/s}}$ (middle). On the right plot direct comparisons between the two bedrock delineations are presented, featuring the f_c for $H_{0.8\text{km/s}}$ and $H_{3\text{km/s}}$ with their bisector as a reference line, and the corresponding ratio (%) according to $\left(\frac{f_{cH_{3\text{km/s}}}}{f_{cH_{0.8\text{km/s}}}} - 1\right) \cdot 100\%$ versus the number of data.

From equation 2.11, that represents the relationship between seismic moment M_o and corner frequency f_c for each earthquake, the Brune's stress drop (Δ_σ) was calculated and plotted with the computed f_c and M_w in figure 4.12. The majority of the data fall in between 10 to 200 bar stress drop range, or 10^6 to $2 \cdot 10^7$ Pa. For $H_{0.8\text{km/s}}$ the Brune's stress drop line that describes the data best is $6.24 \cdot 10^6$, while for $H_{3\text{km/s}}$ is $6.13 \cdot 10^6$. As expected, there is noticeable homogeneity in f_c for both bedrock delineations as shown in figure 4.12(right). The disparities of the $H_{0.8\text{km/s}}$ versus the $H_{3\text{km/s}}$ are evident in the smaller plot that depicts the ratio between those bedrocks definition.

4.3.2.2 Attenuation Factors

In chapter 2.3 the second term of 2.5 and 2.6 represent the propagation path factor. This factor considered incorporates the three parameters characterising attenuation (Q_0 , γ , α) as described by equation 4.10:

$$P(r, f) = \exp\left(-\frac{\pi(rf)}{Q(f)V_s}\right) \left(\frac{1}{r}\right)^{\gamma_r} \quad (4.10)$$

where r the hypocentral distance, f the frequency, $Q(f)$ the frequency-dependent quality factor, which is mainly assumed as $Q(f) = Q_0 f^\alpha$, where Q_0 the quality factor

for $f = 1$ Hz and the parameter α . V_s the shear wave velocity and γ the distance-dependent geometrical spreading factor.

As previously noted, the area of Greece was divided into $n = 285$ distinct cells so that the segments of seismic rays could be individually studied for these subareas, spanning latitudes from $33.80^\circ N$ to $42.00^\circ N$ and longitudes from $19.2^\circ E$ to $29.2^\circ E$. Nevertheless, not all the seismic events rays cross every cell, but only 241 of them. The cells that were not intersected by no seismic ray were located along the boundaries of the defined area.

For those 241 subareas the frequency-dependent quality factor, $Q(f)$, was calculated from GIT analysis and plotted in figure 4.13, regardless of their uncertainties, in a coloured scale, for $H_{0.8 \text{ km/s}}$ (top) and for $H_{3 \text{ km/s}}$ (bottom) and for frequencies 0.5, 1 (Q_0) and 5 Hz (left to right). Similarly distributed, figure 4.14 displays the coefficient of variation (CV), which is presented as a percentage (%), quantifying the variability of data independently of the mean value. That means, the lower the CV value is, the higher the precision of the coefficient Q in the estimation of results. Finally, the smoothed Q values of figure 4.13 are depicted smoothed in figure 4.15, but only the $Q(f)$ values for $CV < 7\%$ are taken under consideration. In these maps an increase of the quality factor, $Q(f)$, with the increase in frequency is observed. One would expect that at greater frequencies, closer to the surfaced layers, the attenuation would be smaller. However, according to equation: $Q(f) = Q_0 f^\alpha$, an increase in frequency also causes an increase in quality factor $Q(f)$, but this doesn't imply, as shown in equation 4.10, that the attenuation will decrease.

However, the color scale in the above maps cannot accurately convey the differences in quality factor, Q , between $H_{0.8 \text{ km/s}}$ and $H_{3 \text{ km/s}}$. To enhance comprehension of the distribution of quality factor, $Q(f)$, across the assumed two bedrock cases, figure 4.16 (upper left plot) encompasses all values of $Q(f)$ generated by GIT, along with the bisector, which acts as a reference line to facilitate direct comparison of these values. The comparison between the factors derived from both approaches reveals a strong concordance across the entire frequency spectrum (0.3 to 15 Hz), evidenced by their close alignment with the bisector, while the ratio (%) according to equation: $\left(\frac{Q_{3 \text{ km/s}}}{Q_{0.8 \text{ km/s}}} - 1 \right) \cdot 100\%$, renders the variances better. Furthermore, the geometrical mean of Q_0 for the engineering bedrock is equal to $Q_0^{H_{0.8 \text{ km/s}}} = 62.986$ and for seismological bedrock $Q_0^{H_{3 \text{ km/s}}} = 63.163$. In upper right side of figure 4.16, the ratio of parameter α according to $\left(\frac{\alpha_{H_{3 \text{ km/s}}}}{\alpha_{H_{0.8 \text{ km/s}}}} - 1 \right) \cdot 100\%$, across each of the 241 subareas is presented. The geometrical mean of α for the two bedrock scenarios was estimated: $\alpha^{0.8 \text{ km/s}} = 0.719$ and $\alpha^{3 \text{ km/s}} = 0.717$.

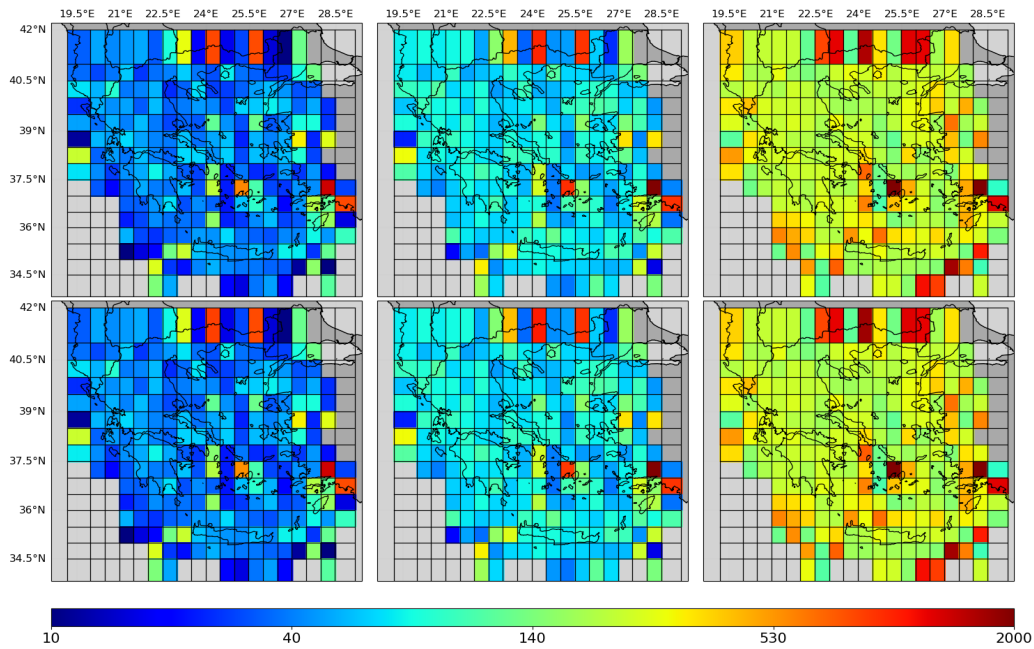


Figure 4.13: Maps corresponding to the computed $Q(f)$ for the frequencies 0.5 Hz (left), 1 Hz (middle) and 5 Hz (right). For $H_{0.8\text{km/s}}$ (top) and $H_{3\text{km/s}}$ (bottom)

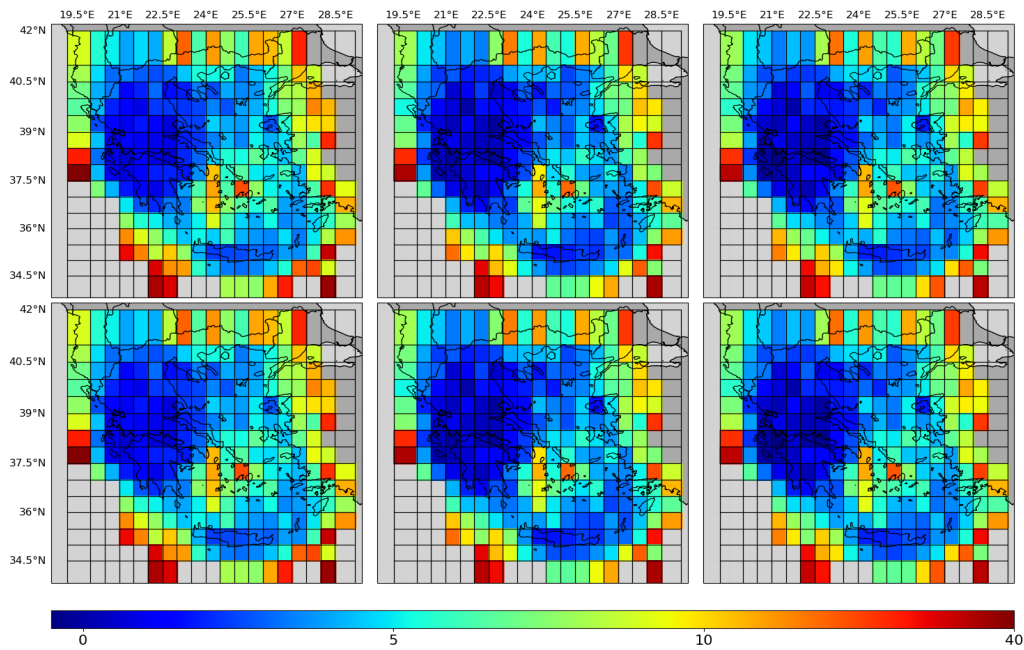


Figure 4.14: Maps corresponding to the uncertainties of $Q(f)$ for frequencies 0.5 Hz (left), 1 Hz (middle) and 5 Hz (right). For $H_{0.8\text{km/s}}$ (top) and $H_{3\text{km/s}}$ (bottom)

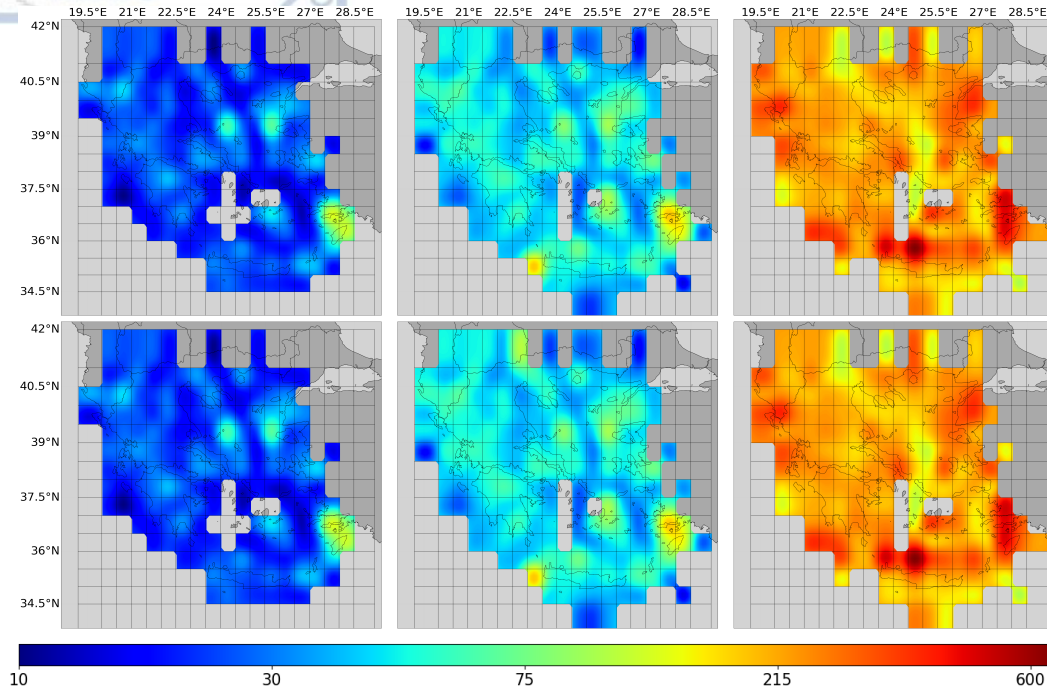


Figure 4.15: Maps corresponding to the smoothed values of $Q(f)$ with $CV \leq 7$ for frequencies 0.5 Hz (left), 1 Hz (middle) and 5 Hz (right). For $H_{0.8 \text{ km/s}}$ (top) and $H_{3 \text{ km/s}}$ (bottom)

In the lower part of figure 4.16 the spreading of parameter γ in relation to the epicentral distances is shown and, as mentioned previously, the value of γ varies across different epicentral distances, ranging from 10 to 300 km, in increments of 10 km. In the first 60 km, there is an almost linear increase in the geometric mean, γ , followed by a continuous decrease of the factor beyond this distance and a consistent increment of standard deviation. This phenomenon could be attributed to the properties of seismic wave propagation, as seismic waves travel through many interfaces and inhomogeneities, leading to increased attenuation or energy loss, resulting the decrease of γ beyond 60 km. Furthermore, an exponential decrease in the relative difference between $\gamma_{H_{3 \text{ km/s}}}$ and $\gamma_{H_{0.8 \text{ km/s}}}$ is observed. Overall, the geometrical mean of γ is: $\gamma_{0.8 \text{ km/s}} = 1.0089$ and $\gamma_{3 \text{ km/s}} = 1.0312$.

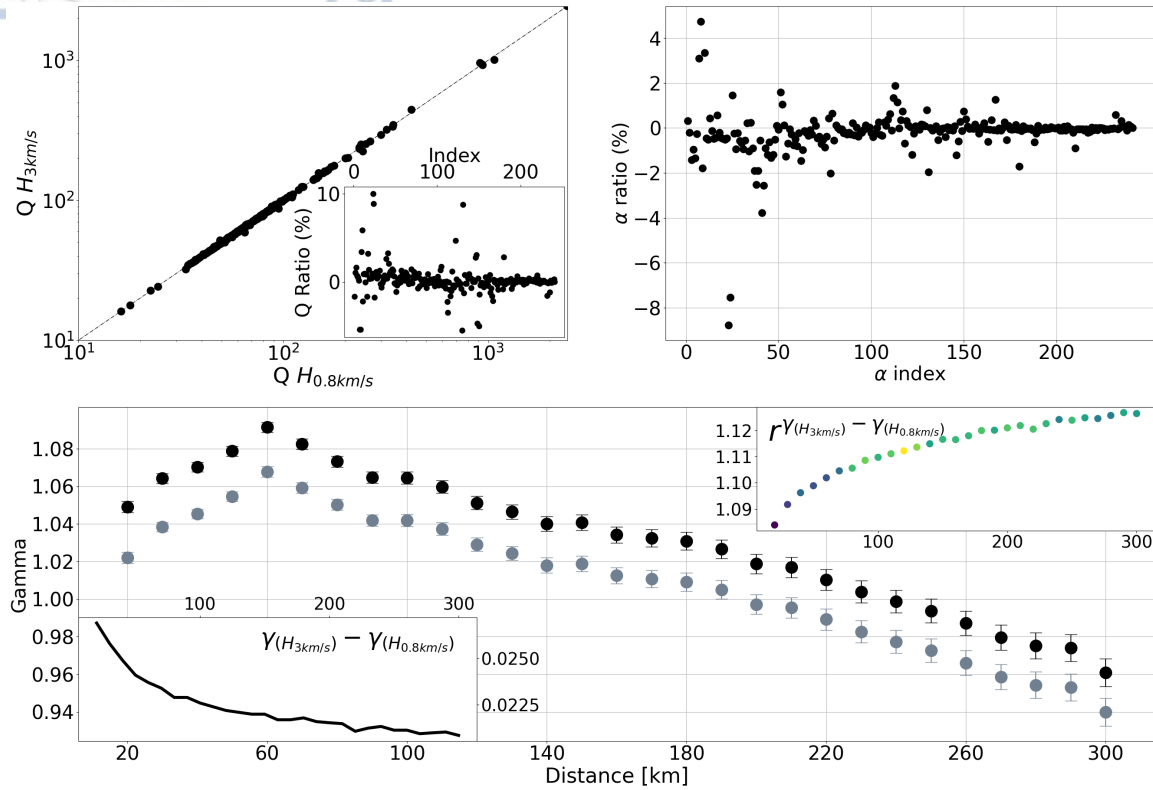


Figure 4.16: Comparison of the quality factor, Q_0 for $H_{0.8\text{ km/s}}$ and $H_{3\text{ km/s}}$. The dashed line represents the bisector as a reference line. Inner plot: Q_0 ratio (%) for each of the 241 studied subareas. b) The ratio of α (%) for each of the 241 studied subareas. c) Comparison of geometrical spreading coefficient, γ for $H_{0.8\text{ km/s}}$ (grey points) and $H_{3\text{ km/s}}$ (black points) with \pm std. Inset lower plot: The relative difference between $\gamma_{3\text{ km/s}}$ and $\gamma_{0.8\text{ km/s}}$. Inset upper plot: The relative difference between $\gamma_{3\text{ km/s}}$ and $\gamma_{0.8\text{ km/s}}$ amplify with increasing epicentral distance, r , while the colorbar represents the number of seismic rays at each distance r .

4.3.2.3 Site Amplification Factors (SAFs)

Apart from estimating the source and path factors, GIT simultaneously calculated the horizontal and vertical site amplification factors, HSAFs and VSAFs, respectively. Of great interest were the results of the Site Amplification Factors (SAFs) comparing the two cases, for seismological and engineering bedrock. In the inverted site factors, although the site amplification presents the same shape throughout the entirely frequency range, a deamplification is observed for parameters corresponding with the S-wave SAFs for $H_{0.8\text{ km/s}}$. In figure 4.17, the HSAFs are presented, for same stations scattered in the area of Greece.

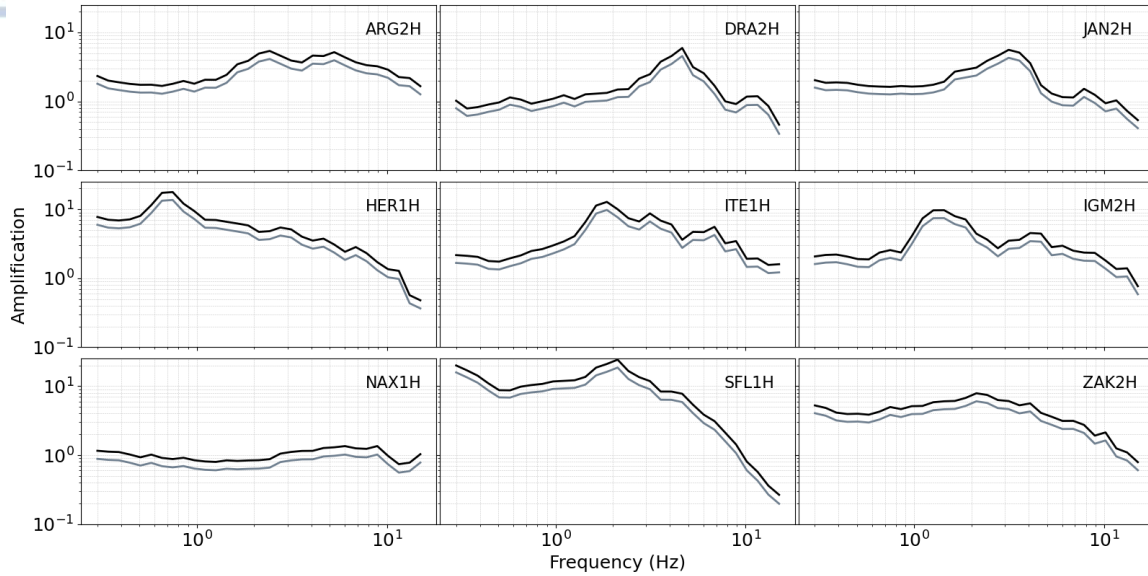


Figure 4.17: The Horizontal Site Amplification Factors (HSAFs) at 9 selected stations all over Greece for $H_{3\text{km/s}}$ (black line), and $H_{0.8\text{km/s}}$ (grey line).

An almost constant increase in amplification of about 30% is observed in SAFs derived from GIT analysis across the whole frequency range when extending down to seismological bedrock, $H_{3\text{km/s}}$. The noted deamplification for $SAFs_{0.8\text{km/s}}$ in the site parameter outcomes, may be, partially, attributed to the computed geometrical spreading parameter, γ , being slightly lower when inversion takes place for $H_{0.8\text{km/s}}$, as shown in the lower plot in figure 4.16. But most possible is due to the differences spotted in site spectral amplification factors of horizontal component created by the V_{PZ} , V_{SZ} and ρ_Z profiles of the six reference stations from 'HV-inv' software. The ratio of Horizontal $SAF^{theoretical}$ ($\frac{HSAFs_{3\text{km/s}}^{theoretical}}{HSAFs_{0.8\text{km/s}}^{theoretical}}$) is depicted in figure 4.18 (middle) where the black solid curve is the geometrical mean of six calculated ratios. Likewise, the ratios of HSAFs derived from GIT analysis ($HSAFs^{GIT}$) for are shown in figure 4.18 (top), where the faint red lines are the ratios of $HSAFs^{GIT}$ for seismological bedrock divided by the $HSAFs^{GIT}$ for engineering bedrock ($\frac{HSAFs_{3\text{km/s}}^{GIT}}{HSAFs_{0.8\text{km/s}}^{GIT}}$), and the red solid line represents the geometrical mean of all 152 ratios. The geometrical mean ratios calculated from $HSAFs^{theoretical}$ (black) and $HSAFs^{GIT}$ (red) ratios were plotted together in the the lower part of 4.18, exhibiting similar trend, as the least square analysis confirms (green line).

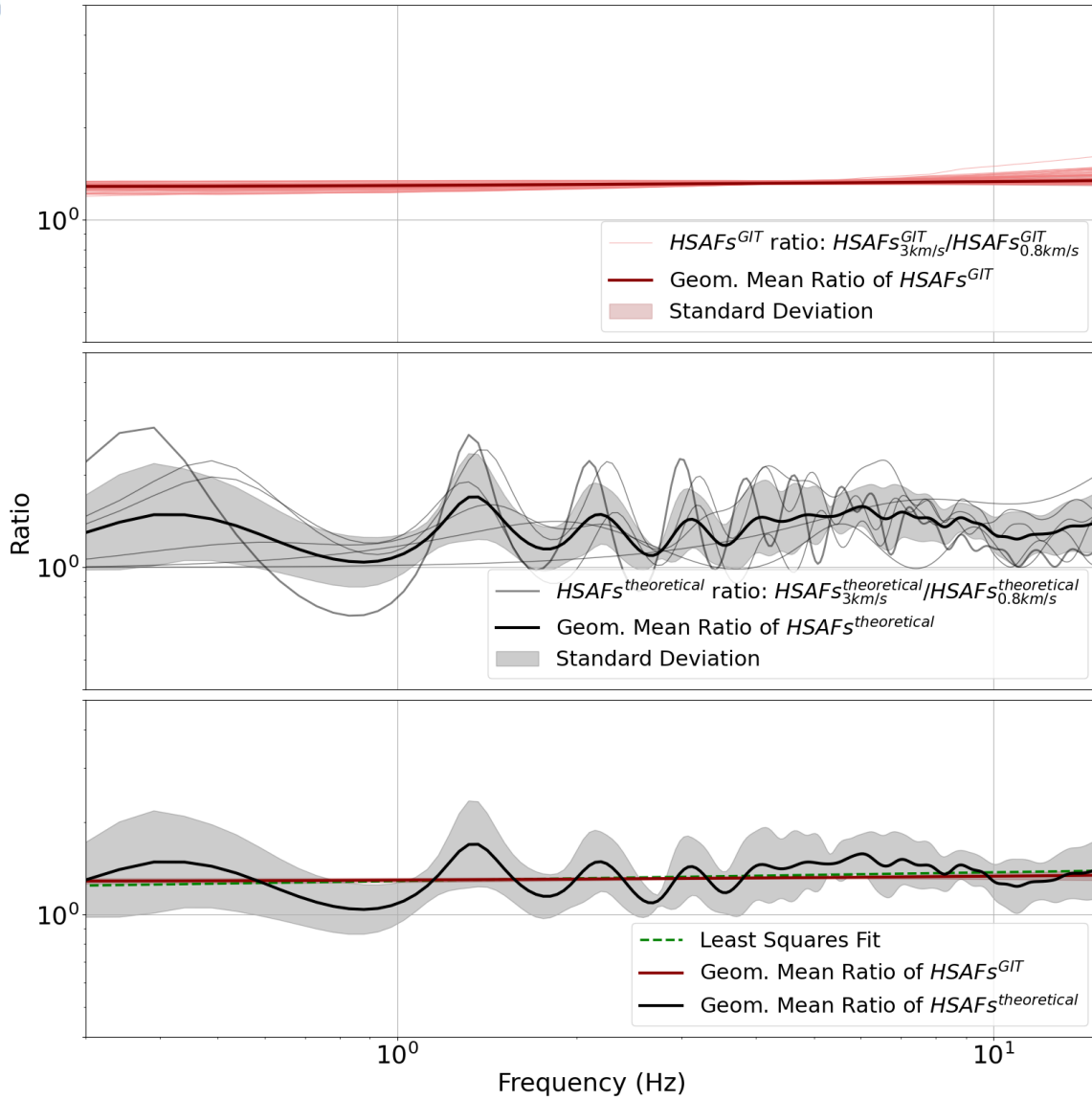


Figure 4.18: Top: $HSAFs^{GIT}$ ratios ($HSAFs_{3\text{km/s}}^{GIT}/HSAFs_{0.8\text{km/s}}^{GIT}$) with the geometrical mean of that ratio and \pm a standard deviation. Middle: $HSAFs^{theoretical}$ ratios ($HSAFs_{3\text{km/s}}^{theoretical}/HSAFs_{0.8\text{km/s}}^{theoretical}$) derived from the 1D- V_{SZ} profiles of the six reference stations with the geometrical mean of that ratio and \pm a standard deviation. Bottom: The above mentioned geometrical means and the corresponding std alongside with the least squares fit (green dashed line).

A general correlation analysis of the amplitude characteristics between HSAF and VSAF obtained from the GIT, is profitable. Specifically, figure 4.19 illustrates the

comparison of the maximum (peak) amplitude of HSAF as a function of peak amplitude of VSAF (left) and the geometrical average amplitude of HSAF as a function of the geometrical average amplitude of VSAF (right). From these two figures, it is evident that when peak amplitudes is plotted, VSAF is $\sim 40\%$ of HSAF, whereas when average amplitude is plotted, VSAF is $\sim 43\%$ of HSAF. However, the correlation coefficient (R^2) in the case of the average amplitude correlation is evidently higher, since the data are not so scattered.

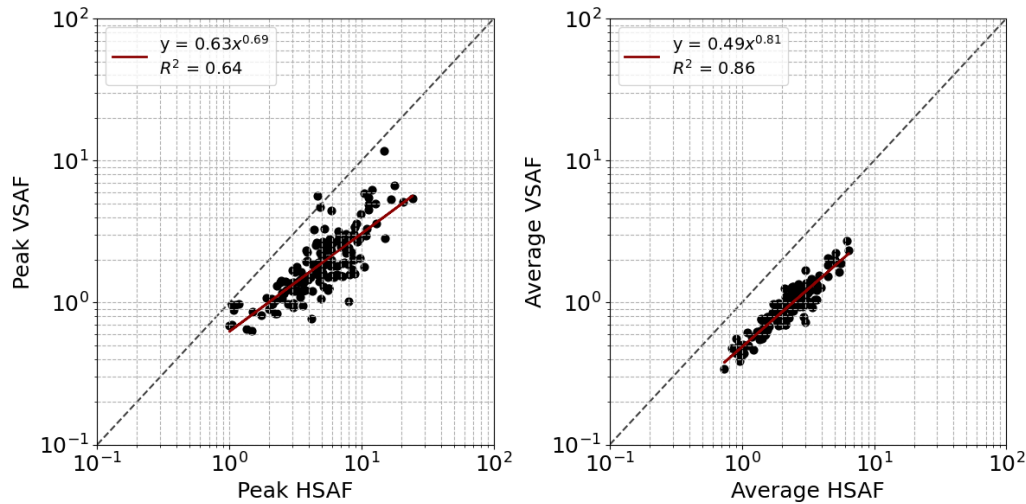


Figure 4.19: HSAF and VSAF correlation obtained by GIT regarding the maximum amplitudes (left) and the geometrical average amplitudes (right) for the 152 stations. The linear regression lines and the regression coefficients are depicted, as well as the correlation coefficient, R^2 .

Similarly, the comparison between HSAF and eHVSR is conducted to identify any potential correlation between these variables. The analysis includes comparisons of both the peak amplitude and the log-average amplitude, as well as a more direct comparison of the Fourier spectral amplitudes at 0.5, 1, 2, and 5 Hz, depicted in figure 4.20. Generally, it was observed that the HSAF values were consistently higher than eHVSR, while the correlation between these two is quite weak, especially at 5 Hz. Therefore, eHVSR cannot be considered a reliable proxy for HSAF at most sites that have been studied. This leads to the conclusion that a factor is needed to adjust the measured eHVSRs, thereby obtaining the accurate HSAFs.

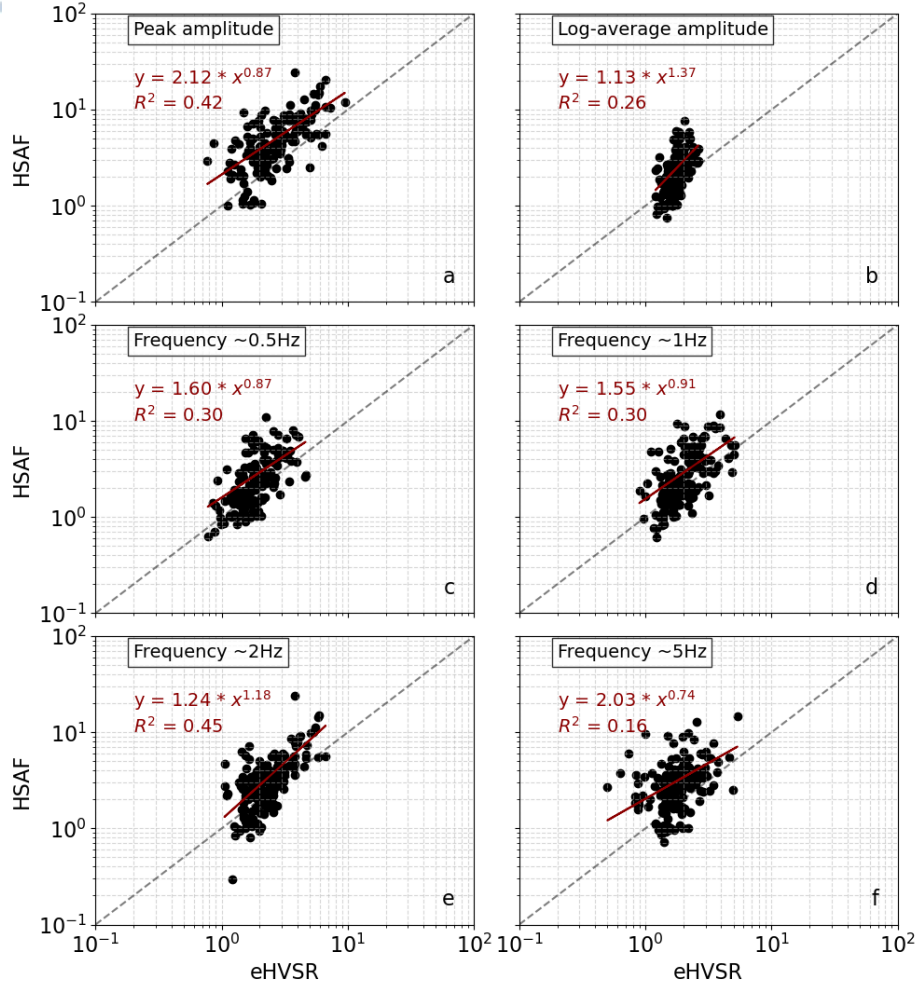


Figure 4.20: HSAF obtained by GIT and eHVSr correlation in regards to (a) the maximum amplitudes and (b) the geometrical average amplitudes for the 152 stations. Furthermore, the linear regression lines and the regression coefficients are depicted, as well as the R^2 .

Furthermore, in equation 2.6 the third term, $V_b H_b R$ is the inverse of the horizontal-to-vertical spectra ratio and it is used to convert the amplitude of horizontal S-waves into vertical P-waves. $V_b H_b R$ is essential because the main portion of wave energy is encompassed in S waves, which were being scattered through the medium where seismic waves travel, from the depth $H_{3\text{km/s}}$ until the surface. $V_b H_b R$ estimation requires both the observed on surface eHVSr data and the theoretical HSAF and VSAF calculated for the reference stations, and it is expressed as follows (Ito et al., [33]):

$$V_b H_b R = \frac{eVHSR}{VSAF} \times HSAF \quad (4.11)$$

where eVHSR is the inverse observed horizontal-to-vertical spectra ratio. Ito et al. [33] emphasize that the estimation of the observed S-wave spectra must be made at least until the S-wave velocity reaches 3 km/s or higher, as the DFA theory is assumed to be valid up to the seismological bedrock. The latter study estimated a theoretical value for $V_b H_b R \approx 0.76$. In the present study a log-average $V_b H_b R$ have been calculated for each reference station with respect to engineering bedrock (figure 4.21a) and seismological bedrock (figure 4.21b). These log-average values are presented in both figure with black solid lines and their respective values are given in y axis.

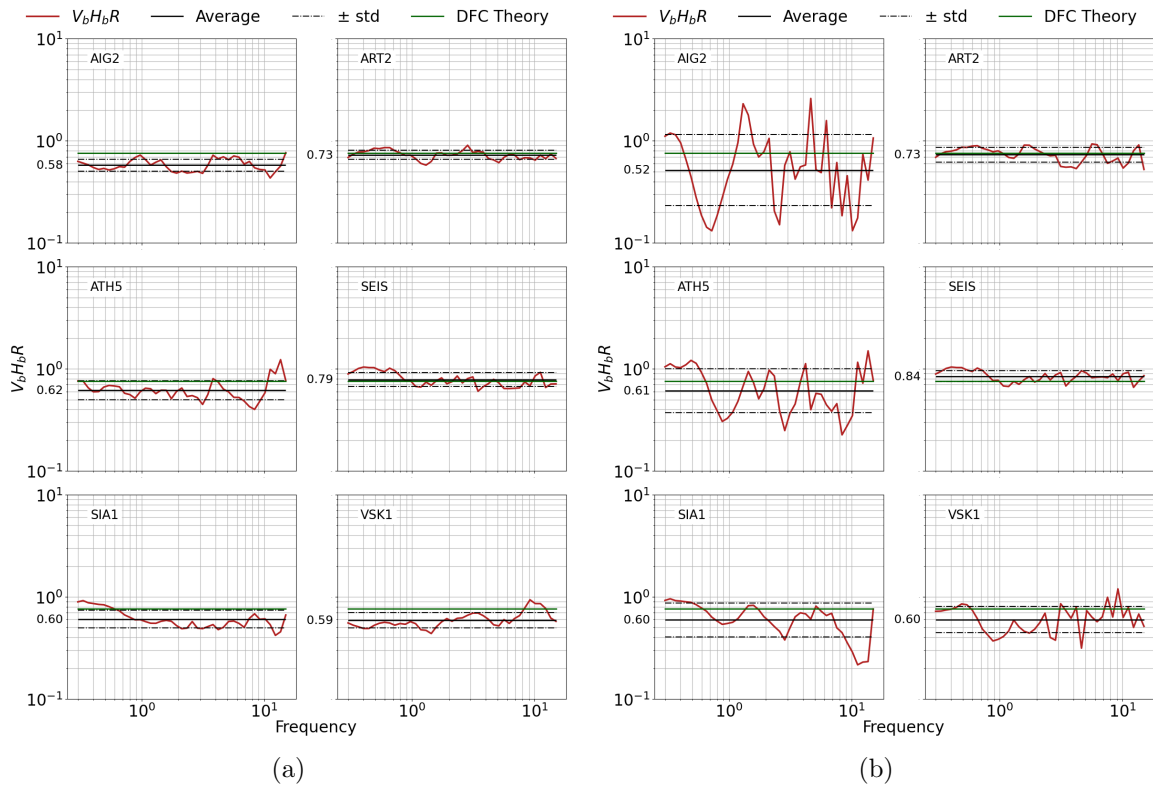


Figure 4.21: Comparison of $V_b H_b R$ curves for engineering and seismological bedrock. (a) The $V_b H_b R$ curve (red) for all six reference stations down to engineering bedrock ($H_{0.8 \text{ km/s}}$) alongside with their geometrical average (black line) with $\pm 1std$ (dashed black line). Green line: the theoretical solution from the diffuse field assumption (DFA). (b) The $V_b H_b R$ curve (red) for all six reference stations down to seismological bedrock ($H_{3 \text{ km/s}}$) alongside with their geometrical average (black line) with $\pm 1std$ (dashed black line). Green line: the theoretical solution from the diffuse field assumption (DFA).

4.3.3 Vertical Amplification Correction Functions (VACFs)

Ito et al. [33] determined empirical correction functions that allow the estimation of Horizontal Site Amplification Factors (HSAFs) using only the calculated

Horizontal-to-Vertical Spectral Ratios of earthquake recordings (eHVSr), called vertical amplification correction functions (VACFs). At an arbitrary site, HSAF can be expressed as a function of VACF as follows:

$$HSAF = eHVSr \times VACF \quad (4.12)$$

where eHVSr the observed ratio on surface.

VACFs were calculated, separately, for every station according to equation 4.12. Based on the peak amplitude (A_p) and the peak frequency (f_p) of each station in the observed eHVSr data, VACFs were divided into eight categories. The categorization, as it depicted in figure 4.22a indicates that the coefficient varies for each category, with the most significant differences of VACFs observed for frequencies between 1 and 10 Hz. This variability may be partially attributed to the small number of sites in some categories, as shown in Appendix Table A.1. Moreover, categories were defined based on the peak amplitude and the peak frequency of the empirical Vertical-to-Horizontal Spectral Ratio (eVHSR), which is essentially $eVHSR = 1/eHVSr$. However, stations were categorized into only four out of ten categories, as shown in Figure 4.22b and in Appendix Table A.2.

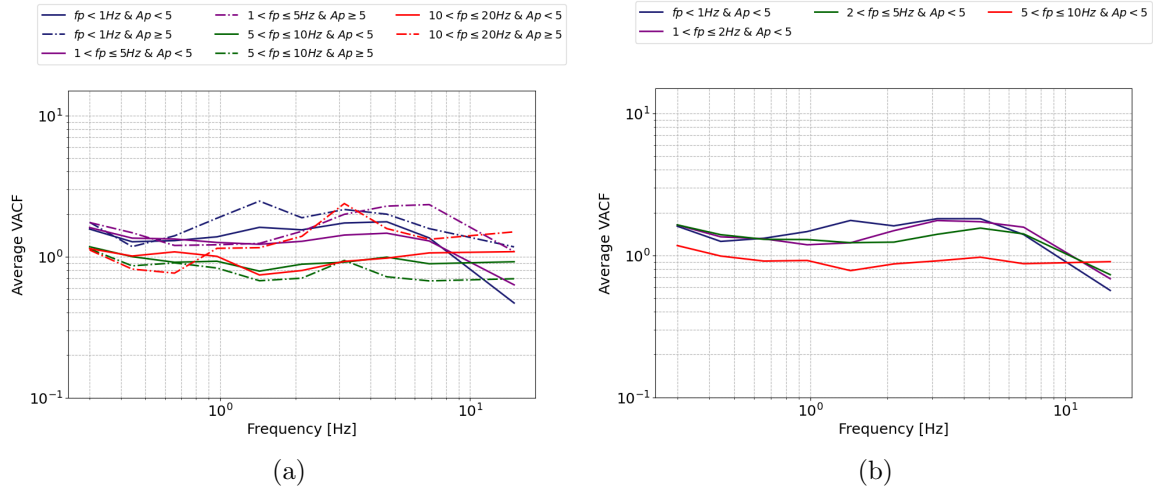


Figure 4.22: Left: Log-average VACFs for eight site categories classified by the maximum eHVSr, where f_p is the peak frequency and A_p the corresponding peak amplitude. Right: Log-average VACFs for ten site categories classified by the maximum eVHSR, where f_p is the peak frequency and A_p the corresponding peak amplitude. Stations were categorized into only four of the ten categories.

Figure 4.23 presents the maximum and average values of both simulated HSAF and the observed eHVSr in comparison to the observed HSAF from GIT in the first

two top plots. Additionally, the figure includes comparisons of FAS values at 0.5 Hz, 1 Hz, 2 Hz, and 5 Hz, respectively, in the subsequent plots. Simulated HSAFs were calculated according to equation 4.12.

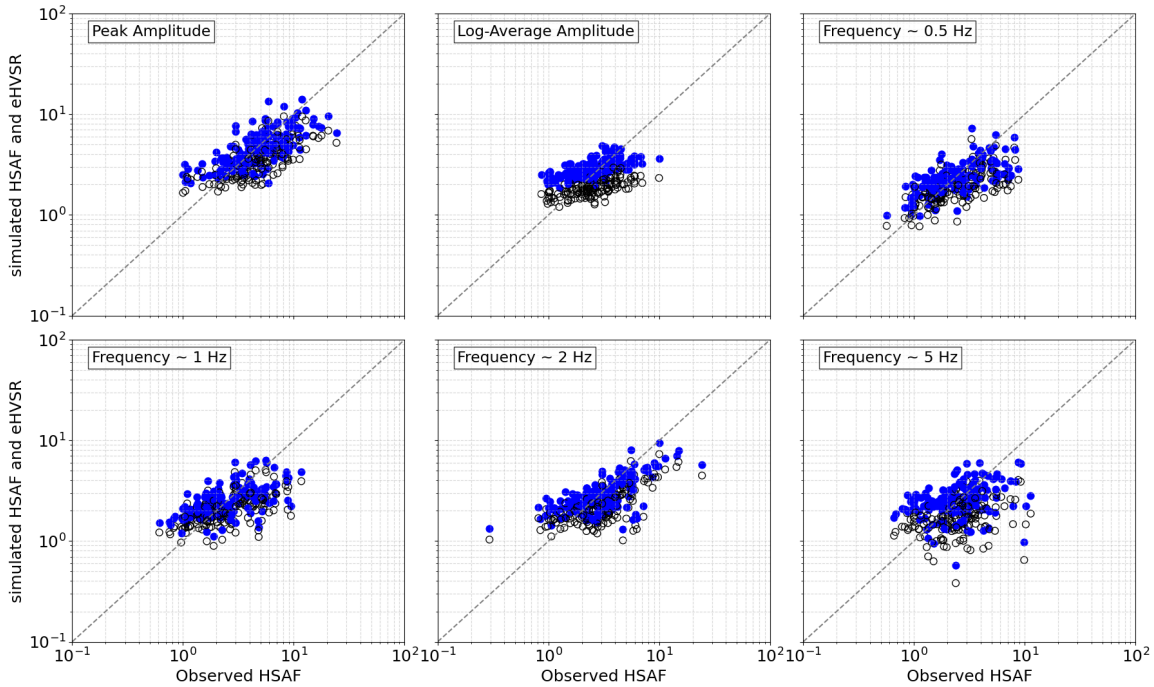


Figure 4.23: Simulated HSAFs according to equation 4.12 (blue circles) and the observed on the surface eHVSRs (open circles) versus the calculated HSAFs from GIT analysis. From left to right the horizontal axis for peak amplitude and in the Fourier spectral amplitudes at 0.5, 1.0, 2.0 and 5 Hz.

Ito et al. [33] estimated the VACFs for 1678 Japanese sites, recorded more than seven earthquakes at each location. Computed HSAFs for seismological bedrock were employed to VACFs calculations at each station site. The goal is to determine the logarithmic average of these values and to juxtapose them with the VACFs values presented by [33] in figure 4.24. While there is a consistency in VACF results between both studies for the frequency range of 0.7 Hz to 7 Hz, deviations were notably outside this range. Specifically, the log-average VACF for frequencies below 0.7 Hz exhibits amplification, diverging from the results by [33], and, similarly, for frequencies above 7 Hz, the VACF calculated in this study presents a deamplification compared to the log-average VACF for the Japanese sites.

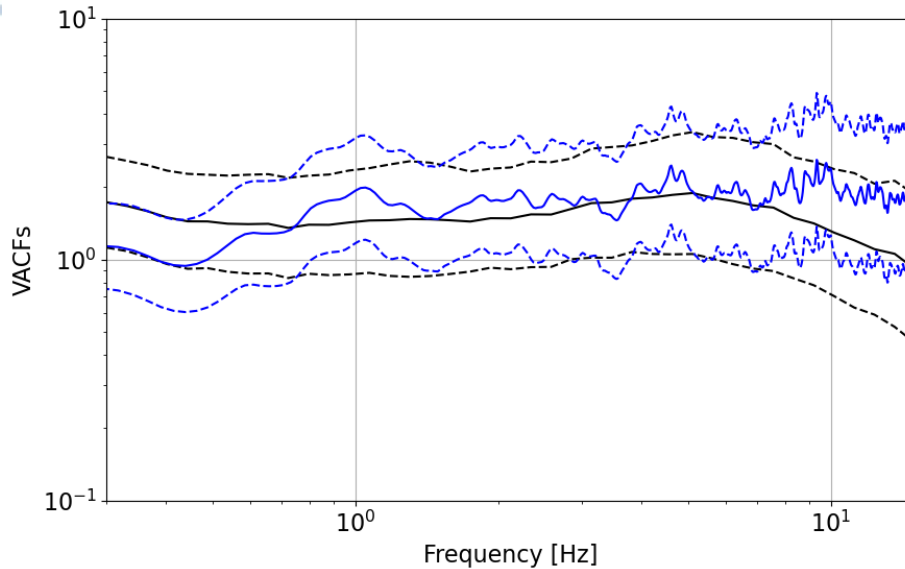


Figure 4.24: Variation of the logarithmic average empirical VACF for all 152 stations (black curves) $\pm std$, in comparison with the curves calculated for Japanese data (blue curves) $\pm std$, by Ito et al., [33]

Since the above comparison presented both positive and diverted results, the logarithmic average VACF was also calculated for all 152 sites grouped by soil type according to the current EC8 [1] in figure 4.25; a detailed analysis of the current EC8 will be discussed in section 4.4.1. The log-average VACF for category A (see Table 4.14) differs from categories B and C, since it aligns better with the VACFs calculated by Ito et al. [33]. At lower frequencies the curve approaches unity while increasing frequency, VACF value also increases. In contrast, for categories B and C, the log-average VACF is higher than that for category A at lower frequencies, while a characteristic drop of VACF for frequencies higher than 5 Hz is observed.

To validate the evaluation results of VACFs, simulated horizontal site amplification factors (sHSAFs) were computed according to equation 4.12, at two stations in Greece: the ARGONET+ station (CK0) (Grendas et al., [30]) and a *EUROSEIS-TEST* project station (TST) (Raptakis et al., [68]), both of them not included in present's study GIT analysis. For sHSAFs calculation at both stations, the log-average VACF (figure 4.24 black line) was used including the standard deviation, and then, they were compared with the SAF, with respect to the nearby surface rock (reference) sites, CKWP and PRO for stations CK0 and TST, respectively, using the Standard Spectral Ratio (SSR) method (Borcherdt, [13]). The corrected SSRs were estimated by multiplying the simulated HSAFs of the reference stations, according to equation 4.12 with the real SSRs measurements in CK0 and TST. The corrected SSRs were compared against the sHSAF and eHVSF, as presented in figure 4.26a and 4.26b.

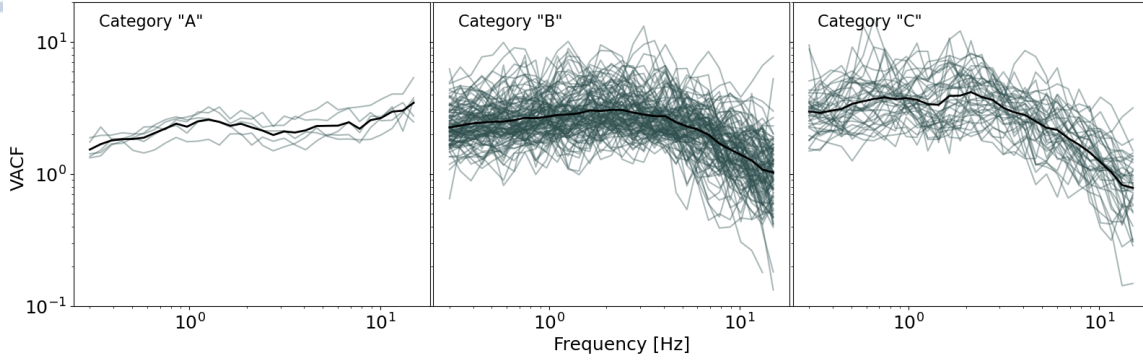


Figure 4.25: Variation of the logarithmic average VACF (black curve) for all 152 stations (green curves) divided by the type per soil of each site according to the current EC8.

Ideally, sHSAFs and corrected SSRs should converge as much as possible. However, for both station stations, between the fundamental frequency and the second harmonic a distinguished discrepancy is observed. These differences could be partly attributed to the complexity of the actual geology of sites. When calculating the simulated HSAF the sites are assumed to be 1D when in reality there are not. Between the fundamental frequency and the second harmonic surface waves dominate the seismic response. The SSR curve inherently includes the surface wave response while the simulated HSAF does not.

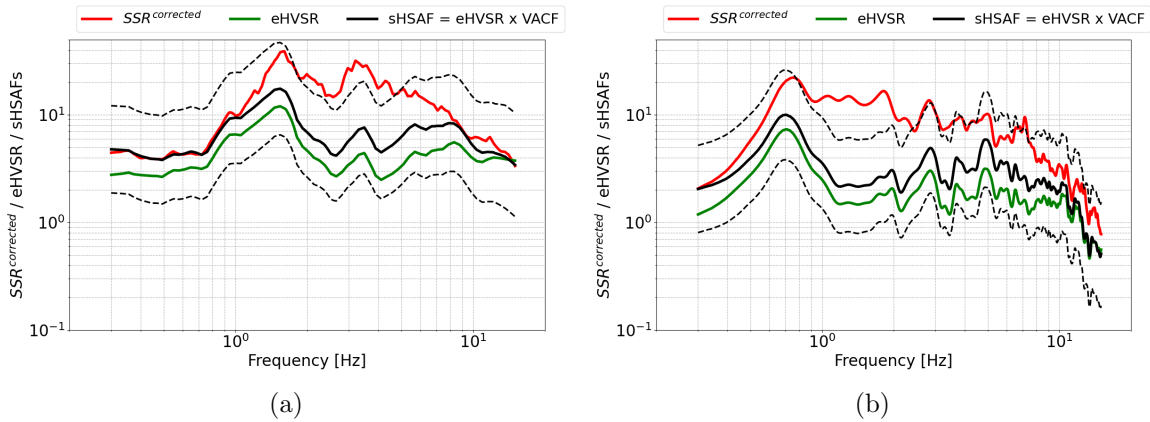


Figure 4.26: Comparison of simulated HSAFs by employing the log-average VACF and its calculated standard deviation (black lines), the simulated HSAF based on the peak amplitude (A_p) and peak frequency (f_p) in observed eHVSR data (green line), the corrected SSR (red line), and the eHVSR (green line) at stations CK0 (left) and TST (right).

Kawase et al. [41] proposed a novel method by which the eHVSR can be empir-

ically calculated from the horizontal-vertical spectral ratio of ambient noise recordings (mHVSR). This is achieved using the observed spectral ratio between eHVSR and mHVSR at the same reference site, referred to as earthquake-to-microtremor ratio, EMR. Consequently, calculation of VACFs could be used to blindly estimate the HSAF at a site, based solely on eHVSR, while calculating EMR a double correction could be succeeding by estimate the mHVSR at a site. In figure 4.27 the EMRs of each station, following this equation: $EMR = \frac{eHVSR}{mHVSR}$, is plotted and an additional logarithmic mean have been calculated (black curve).

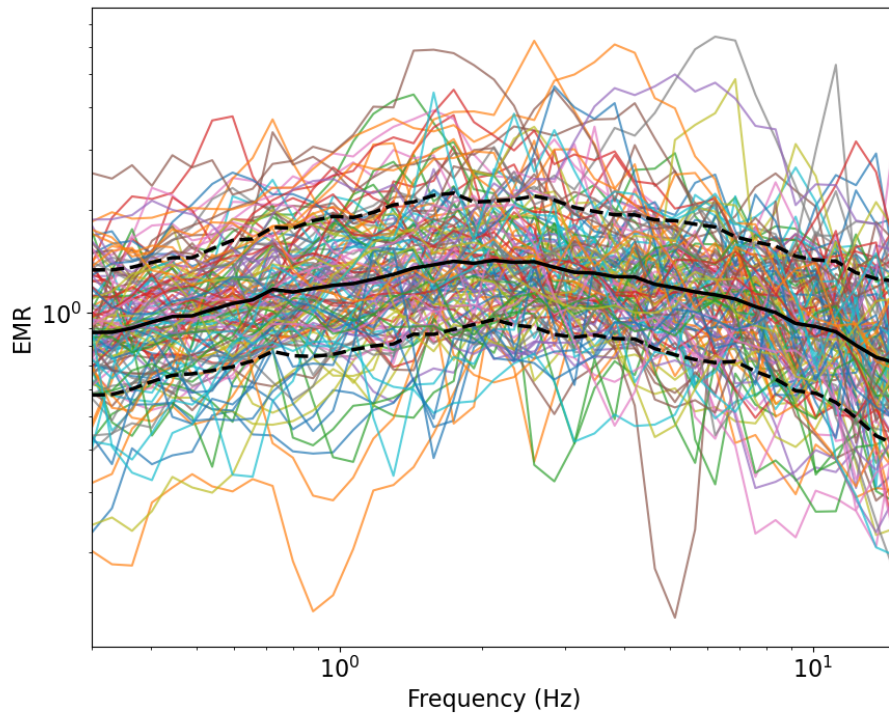
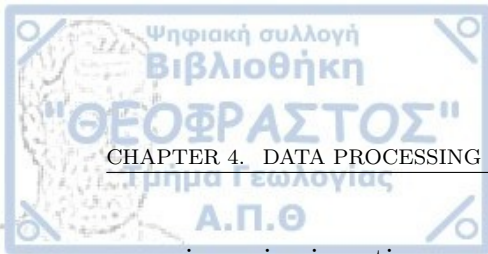


Figure 4.27: Earthquake-to-microtremor ratio, EMR for each out of 152 stations (coloured lines) alongside with the logarithmic mean and $\pm 1std$ (black solid and dashed lines)

4.4 Soil type categorisation according to Eurocode 8 (EC8) and comparison with SAFs

Eurocode 8 (EC8) was designed, specifically, to address the structural design of buildings and infrastructure design to withstand seismic actions, in order to ensure their safety and minimize human and property loss. EC8 plays a crucial role in



assessing seismic actions and their impact on structures by its detailed and effective site categorization model. Eurocode 8 (CEN 2004[1], Part 1) is the in force code that implements a simple site classification model, based on the average velocity of Shear waves in the top 30 meters of soil, known as V_{S30} . In 2024 a draft the previous version was updated by including more parameters and two different proxies for site categorization. In the present dissertation, the HSAFs derived from GIT down to engineering bedrock, were utilized for site categorization per soil type according to the current EC8 and EC8 2024 draft.

4.4.1 Categorisation according to the current EC8

Current EC8, as mentioned, follows a simple categorization based on the V_{S30} and local geology, distinguishing five soil categories presented in Table 4.14. So in order to categorise all 152 station site the V_{S30} values were required. Most of these values were sourced from the I.T.S.A.K. database, derived from in-situ geophysical measurements (borehole) while others were estimated based on the site's geology and a preferred V_{S30} for analysis was established with a standard deviation. However, in sites where such data do not exist but only the age of the formations were available, Stewart et al. [79] study were utilized. [79] used 314 sites and classified them into five major age groups (Holocene, Pleistocene, Mapped Quaternary, Tertiary: Neogene, Mesozoic and Paleozoic) using 1:50,000 IGME maps. Subsequently, a V_{S30} estimation procedure was developed, based on geology and gradient data. For each geological time period, a V_{S30} per approximately 100 years was calculated, accompanied by a logarithmic error.

Table 4.14: Site categorisation according to the EC8 (CEN 2004[1]).

| Ground Type | Description of stratigraphic profile | V_{s30} (m/s) |
|-------------|---|-----------------|
| A | Rock or other rock-like geological formation, including at most 5 m of weaker material at the surface. | > 800 |
| B | Deposits of very dense sand, gravel, or very stiff clay, at least several tens of metres in thickness, characterised by a gradual increase of mechanical properties with depth. | 360-800 |
| C | Deep deposits of dense or medium-dense sand, gravel or stiff clay with thickness from several tens to many hundreds of metres. | 180-360 |
| D | Deposits of loose-to-medium cohesionless soil (with or without some soft cohesive layers), or of predominantly soft-to-firm cohesive soil. | < 180 |
| E | A soil profile consisting of a surface alluvium layer with V_s values of type C or D and thickness varying between about 5m and 20m, underlain by stiffer material with $V_s \geq 800$ m/s. | |

Based on the calculated V_{S30} values and accounting for their associated errors, the sites were categorized according to Table 4.14. Although, EC8, typically, proposes five categories in total, the available data allowed for classification into only three of these categories. Only the six reference stations used in this study was classified as category A, while the majority of sites were grouped to category B, and several in the category C. While the errors were used in the classification, creating a range of values for V_{S30} , they did not contribute to the final results. In figure 4.28, the V_{S30} versus the fundamental frequency, f_0 , is depicted for all 152 stations, while each colour represent a different category based on current EC8. The calculation of f_0 is analyzed in section 4.4.2, while its values at each station are given in the Appendix table A.4.

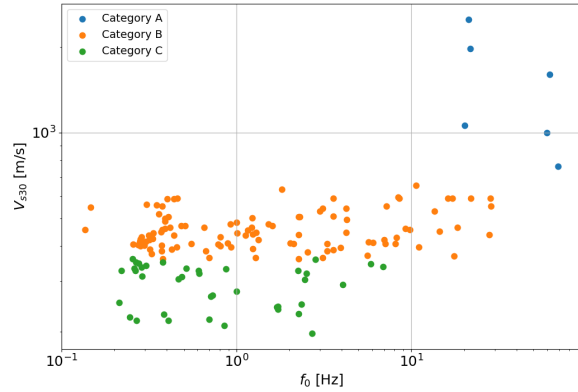


Figure 4.28: Colour representation of the categorization of sites according to the current EC8 in a V_{S30} versus fundamental frequency (Hz) plot.

Following Paolucci et al. [64] study, in the left side of figure 4.29 a comparison amplification factors according to the current EC8 and ground-motion models (GMMs) by Boore et al.[12]. For the GMMs calculations, several fixed parameters must be established. Such as the moment magnitude, M_o , that was set to 5.8, the highest ground motion value recorded on surface. The type of fault was identified as normal, the period range was defined from 0.01 s to 4 s and the predicted PGA was defined at $\sim 0.4g$. Additionally, the Joyner and Boore distance (R_{jb}), which is the shortest distance from the site to the projection of the rupture on the surface, was set at 100 km to mitigate nonlinear behaviors. The GMMs were calculated four times based on the V_{S30} values, which were defined hinge on the four categories according to the EC8. GMMs and amplification factor in category A are identical, while for category B the range of GMMs include the amplification factors proposed by the EC8. The trend of GMMs and amplification factors were the same in categories C and D, but there were notable dissimilarities in amplification.

In the right-hand side of 4.29 the amplification factors according to the current EC8, alongside with the HSAFs of each category derived by the GIT are presented. As mentioned before, there is a noteworthy clustering of HSAFs in category B. In category A, mean HSAF and amplification factors show good convergence, while for category B, mean HSAF presents slightly higher amplification. For category C mean HSAF and amplification factors according to EC8 present even higher amplification values from category B and deviate more from EC8 amplification factors.

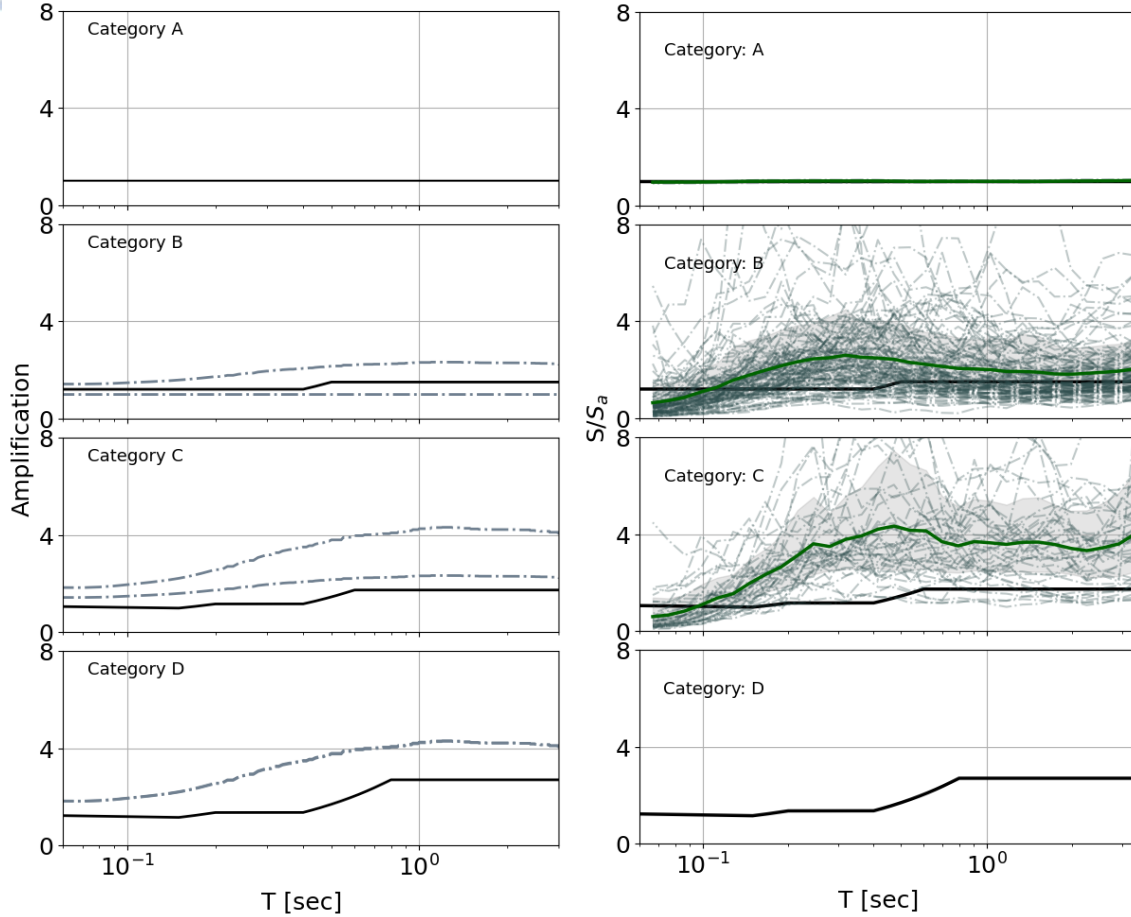


Figure 4.29: Left: Upper and lower limits of period-dependent site amplification factors for $V_{s30} = 0.8$ km/s for category A, for category B 360 m/s $\leq V_{s30} < 0.8$ km/s , 180 m/s $\leq V_{s30} < 360$ m/s for category C, and 150 m/s $\leq V_{s30} < 180$ m/s for D, according to the GMMs by Boore et al.[12] (grey dashed dotted lines) alongside with the corresponding amplification factors according to the current EC8 (black lines). Right: Amplification factors according to the current EC8 (black lines), considering high seismicity regions. And the HSAF (green dashed dotted lines) with the estimated logarithmic mean (green curve) and $\pm 1std$

4.4.2 Categorisation according to EC8 2024 draft

Recognizing that classification based on V_{s30} alone does not adequately capture the diverse site amplification effects observed in real geological profiles (Lee and Trifunac, [47], among others), in 2024 a new draft EC8 proposed, which introduced two parameters for site categorization: H_{800} and $V_{s,H}$. $V_{s,H}$ is the quotient of the depth (H) of seismological bedrock in a site and the sum of the thickness (h_i) divided by the shear wave velocity (V_i) in each layer in the geological structure, and it is expressed

as follows: $V_{s,H} = \frac{H}{\sum_{n=1}^N \frac{h_i}{V_i}}$, where N the sum of soil layers overlying the engineering bedrock.

Table 4.15: Standard site categorisation according to 2024 draft of EC8 .

| | Ground Class | Stiff | Medium Stiffness | Soft |
|--------------|---|--|---|---|
| Depth class | V_{sH} range H_{800} | $400 \text{ m/s} \leq V_{sH} < 0.8 \text{ km/s}$ | $250 \text{ m/s} \leq V_{sH} < 400 \text{ m/s}$ | $150 \text{ m/s} \leq V_{sH} < 250 \text{ m/s}$ |
| Very shallow | $H_{800} \leq 5 \text{ m}$ | A | A | E |
| Shallow | $5 \text{ m} < H_{800} \leq 30 \text{ m}$ | B | E | E |
| Intermediate | $30 \text{ m} < H_{800} \leq 100 \text{ m}$ | B | C | D |
| Deep | $H_{800} > 100 \text{ m}$ | B | F | F |

Table 4.16: Site categorisation based on $V_{s,H}$ and f_0 according to EC8 2024 draft.

| Combination of f_0 (Hz) and $V_{s,H}$ (m/s) | Site Category |
|--|---------------|
| $f_0 > 10$ and $V_{s,H} \geq 250$ | A |
| $f_0 < 10$ and $400 \geq V_{s,H} < 800$ | B |
| $V_{s,H}/250 < f_0 < V_{s,H}/120$ and $250 \geq V_{s,H} < 400$ | C |
| $V_{s,H}/250 < f_0 < V_{s,H}/120$ and $150 \geq V_{s,H} < 250$ | D |
| $V_{s,H}/120 < f_0 < 10$ and $150 \geq V_{s,H} < 400$ or | E |
| $f_0 > 10$ and $150 \geq V_{s,H} < 250$ | E |
| $f_0 < V_{s,H}/250$ and $150 \geq V_{s,H} < 250$ | F |

Site categorization can be conducted using Tables 4.15 and 4.16 of EC8 2024 draft. Table 4.15 serves as the main reference, providing the standard site categorization according to the 2024 draft of EC8, while Table 4.16 categorizes sites based on $V_{s,H}$ and f_0 . Therefore, in order to complete the classification of sites based on those Tables, three parameters were calculated: the

fundamental frequency f_0 , the depth H of engineering bedrock at the 146 stations, since the rest six site were already knows as reference sites and the H have been calculated through the 'HV-inv' method, and the $V_{s,H}$ at the engineering bedrock. As detailed in Chapter 3.3, ambient noise measurements (mHVSR) obtained from accelerometer-sensitivity and velocity-sensitivity instruments were employed, taking into account coda waves windows from earthquake waveforms to determine eHVSR and the f_0 at each site. However, calculating the thickness of layers down to seismological bedrock was more complex. The widely used relation 4.2 facilitated these calculations.

With f_0 available, a range for $V_{s,H}$ was set from 150 m/s until 790 m/s. For each site, the two extreme values of H and a logarithmic average were calculated, along

with any associated errors from prior calculations. Similarly, using 4.2, a range of the average velocity $V_{s,H}$ was calculated. With all necessary data available, sites have been categorized combining both Tables (4.15, 4.16). However, due to the broad range of parameter values, some sites have fallen into two different classes, and, also, discrepancies between the two Tables have been observed (Appendix Table A.6). In such cases, the categorization from the Standard site Table was primarily used, and any outliers that placed a site into another category were excluded from the final figure displaying the amplification factors according to EC8 2024 draft but were retained in the dataset.

The categorisation of the sites is depicted in the figure 4.30. Notably, the grouping of HSAFs in Category B is prominent, yet each category includes at least one site. Compared to the current EC8, additional sites have been included in Class A in the EC8 2024 draft, moreover, sites previously categorized under Class C were distributed among other categories. However, the significant clustering of HSAFs into a single category, in the current EC8 and EC8 2024 draft, raises inquiries about the adaptability and broader relevance of category definition in EC8.

The mean HSAF and amplification factors proposed by EC8 showed for categories A, E and F a relatively good convergence but not many sites are classified in these three categories. For category B, the mean HSAF appears higher amplification than the EC8 factors. For categories C and D the amplification factors and mean HSAF values show more distinct differences, however very few sites are classified in these categories as well.

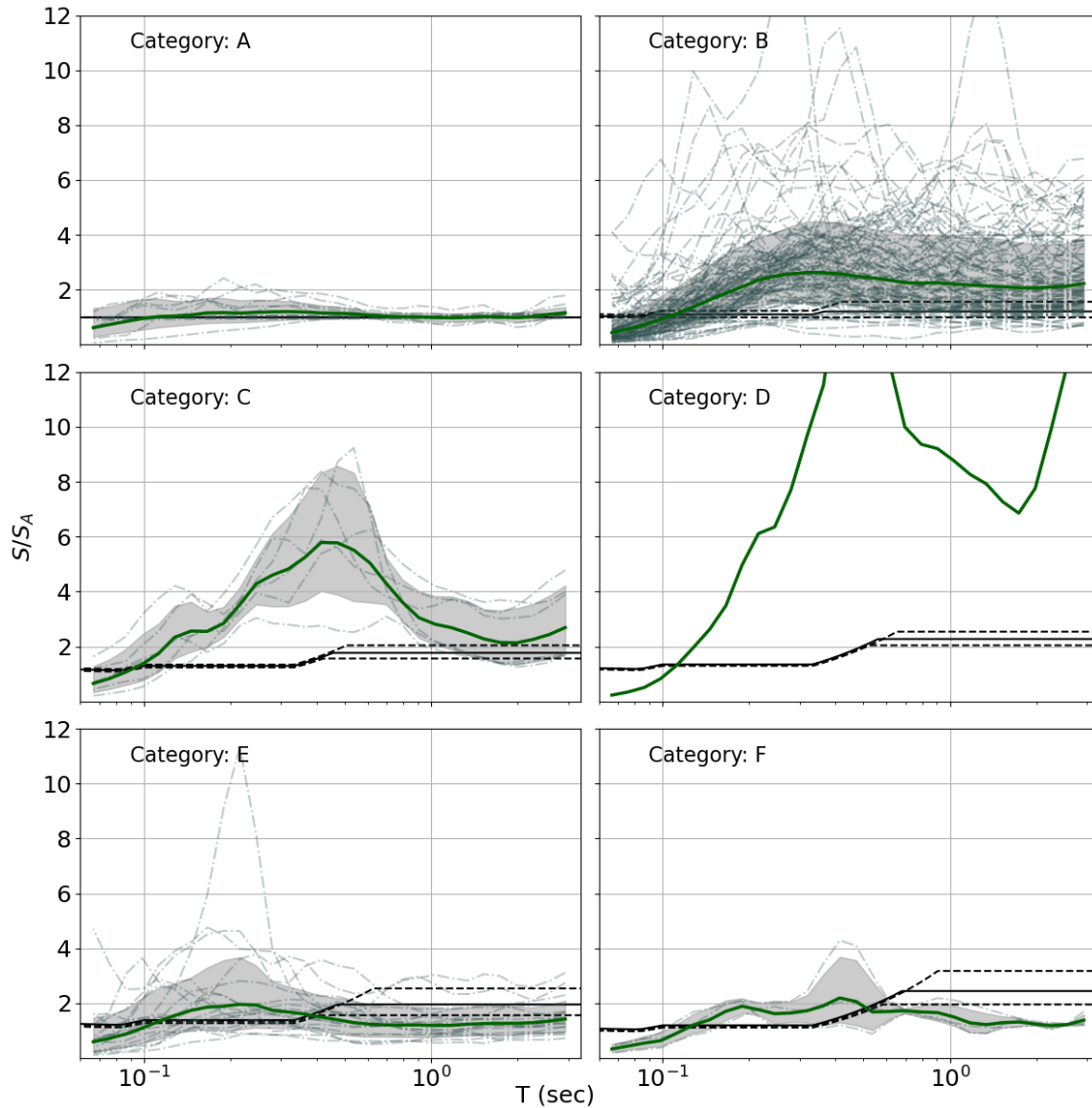


Figure 4.30: Amplification factors according to EC8 2024 draft (black lines) with a standard deviation (dashed black lines), considering high seismicity regions ($S_{\alpha,RP} = 6 \text{ m/s}^2$, $S_{\beta,RP} = 2 \text{ m/s}^2$). And the HSAF (green dashed curves) with the estimated logarithmic mean (green curve) and a $\pm std$



Chapter 5

Discussion and Conclusions

The main objective of this thesis was the estimation of the horizontal site amplification factors (HSAF s) for 152 stations scattered throughout the broader Aegean area using the generalized inversion technique (GIT). The aim was to compare these factors with the corresponding SAFs specified in the current Eurocode 8 (EC8) and 2024 draft of EC8. For this purpose, an inversion method was employed based on the diffuse field assumption (Sánchez-Sesma et al., [74]), which embodies all types of elastic waves and relates the microtremor horizontal-to-vertical spectral ratio (mHVSR) with the imaginary parts of Green's function tensor components (Sánchez-Sesma et al., [72]). As input to the inversion were used the mHVSR and the dispersion curves at six sites located on rock formations, called reference stations, to estimate 1D V_s models, albeit with some non-negligible misfits. Although the inversion code of Garcia-Jerez et al, [24], 'HV-inv', points out that the simultaneous inversion of mHVSR and dispersion curves produces smaller misfits, however in the present study higher misfits were observed. In particular, for AIG2 and VSK1 stations are the only ones that showed a misfit lower than 10, ART2, ATH5 and SIA1 stations depicted misfit values between 10 and 20, while SEIS station has the largest misfit of around 36.

Due to concerns, raised by the high misfit values observed mostly in 'SEIS' station, about the reliability of the inversion results, the 1D V_s profiles were also used, as they were obtained by Theodoulidis et al., 2024 (personal communication), using Geopsy-Dinver software, after inversion of only the dispersion curves. The results of these two approximations were used to construct the 1D theoretical Site Spectral Amplification Factors ($SAF_s^{theoretical}$) at each reference station for two cases: once with respect to seismological bedrock ($H_{3\text{km/s}}$), where V_s reaches or exceeds 3 km/s, and with respect to engineering bedrock ($H_{0.8\text{km/s}}$), where V_s reaches or exceeds 800 m/s. The $SAF_s^{theoretical}$ from the Geopsy-Dinver method showed in the case of $H_{3\text{km/s}}$ greater

smoothing at the higher frequencies than the $SAF^{theoretical}$ resulted from the 'HV-Inv'. These two cases were defined to examine if the diffuse field assumption proposed for the seismological bedrock is valid also for the engineering bedrock and because site amplification coefficients in EC8 are defined with respect to the latter one.

$SAF^{theoretical}$ were used to correct the Fourier Amplitude Spectra (FAS) of 372 earthquakes recorded at 152 stations of HUSN network from 2005 to 2018. The correction (deconvolution) of the FAS at reference stations was performed four times, for $H_{3\text{km/s}}$ and $H_{0.8\text{km/s}}$, using both 'HV-Inv' and Geopsy-Dinver approaches. Initially, the adapted FAS were imported in GIT algorithm, composing a simplistic parametric model aiming to the comparison of those two software. The obtained results showed slight differences in seismic source, attenuation path, and site properties. The adequate merging of results led to the conclusion that both methods of 1D V_s profiles acquisition, are valid despite the misfit values of estimated V_{SZ} profiles. For the final HSAF s through GIT, the deconvolved FAS obtained using the $SAF^{theoretical}$ of 'HV-inv' software were employed.

Formulating a new configured parametric model the generalized inversion was performed again for $H_{3\text{km/s}}$ and $H_{0.8\text{km/s}}$. The final results showed remarkable similarity for seismic source and attenuation path properties, while an almost constant increase in amplification of 30% was observed in site amplification factors (SAFs) across the entire frequency range when extending down to seismological bedrock. The noted deamplification for SAF down to $H_{0.8\text{km/s}}$ in the site parameter outcome, may be, partially, attributed to the computed geometrical spreading parameter, γ , being slightly lower when the inversion was conducted for $H_{0.8\text{km/s}}$. Moreover, the deamplification may also be attributed to the $SAF^{theoretical}$ ratios of $H_{3\text{km/s}}$ over $H_{0.8\text{km/s}}$, derived from the V_{SZ} profiles at six reference stations, which also depicted a steady difference close to 30%.

Based on estimated VSAF, the $V_b H_b R$ has been calculated, which is the inverse of the horizontal-to-vertical spectra ratio (eHVSF), used to convert the amplitude of horizontal incident S-waves into vertical P-waves in bedrock. Kawase et al. [41] and Ito et al. [33] who used a large data set in Japan area, calculated a theoretical value for $V_b H_b R$ approximately at 0.76, in the case of a Poisson solid. In the present study, $V_b H_b R$ was calculated separately at each reference station for $H_{0.8\text{km/s}}$ and $H_{3\text{km/s}}$. With respect to engineering bedrock, $V_b H_b R$ was ranged from 0.52 at 'AIG2' station to 0.84 at 'SEIS' station, while with respect to seismological bedrock, $V_b H_b R$ was ranged from 0.58 at 'AIG2' station to 0.79 at 'SEIS' station.

The GIT derived HSAF s for $H_{3\text{km/s}}$ were used to estimate the Vertical Amplification Correction Functions (VACFs) proposed by Ito et al., [33]. This study ([33]) calculated the log-average VACF for 1678 sites in Japan and the results were compared with log-average VACF obtained in the present thesis. The comparison showed differences both at low and high frequencies. Specifically, the log-averaged

VACF calculated for 152 stations across Greece exhibited amplification within the frequency range between 0.7 Hz to 7 Hz, similar to the values calculated by [33], while for frequencies lower than 0.7 Hz, higher values were observed, where the amplification exceeded 1.0. This phenomenon can be, partly, attributed to the initial FAS data and the method of selecting the S-wave windows. To compile the FAS catalogue properly, S-wave windows of 5 seconds were selected in the waveforms of the studied earthquakes, regarding of their epicentral distance ($12 < R_{rjb} < 300$ km) and its magnitude ($4 < M_w < 6$). Grendas et al., [28], performed a parametric experimental analysis on the most appropriate selection of S-wave windows, and observed that longer S-wave windows result in lower standard deviations, especially at lower frequencies. On the contrary, at frequencies higher than 7 Hz, a steep reduction in VACF values is observed, which could be linked to the Soil Structure Interaction (SSI) of buildings housing the accelerometer sensors. Kawase et al., [41] proposed the earthquake-to-microtremor ratio (EMR), from which the eHVSr can be empirically calculated from the mHVSr. The EMR calculated in this study showed an average value of about 1.1 for frequencies from 1 to 10 Hz. This calculation of EMR could be used for a double correction of eHVSr data, along with VACF.

The final HSAF s for $H_{0.8\text{km/s}}$ were used to categorize the sites by soil category according to the current EC8 and the 2024 draft EC8 and compare them with the default site amplification factors defined therein. Categorisation according to the current EC8 resulted in only the six reference stations being classified as category A, while the remaining 146 stations were divided into 107 site in categories B and 39 in category C. According to the 2024 draft EC8, more stations were included in category A, and at least one station was classified into other categories (B-F). However, pronounced clustering of amplification factors in category B was observed, prompting questions regarding the flexibility and broader applicability of how categories are defined. Also, for category A in both EC8 the amplification factors proposed and the mean HSAF calculated in each category show satisfactory convergence, while for category B the mean HSAF s appear slightly higher amplification than the ones proposed by the two EC8 amplification factors. For category C of the current EC8, mean HSAF is higher than the EC8's amplification factors. In categories C, D, E and F of the 2024 draft EC8, the positions classified in them are few. In the first two categories there is a large difference between the proposed amplification factors and the calculated average HSAF s, while in the last two they show good correlation. The conclusion of this study highlighted the key findings and their immediate implications, however, to fully understand the broader significance and future direction of this outcome a more detailed discussion is required.

The 1D V_{SZ} profiles obtained by the 'HV-inv' algorithm, despite noticeable misfit, suggest that the final results are reliable. However, further investigation into the causes of these errors and potential improvement in inversion techniques are warranted to enhance the reliability of the results. The subsequent $SAF^{theoretical}$ constructed for

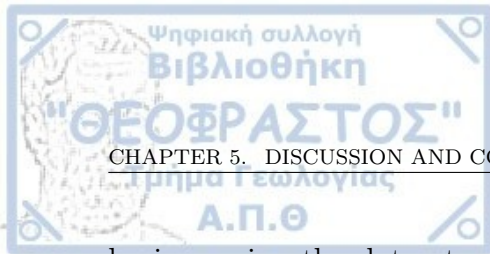


$H_{3\text{km/s}}$ indicates a significant influence of the underlying bedrock properties on site amplification since there is a consistent increase in amplification at the highest frequencies, while for engineering bedrock, deamplification appears, suggesting that the computed geometrical spreading parameter and $SAF^{theoretical}$ ratios require careful consideration in future studies.

The categorization of the 152 stations according to current EC8 and 2024 draft EC8, and the pronounced clustering in category B, raises questions about the flexibility and broader applicability of the categorisation criteria. Current EC8 categorises sites based solely on the average velocity of S-waves in the first 30 meters, V_{S30} , highlighting the need for more soil types based on additional parameters. Although 2024 draft EC8 defines more parameters for categorization beyond V_{S30} the grouping into a single category remains. The comparison with proposed amplification factors in EC8 underscores the necessity for several adjustments in EC8 theoretical conditions and take into account the local geological and seismological conditions. Furthermore, the increase in sites of interest will lead to a better distribution of them in the rest of the proposed categories.

The differences between the log-average VACF for greek and japanese data, with the former showing inconsistent values at low and high frequencies, emphasise the need for further investigation into the way of selection of S-wave windows and the impact of Soil Structure Interaction (SSI) on recordings. These factors must be carefully considered in future VACFs calculations, and a new, improved version of the FAS catalogue would, probably, ensure accurate site amplification assessments. Furthermore, the disparity of data between the two studies is distinct. Additionally, the calculation of the log-averaged $V_b H_b R$ at each reference station revealed a range from 0.52 to 0.84 with respect to the seismological bedrock and from 0.58 to 0.79 with respect to the engineering bedrock. The 152 stations studied in the present dissertation, are limited to achieve satisfactory results in the calculation of VACFs and $V_b H_b R$. This suggests that increasing the number of data and the number of stations homogeneously distributed over site classes according to EC8, is necessary to improve the accuracy of above calculations.

The results of this study might have significant contribution also to seismic hazard assessment. The scientific community has validated the importance of conducting studies with respect to seismological bedrock, such as the diffuse field assumption (DFA) theory which has been proven valid in these context. This study attempted to extend the DFA theory down to engineering bedrock to investigate the differences and similarities between the two cases ($H_{0.8\text{km/s}}$ and $H_{3\text{km/s}}$). The noticeable deamplification observed at $H_{0.8\text{km/s}}$ in $SAF^{theoretical}$ and GIT's empirical SAFs was anticipated. However, many aspects, such as seismic source and anelastic attenuation factors, showed congruity between the two cases of seismological and engineering bedrock. The potential for greater similarities between the two approaches could be enhanced



by increasing the dataset samples, the number of stations and the characterisation of reference stations by incorporating more flexible and regionally tailored criteria. Also, the broad range of $V_b H_b R$ factor for $H_{0.8 \text{ km/s}}$ and $H_{3 \text{ km/second}}$ fortifies the need for more defined reference stations to validate $V_b H_b R$ estimations

Overall, several prospective for future research have been identified. Firstly, proving that several inversion techniques can yield satisfactory 1D V_{SZ} profiles, but improving these techniques to reduce misfits and increase reliability could be crucial. Secondly, a comprehensive analysis of the impact of SSI on recordings and their contribution to recording ambient noise is necessary. Further analysis is also needed for constructing the FAS catalogues, particularly regarding the choice of S-wave windows, the number of recordings for each seismic event, and the total number of data. Finally, further studies should explore the regional applicability of EC8 soil categorization criteria and investigate potential adjustments.



References

- [1] Cen (2004). Eurocode 8: Design of structures for earthquake resistance—part 1: general rules, seismic actions and rules for buildings. *European Committee for Standardization, Brussels*.
- [2] Geopsy. <https://www.geopsy.org>.
- [3] K. Aki. Space and time spectra of stationary stochastic waves, with special reference to microtremors. *Earthquake Research Institute, XXXV*, June 1957.
- [4] K. Aki. Local site effects on strong ground motion. *Earthquake Engineering and Soil Dynamics II—Recent Advances in Ground Motion Evaluation, ASCE, Reston, Virginia*, page 103–155, 1988.
- [5] D.J. Andrews. Objective determination of source parameters and similarity of earthquakes of different size. *Earthquake Source Mechanics*, 37:259 – 267, 1986. <https://doi.org/10.1029/GM037p0259>.
- [6] P.I. Apostolidis, D.G. Raptakis, K.K. Pandi, M.V. Manakou, and K.D. Pitilakis. Definition of subsoil structure and preliminary ground response in aigion city (Greece) using microtremor and earthquakes. *Soil Dynamics and Earthquake Engineering*, 26:922–940, 2006. <https://doi.org/10.1016/j.soildyn.2006.02.001>.
- [7] H. Arai and K. Tokimatsu. S-wave velocity profiling by inversion of microtremor h/v spectrum. *Bulletin of the Seismological Society of America*, 94:53–63, 2004. <https://doi.org/10.1785/0120030028>.
- [8] M. W. Asten and J. D. Henstridge. S-wave velocity profiling by inversion of microtremor h/v spectrum. *Bulletin of the Seismological Society of America*, 49(11):53–63, 1984. <https://doi.org/10.1190/1.1441596>.
- [9] D.M. Boore. Determining generic velocity and density models for crustal amplification calculations, with an update of the Boore and Joyner, (1997)[11] generic site amplification for $\bar{V}_S(Z) = 760\text{m/s}$. *Bulletin of the Seismological Society of America*, 106(1):316–320, 2016. <https://doi.org/10.1785/0120150229>.

- REFERENCES
-
- [10] D.M. Boore and J. Boatwright. Average body-wave radiation coefficients. *Bulletin of the Seismological Society of America*, 74(5):1615–1621, 1984. <https://doi.org/10.1785/BSSA0740051615>.
- [11] D.M. Boore and W.B. Joyner. Site amplifications for generic rock sites. *Bulletin of the Seismological Society of America*, 87:327–341, 1997. <https://doi.org/10.1785/BSSA0870020327>.
- [12] D.M. Boore, J.P. Stewart, A.A. Skarlatoudis, E. Seyhan, B. Margaris, N. Theodoulidis, E. Scordilis, I. Kalogeras, N. Klimis, and N.S. Melis. A ground-motion prediction model for shallow crustal earthquakes in greece. *Bulletin of the Seismological Society of America.*, 111(2):857–874, 2021. <https://doi.org/10.1785/0120200270>.
- [13] R. D. Borcherdt. Effects of local geology on ground motion near san francisco bay. *Bulletin of the Seismological Society of America.*, 60(1):29–61, 1970. <https://doi.org/10.1785/BSSA0600010029>.
- [14] T.M. Brocher. Empirical relations between elastic wavespeeds and density in the earth’s crust. 95(6):2081–2092, 2005. <https://doi.org/10.1785/0120050077>.
- [15] T.M. Brocher. Compressional and shear-wave velocity versus depth relations for common rock types in northern california. 98(2):950–968, 2008. <https://doi.org/10.1785/0120060403>.
- [16] J.N. Brune. Correction [to “tectonic stress and the spectra of seismic shear waves from earthquakes”]. *Journal of Geophysical Research*, 20::5002, 1971. <http://dx.doi.org/10.1029/JB076i020p05002>.
- [17] J.N. Brune. Tectonic stress and the spectra of seismic shear waves from earthquakes. *Journal of Geophysical Research*, 75(26):4901–5141, 1971. <https://doi.org/10.1029/JB075i026p04997>.
- [18] J. Capon. High-resolution frequency-wavenumber spectrum analysis. *Proceedings of the IEEE*, 57(8):1408 – 1418, August 1969. <https://doi.org/10.1109/PROC.1969.7278>.
- [19] S. Castellaro, F. Mulargia, and P.L. Rossi. v_{s30} : Proxy for seismic amplification? *Seismological Research Letters*, 79(4):540–543, 2008. <https://doi.org/10.1785/gssrl.79.4.540>.
- [20] R.R. Castro, J.G. Anderson, and S.K. Singh. Site response, attenuation and source spectra of s waves along the guerrero, mexico, subduction zone. *Bulletin of the Seismological Society of America*, 80(6A):1481–1503, 1990. <https://doi.org/10.1785/BSSA08006A1481>.

- [21] P. Dang, J. Cui, H. Yang, and J. Song. Regional spectral characteristics, quality factor and site responses in western-central Sichuan, China (I): Application of parametric generalized inversion technique. *Soil Dynamics and Earthquake Engineering*, 176:108303, 2024. <https://doi.org/10.1016/j.soildyn.2023.108303>.
- [22] S. Drouet, S. Chevrot, F. Cotton, and A. Souriau. Simultaneous inversion of source spectra, attenuation parameters, and site responses: Application to the data of the french accelerometric network. *Bulletin of the Seismological Society of America*, 98(1):198–219, 2008. <https://doi.org/10.1785/0120060215>.
- [23] M. R. Gallipoli and M. Mucciarelli. Comparison of site classification from v_{S30} , v_{S10} , and HVSR in italy. *Bulletin of the Seismological Society of America*, 99(1):340–351, 2009. <https://doi.org/10.1785/0120080083>.
- [24] A. García-Jerez, J. Piña-Flores, F.J. Sánchez-Sesma, F. Luzón, and M. Petron. A computer code for forward calculation and inversion of the H/V spectral ratio under the diffuse field assumption. *Computers and Geosciences*, 97:67–78, 2016. <https://doi.org/https://doi.org/10.1016/j.cageo.2016.06.016>.
- [25] A. García-Jerez, H. Seivane, M. Navarro, M. Martínez-Segura, and J. Piña-Flores. Joint analysis of rayleigh-wave dispersion curves and diffuse-field hvsr for site characterization: The case of el ejido town (se spain). *Soil Dynamics and Earthquake Engineering*, 121:102–120, 2019. <https://doi.org/10.1016/j.soildyn.2019.02.023>.
- [26] R. Graves and A. Pitiraka. Broadband time history simulation using a hybrid approach. In *13th World Conference on Earthquake Engineering*, Vancouver, B.C., Canada, August 1-6 2004. Paper No. 1098.
- [27] I. Grendas, N. Theodoulidis, P. Hatzidimitriou, B. Margaris, and S. Drouet. Determination of source, path and site parameters based on non-linear inversion of accelerometric data in greece. *Bulletin of the Seismological Society of America*, 16:5061–5094, April 2018. <https://doi.org/10.1007/s10518-018-0379-8>.
- [28] I. Grendas, N. Theodoulidis, F. Hollender, and P. Hatzidimitriou. Effects of the s-wave time-window selection on standard spectral ratio (ssr): Application to the argonet vertical array in greece. *6th International Conference on Earthquake Engineering and Seismology, 13-15 October, GTU, Gebze, Kocaeli, Turkey*, 2021.
- [29] I. Grendas, N. Theodoulidis, F. Hollender, and P. Hatzidimitriou. A GIT algorithm for simultaneous estimation of seismic source, site response and regional-distance dependent attenuation parameters: application to synthetic and real data. *Journal of Seismology*, 25:575–598, 2021. <https://doi.org/10.1007/s10950-020-09975-8>.

- [30] I. Grendas, N. Theodoulidis, F. Hollender, and P. Hatzidimitriou. Spectral decomposition of S-waves in investigating regional dependent attenuation and improving site amplification factors: A case study in western Greece. *Bulletin of Earthquake Engineering*, 20(12):6441–6465, September 2022. <https://doi.org/10.1007/s10950-020-09975-8>.
- [31] T.C. Hanks and H. Kanamori. A moment magnitude scale. *Journal of Geophysical Research*, 84(B5):2145–2400, 1979. <https://doi.org/10.1029/JB084iB05p02348>.
- [32] W.K. Hastings. Monte carlo sampling methods using markov chains and their applications. *Biometrika*, 57(1):97–109, 1970. <https://doi.org/10.1093/biomet/57.1.97>.
- [33] E. Ito, K. Nakano, F. Nagashima, and H. Kawase. A method to directly estimate s-wave site amplification factor from horizontal-to-vertical spectral ratio of earthquakes (ehvsrs). *Bulletin of the Seismological Society of America*, 110(6):2892–2911, 2020. <https://doi.org/10.1785/0120190315>.
- [34] T. Iwata and K. Irikura. Source parameters of the 1983 japan sea earthquake sequence. *Journal of Physics of Earth*, 36(4):155–184, 1988. <https://doi.org/10.4294/jpe1952.36.155>.
- [35] S. Jeong, B. W. Stump, and H. R. DeShon. Spectral characteristics of ground motion from induced earthquakes in the fort worth basin, texas, using the generalized inversion technique . *Bulletin of the Seismological Society of America*, 110(5):2058–2076, 2020. <https://doi.org/10.1785/0120200097>.
- [36] K. Kato, M. Takemura, T. Ikeura, K. Urao, and T. Uetake. Preliminary analysis for evaluation of local site effects from strong motion spectra by an inversion method. *Journal of Physics of Earth*, 40(1):175–191, 1992. <https://doi.org/10.4294/jpe1952.40.175>.
- [37] H. Kawase. Site effects on strong ground motions. *International Handbook of Earthquake and Engineering Seismology, Part B*, W Lee, H. Kanamori, P. Jennings, and C. Kisslinger (Editors), Academic Press, London, United Kingdom, page 1013–1030, 2003.
- [38] H. Kawase. Site effects derived from spectral inversion method for k-net, kik-net, and jma strong-motion network with special reference to soil nonlinearity in high pga records. *Bulletin of the Seismological Society of America*, 81:309–315, 2006. <http://id.ndl.go.jp/bib/8865881>.
- [39] H. Kawase, J. Francisco, F.J. Sánchez-Sesma, and S. Matsushima. The optimal use of horizontal-to-vertical spectral ratios of earthquake motions for velocity inversions based on diffuse-field theory for plane waves. *Bulletin of the*

- Seismological Society of America*, 101(5):2001–2014, October 2011. <https://doi.org/10.1785/0120100263>.
- [40] H. Kawase and H. Matsuo. Amplification characteristics of k-net, kik-net, and jma shindokei network sites based on the spectral inversion technique. *3th World Conference on Earthquake Engineering Vancouver, B.C., Canada*, Paper No. 454, August 1-6 2004.
- [41] H. Kawase, Y. Mori, and F. Nagashima. Difference of horizontal-to-vertical spectral ratios of observed earthquakes and microtremors and its application to s-wave velocity inversion based on the diffuse field concept. *Earth, Planets and Space*, 70(1), 2018. <https://doi.org/10.1186/s40623-017-0766-4>.
- [42] H. Kawase, F. Nagashima, K. Nakano, and Y. Mori. Direct evaluation of s-wave amplification factors from microtremor H/V ratios: Double empirical corrections to “nakamura” method. *Soil Dynamics and Earthquake Engineering*, 126, 2018. <https://doi.org/10.1016/j.soildyn.2018.01.049>.
- [43] S. Kirkpatrick, D. Gelatt, and M. Vecchi. Optimization by simulated annealing. *Science (New York, N.Y.)*, 220:671–680, 1983. <https://doi.org/10.1126/science.220.4598.671>.
- [44] P. Klin, G. Laurenzano, and E. Priolo. Gitanes: A matlab package for estimation of site spectral amplification with the generalized inversion technique. *Seismological Research Letters*, 89(1):182–190, 2018. <https://doi.org/10.1785/0220170080>.
- [45] K. Konno and T. Ohmachi. Ground-motion characteristics estimated from spectral ratio between horizontal and vertical components of microtremor. *Bulletin of the Seismological Society of America*, 88(1):228–241, February 1998. <https://doi.org/10.1785/BSSA0880010228>.
- [46] S. R. Kotha, D. Bindi, and F. Cotton. Partially non-ergodic region specific gmpe for europe and middle-east. *Bulletin of the Seismological Society of America*, 14:1245–1263, 2016. <https://doi.org/10.1007/s10518-016-9875-x>.
- [47] V. W. Lee and M. D. Trifunac. Should average shear-wave velocity in the top 30 m of soil be used to describe seismic amplification? *Soil Dynamics and Earthquake Engineering*, 30(11):1250–1258, 2010. <https://doi:10.1016/j.soildyn.2010.05.007>.
- [48] Y.S. Lee, E. Graham, G. Jackson, A. Galindo, and C.S. Adjiman. A comparison of the performance of multi-objective optimization methodologies for solvent design. *Computer Aided Chemical Engineering*, 46:37–42, 2019. <https://doi.org/10.1016/B978-0-12-818634-3.50007-2>.

- [49] I. Maragkakis. Site Amplification Factors in stations of the National Network of Accelerometers in Greece. *Master Thesis, School of Geology, Aristotle University of Thessaloniki*, page 130pp, 2022.
- [50] F. Nagashima, H. Kawase, and S. Matsushima. Estimation of horizontal seismic bedrock motion from vertical surface motion based on horizontal-to-vertical spectral ratios of earthquake motions. *16th World Conference on Earthquake, 16WCEE 2017 Santiago Chile, January 9th to 13th, Paper No 3685*, 2017. Registration Code: S-N1463127272.
- [51] F. Nagashima, S. Matsushima, H. Kawase, F. J. Sánchez-Sesma, T. Hayakawa, T. Satoh, and M. Oshima. Application of horizontal-to-vertical spectral ratios of earthquake ground motions to identify subsurface structures at and around the k-net site in tohoku, japan. *Bulletin of the Seismological Society of America*, 104(5):2288–2302, 2014. <https://doi.org/10.1785/0120130219>.
- [52] Y. Nakamura. A method for dynamic characteristics estimation of subsurface using microtremor on the ground surface. *Quarterly Report of Railway Technical Research Institute*, 30:25–33, 1989.
- [53] Y. Nakamura. Real-time information systems for hazards mitigation. *Proceedings of the 11th World Conference on Earthquake Engineering (Acapulco, Mexico)*., 1996.
- [54] Y. Nakamura. Vulnerability indexes for surface ground and structures using microtremor. *8th Soil Dynamics Earthquake Engineering '97*, 30:25–33, 20 -24 July 1997.
- [55] Y. Nakamura. Clear identification of fundamental idea of nakamura's technique and its applications. *Proceedings of the 12th World Conference on Earthquake Engineering (Auckland, New Zealand)*., (8p), 2000.
- [56] Y. Nakamura. A modified estimation method for amplification factor of ground and structures using the H/V spectral ratio. *Proc. Of the 2nd Workshop on Dynamic Interaction of Soil and Structure '12, L'Aquila, Italy*, pages 273–284, 29-30 March 2014.
- [57] Y. Nakamura. What is the nakamura method? *Seismological Research Letters*, 90(4):1437– 1443, 2019. <https://doi.org/10.1785/0220180376>.
- [58] K. Nakano, S. Matsushima, and H. Kawase. Statistical properties of strong ground motions from the generalized spectral inversion of data observed by k-net, kik-net, and the jma shindokei network in japan. *Bulletin of the Seismological Society of America*, 105(5):2662–2680, 2015. <https://doi.org/10.1785/0120140349>.

- [59] J.A. Nelder and R. Mead. Simplex method for function minimization. *The Computer Journal*, 7(4):308–313, 1965. <https://doi.org/10.1093/comjnl/7.4.308>.
- [60] M. Nogoshi and T. Igarashi. On the propagation characteristics of microtremor. *Zisin*, 23:264–280, 1970a. (in Japanese with English abstract).
- [61] M. Nogoshi and T. Igarashi. On the amplitude characteristics of microtremor—part 1. *Zisin*, 23:281–303, 1970b. (in Japanese with English abstract).
- [62] M. Nogoshi and T. Igarashi. On the amplitude characteristics of microtremor—part 2. *Zisin*, 24:26–40, 1971. (in Japanese with English abstract).
- [63] M. Ohori, A. Nobata, and K. Wakamatsu. A comparison of esac and fk methods of estimating phase velocity using arbitrarily shaped microtremor arrays. *Bulletin of the Seismological Society of America*, 92(6):2323–2332, August 2002. <https://doi.org/10.1785/0119980109>.
- [64] R. Paolucci, M. Aimar, A. Ciancimino, M. Dotti, S. Foti, G. Lanzano, P. Mattevi, F. Pacor, and M. Vanini. Checking the site categorization criteria and amplification factors of the 2021 draft of eurocode 8 part 1–1. *Bulletin of Earthquake Engineering*, 19:4199–4234, 2021. <https://doi.org/10.1007/s10518-021-01118-9>.
- [65] C.B. Park, R.D. Miller, J. Xia, J.A. Hunter, and J.B. Harris. Higher mode observation by the masw method. *SEG Technical Program Expanded Abstracts · January 1999*, 1999. <https://doi.org/10.1190/1.1821070>.
- [66] M. Petron, F.J. Sánchez-Sesma, A. Rodríguez-Castellanos, M. Campillo, and R.L. Weaver. Two perspectives on equipartition in diffuse elastic fields in three dimensions. *The Journal of the Acoustical Society of America*, 126:1125–1130, 2009. <https://doi.org/10.1121/1.3177262>.
- [67] J. Piña-Flores, M. Cárdenas-Soto, A. García-Jerez, M. Campillo, and F.J. Sánchez-Sesma. The search of diffusive properties in ambient seismic noise. *Bulletin of the Seismological Society of America*, 111(3):1650–1660, 2021. <https://doi.org/10.1785/0120200189>.
- [68] D. Raptakis, N. Theodulidis, and K. Pitilakis. Data analysis of the Euroseistest strong motion array in Volvi (Greece): standard and horizontal-to-vertical spectral ratio techniques. *Earthquake Spectra*, 14(1):203–224, 1998. <https://doi:10.1785/0120130030>.

- [69] J. Roberts, M. Asten, H.H. Tsang, S. Venkatesan, and N. Lam. Shear wave velocity profiling in melbourne silurian mudstone using the spac method. *AEES Conference at Mount Gambier.*, November 2004.
- [70] A. Rodriguez-Marek, F. Cotton, N. A. Abrahamson, S. Akkar, L. A. Atik, B. Edwards, G. A. Montalva, and H. M. Dawood. A model for single-station standard deviation using data from various tectonic regions. *Bulletin of the Seismological Society of America*, 103(6):3149–3163, 2013. <https://doi.org/10.1785/0120130030>.
- [71] F.J. Sánchez-Sesma, J.A. Pérez-Ruiz, F. Luzon, M. Campillo, and A. Rodríguez-Castellanos. Diffuse fields in dynamic elasticity. *Wave Motion*, 45(5):641–654, 2008. <https://doi.org/10.1016/j.wavemoti.2007.07.005>.
- [72] F.J. Sánchez-Sesma, M. Rodríguez, U. Iturraran-Viveros, A. Rodríguez-Castellanos, M. Suarez, M.A. Santoyo, A. Garcia-Jerez, and F. Luzon. Site effects assessment using seismic noise. in *Proceedings of the 9th International Workshop on Seismic Microzoning and Risk Reduction*, February 21 -24 2010. Cuernavaca, Mexico.
- [73] F.J. Sánchez-Sesma, M. Rodríguez, U. Iturrarán Viveros, F. Luzon, M. Campillo, M. Ludovic, A. Garcia-Jerez, M. Suarez, M.A. Santoyo, and A. Rodríguez Castellanos. A theory for microtremor H/V spectral ratio: application for a layered medium. *Geophysical Journal International*, 186(1):221–225, 2011. <https://doi.org/10.1111/j.1365-246X.2011.05064.x>.
- [74] F.J. Sánchez-Sesma, R.L. Waver, H. Kawase, S. Matsushima, F. Luzon, and M. Campillo. Energy partitions among elastic waves for dynamic surface loads in a semi-infinite solid. *Bulletin of the Seismological Society of America*, 101(4):1704–1709, 2011. <https://doi.org/10.1785/0120100196>.
- [75] T. Satoh, H. Kawase, , and T. Sato. Statistical spectral model of earthquakes in the eastern tohoku district, japan, based on the surface and borehole records observed in sendai. *Bulletin of the Seismological Society of America*, 87(2):446–462, 1997. <https://doi.org/10.1785/BSSA0870020446>.
- [76] SESAME European research project. Guidelines for the implementation of the h/v spectral ratio technique on ambient vibrations measurements, processing and interpretation. WP12 – Deliverable D23.12, 2004. https://sesame.geopsy.org/Delivrables/Del-D23-HV_User_Guidelines.pdf.
- [77] H. Shible, F. Hollender, D. Bindi, P. Traversa, A. Oth, B. Edwards, P. Klin, H. Kawase, I. Grendas, R. R. Castro, N. Theodoulidis, and P. Gueguen. Gitec: A generalized inversion technique benchmark. *Bulletin of the Seismological Society of America*, 112(2):850–877, 2022. <https://doi.org/10.1785/0120210242>.

- [78] J.H. Steidl, G.T. Alexei, and R.F. Archuleta. What is a reference site?. *Bulletin of the Seismological Society of America*, 86(6):1733–1748, 1996. <https://doi.org/10.1785/BSSA0860061733>.
- [79] J. P. Stewart, N. Klimis, A. Savvaidis, N. Theodoulidis, E. Zargli, G. Athanopoulos, P. Pelekis, G. Mylonakis, and B. Margaritis. Compilation of a local v_{S30} profile database and its application for inference of v_{S30} from geologic- and terrain-based proxies. *Bulletin of the Seismological Society of America.*, 104(6):2827–2841, 2014. <https://doi.org/10.1785/0120130331>.
- [80] R. Takahashi and K. Hirano. Seismic vibrations of soft grounds. *Bulletin of Earthquake Research Institute Tokyo University*, 19(3):534–543, 1941. in Japanese with English abstract.
- [81] Y. Tao and E. Rathje. Taxonomy for evaluating the site-specific applicability of one-dimensional ground response analysis. *Soil Dynamics and Earthquake Engineering*, 128:10,5865, 2020. <https://doi.org/10.1016/j.soildyn.2019.105865>.
- [82] A. Tarantola. Inverse problem theory and methods for model parameter estimation. *Society for Industrial and Applied Mathematics.*, 2005.
- [83] N. Theodoulidis, F. Hollender, P. Rischette, M. Buscetti, I. DousteBacque, I. Grendas, and Z. Roumelioti. Characterization of selected “rock” reference stations of the Hellenic Accelerometer Network (HAN). *to be submitted for publication.*, 2024.
- [84] N. Theodoulidis, I. Maragkakis, I. Grendas, P. Hatzidimitriou, H. Kawase, E. Ito, and P. Triantafyllidis. Estimation of s-wave horizontal spectral amplification factor (HSAF) from earthquake horizontal-to-vertical spectral ratio (eHVSR) in Greece. *3rd European Conference on Earthquake Engineering Seismology, Bucharest, Romania*, 2022.
- [85] F. Vats and D. Basu. On the construction of joyner-boore distance (R_{jb}) for PESMOS and COSMOS databases. *Journal of Seismology*, 27::173–202, 2014. <https://doi.org/10.1007/s10950-022-10129-1>.
- [86] R.A. Waltz, J.L. Morales, J. Nocedal, and D. Orban. An interior algorithm for nonlinear optimization that combines line search and trust region steps. *Mathematical Programming*, 107(3):391–408, 2006. <https://doi.org/10.1007/s10107-004-0560-5>.
- [87] M. Wathelet, B. Guillier, P. Roux, C. Cornou, and M. Ohrnberger. Rayleigh wave three-component beamforming: signed ellipticity assessment from high-resolution frequency-wavenumber processing of ambient vibration arrays. *Geo-*



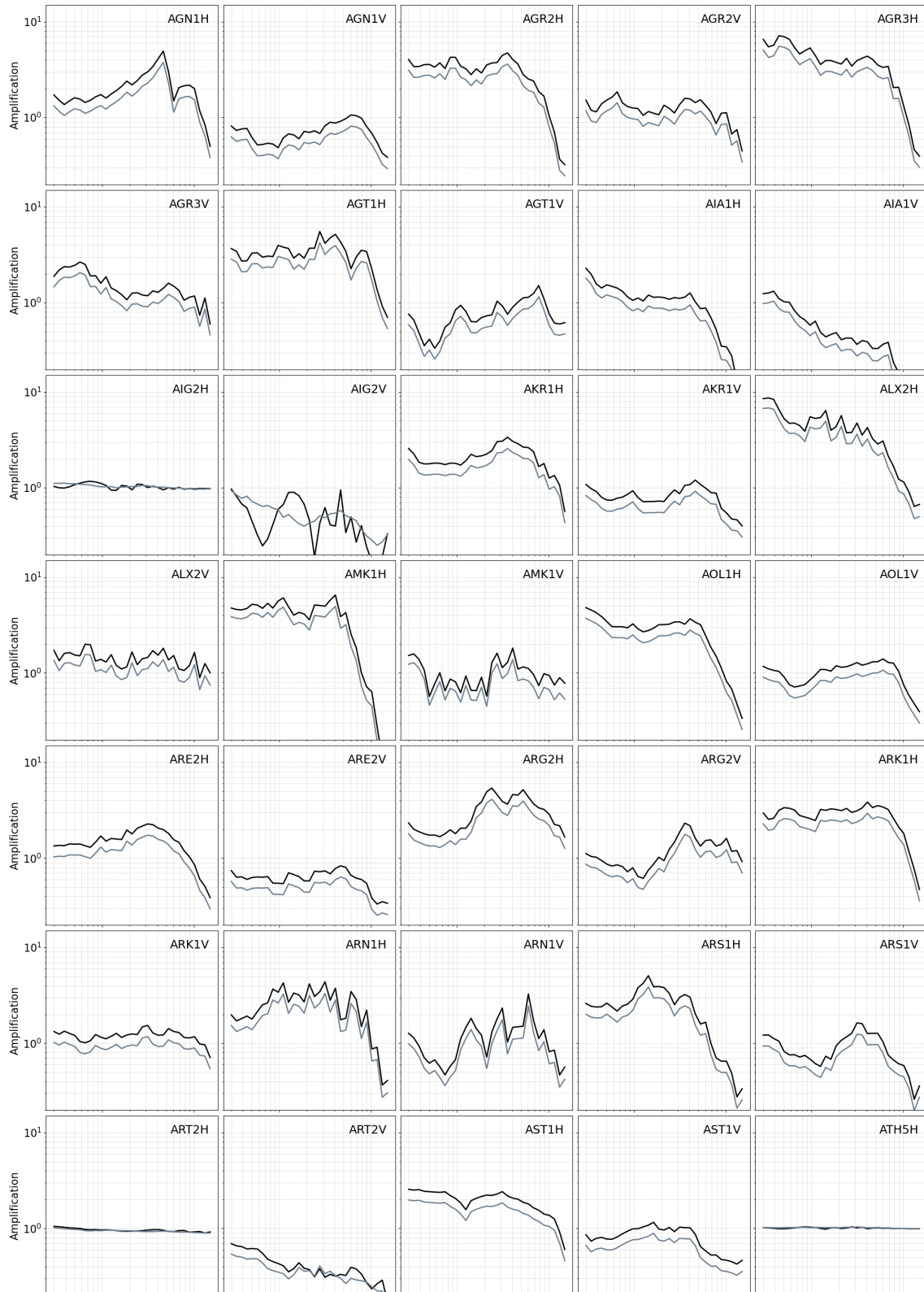
physical Journal International, 215(1):507–523, October 2018. <https://doi.org/10.1007/s10107-004-0560-5>.



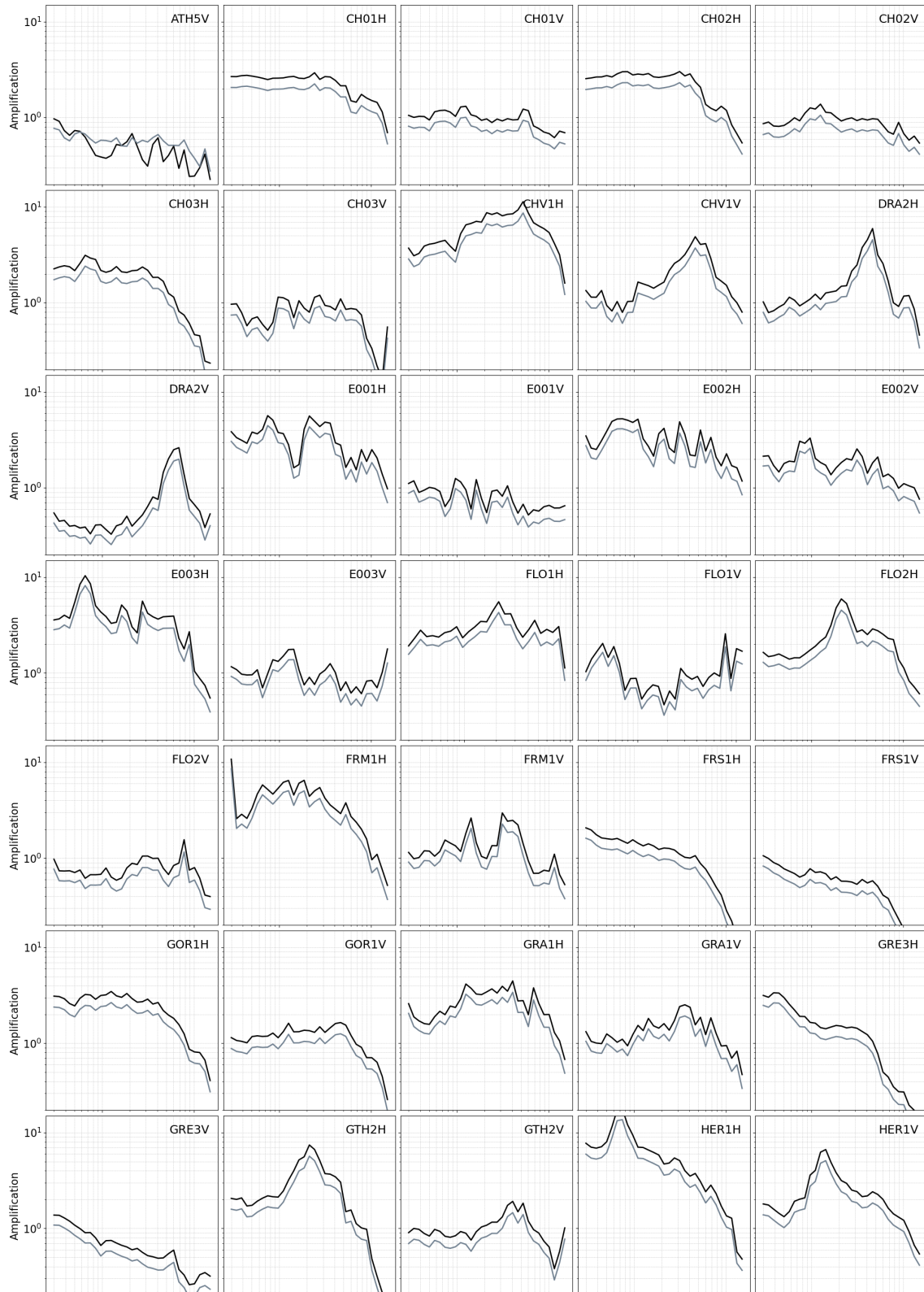
Appendix A

Site Amplification Factors (SAFs) for the 152 stations

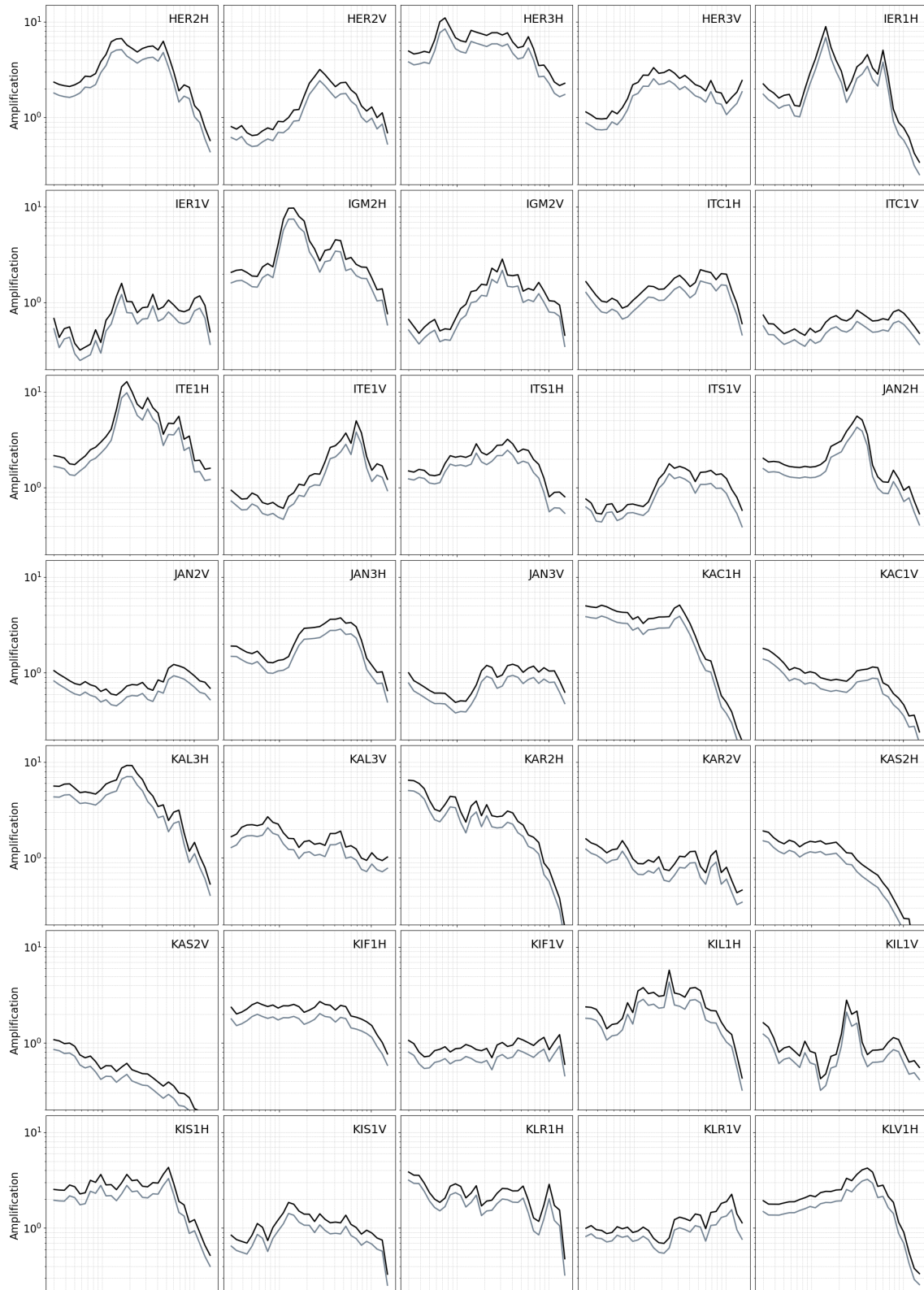
APPENDIX A. SITE AMPLIFICATION FACTORS (SAFS) FOR THE 152 STATIONS



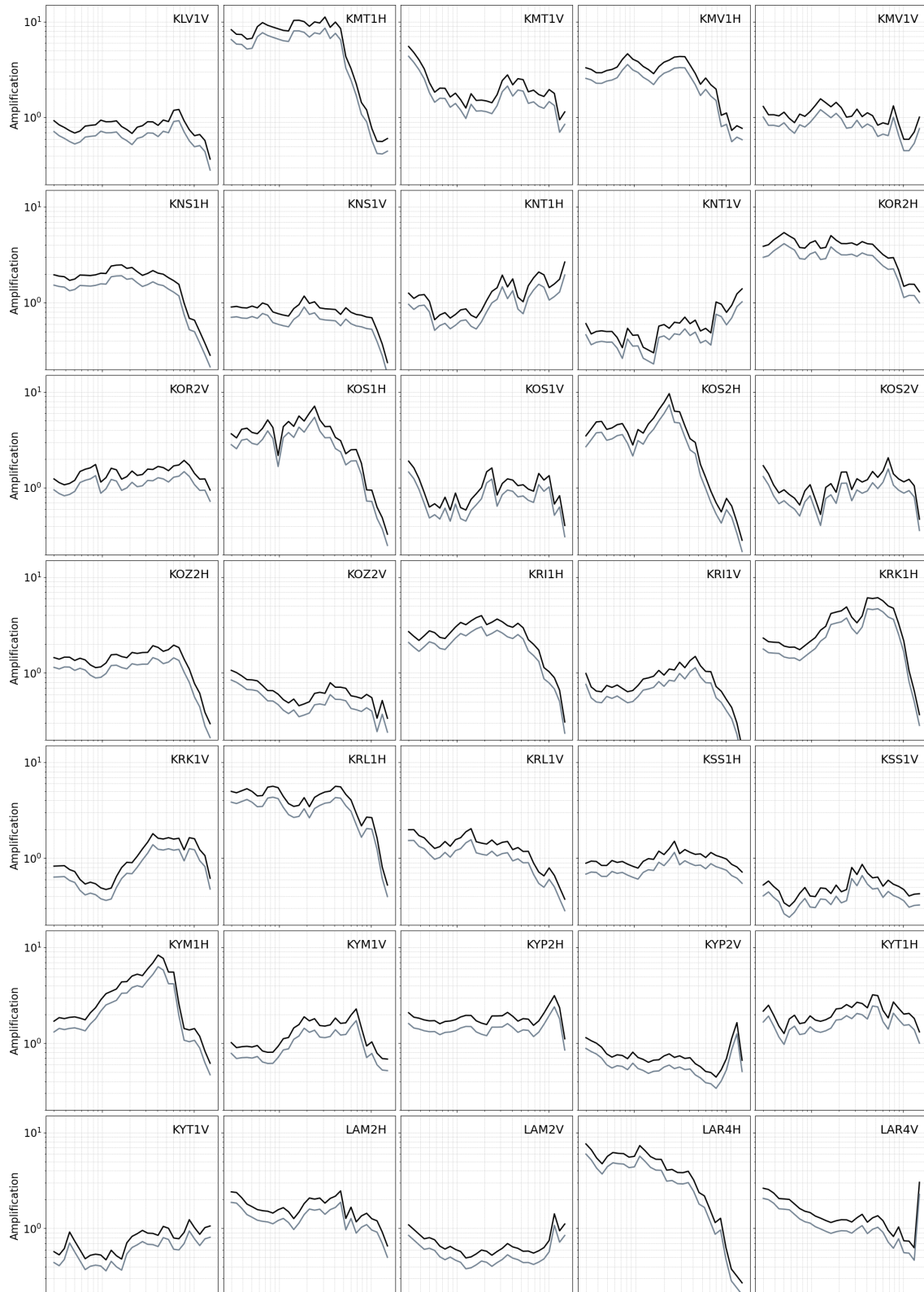
APPENDIX A. SITE AMPLIFICATION FACTORS (SAFS) FOR THE 152 STATIONS



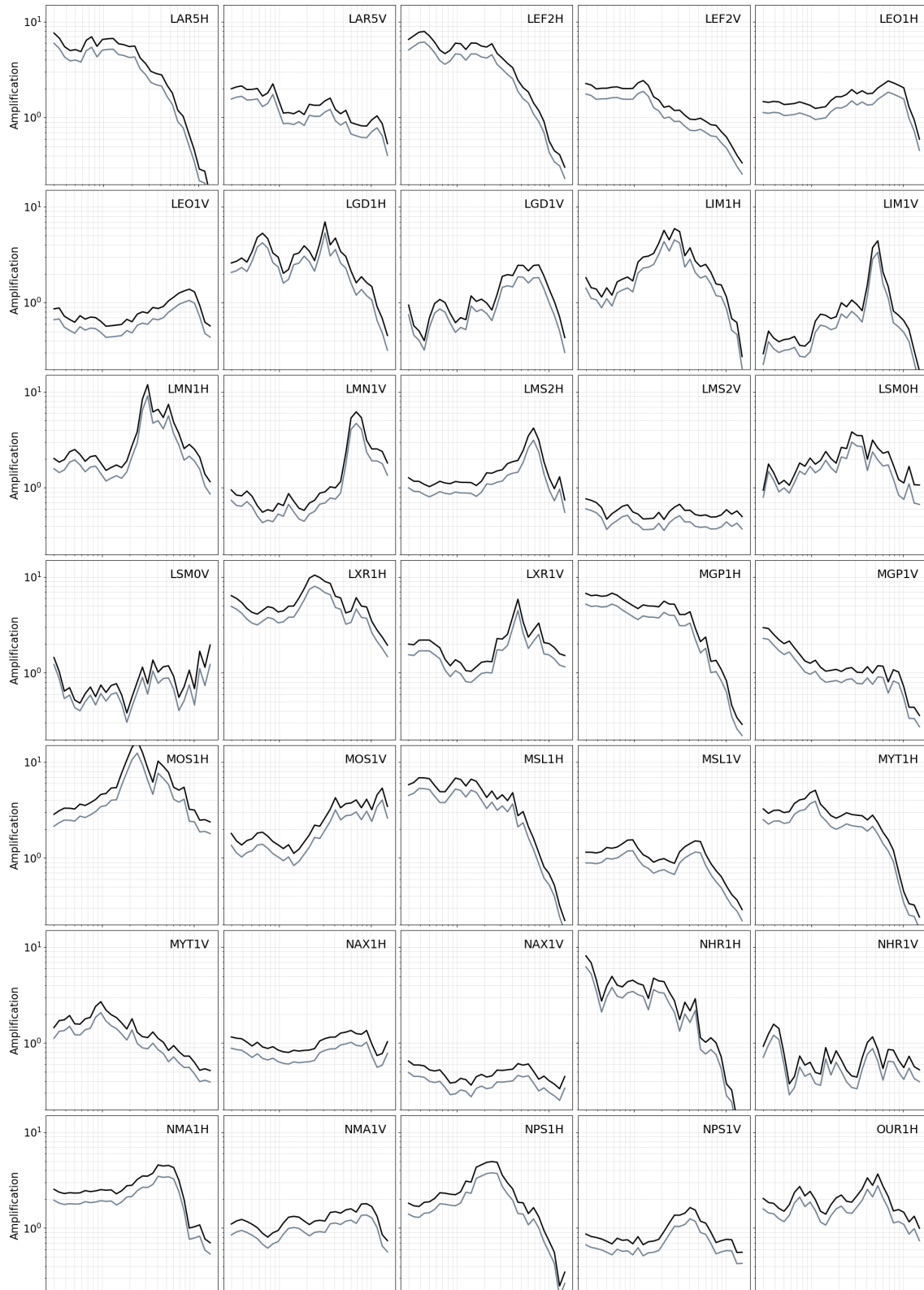
APPENDIX A. SITE AMPLIFICATION FACTORS (SAFS) FOR THE 152 STATIONS



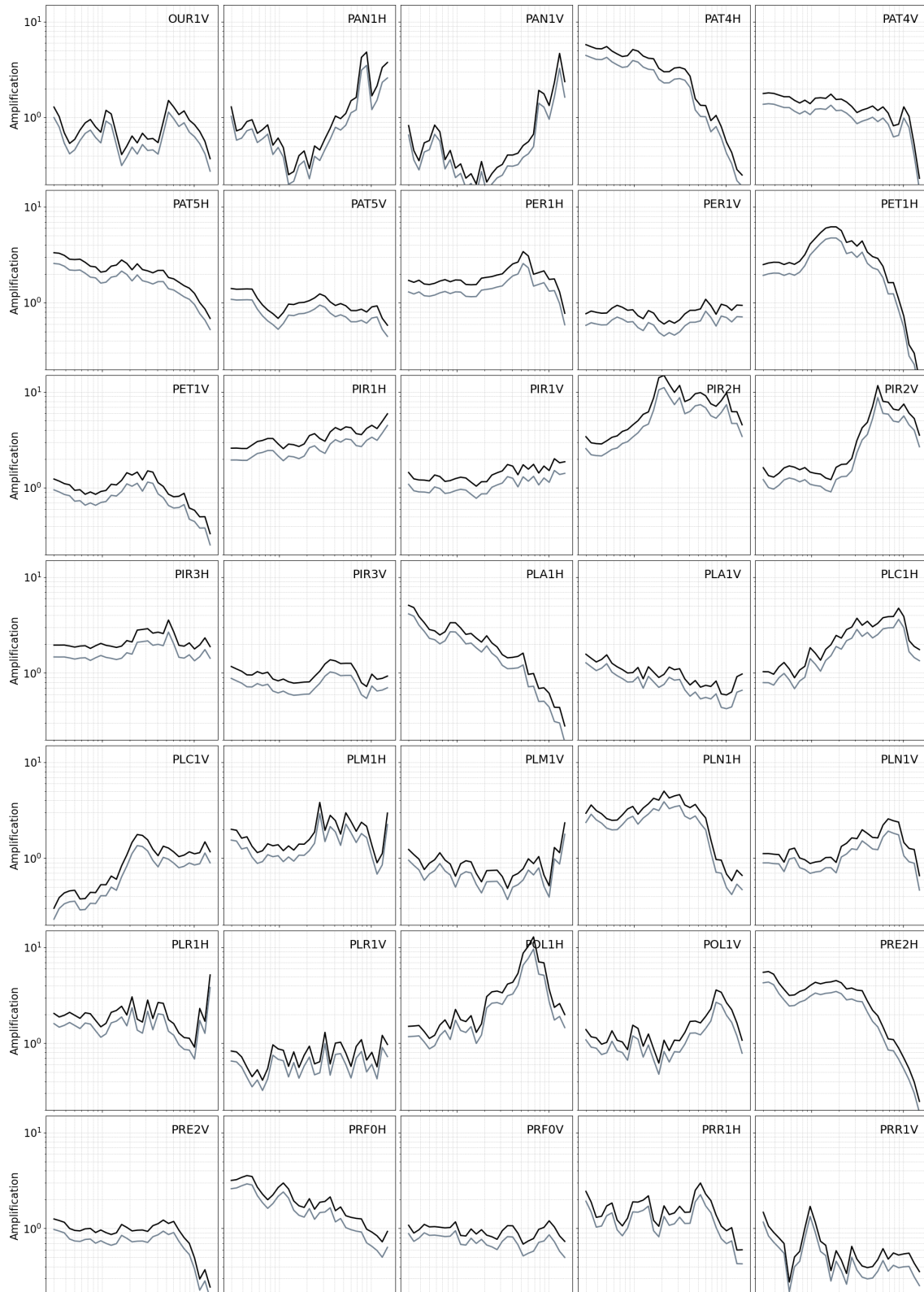
APPENDIX A. SITE AMPLIFICATION FACTORS (SAFs) FOR THE 152 STATIONS



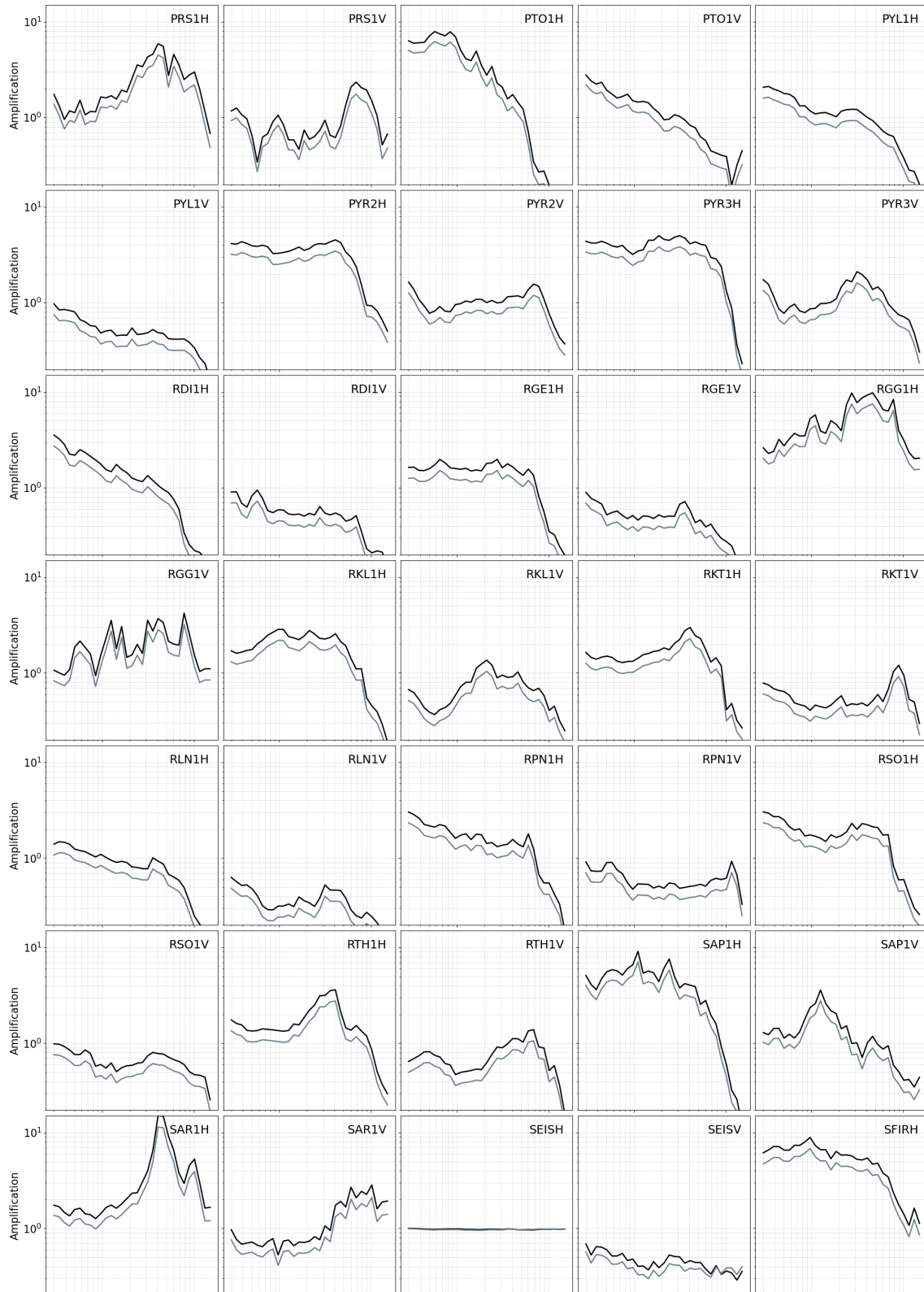
APPENDIX A. SITE AMPLIFICATION FACTORS (SAFS) FOR THE 152 STATIONS



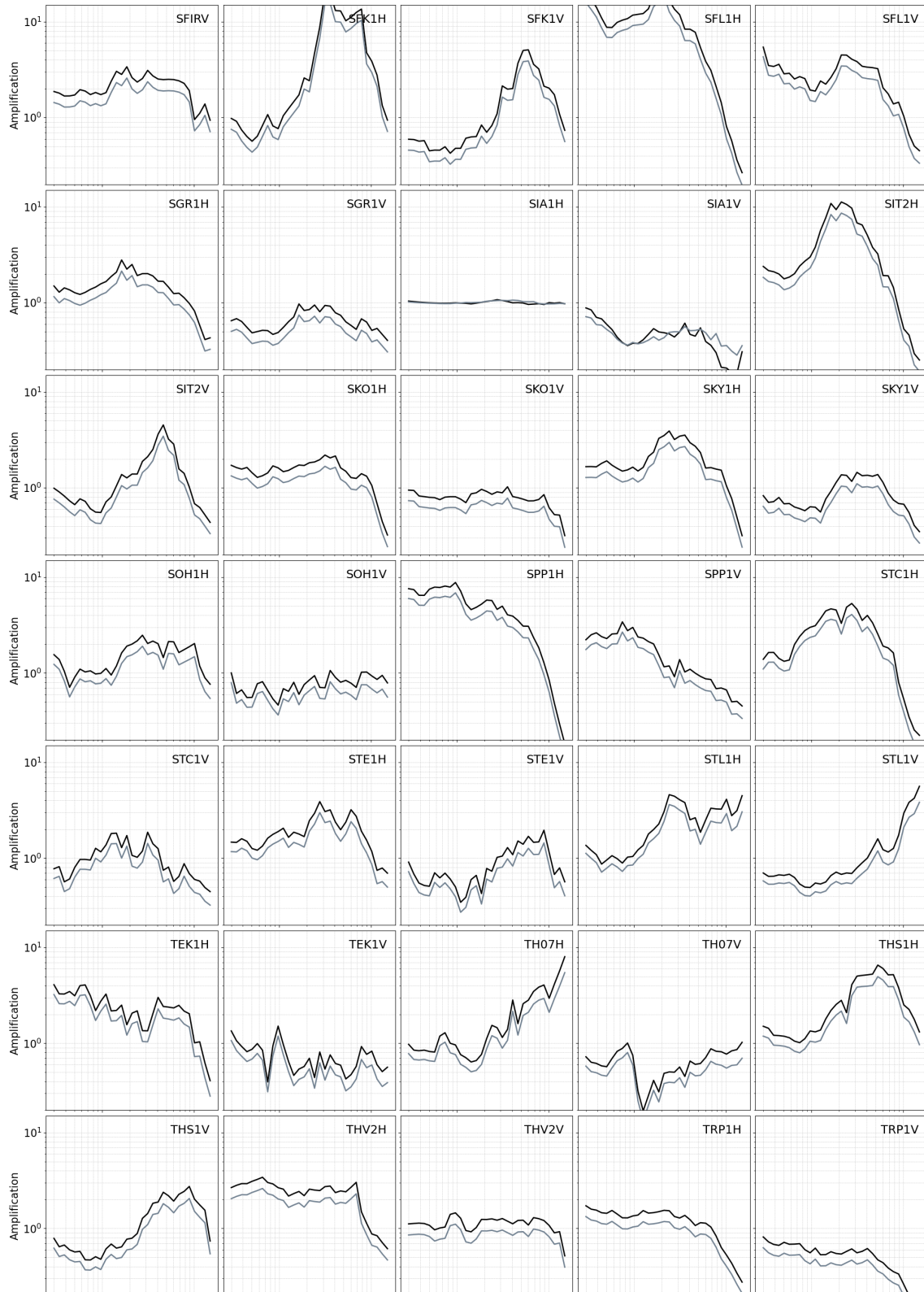
APPENDIX A. SITE AMPLIFICATION FACTORS (SAFs) FOR THE 152 STATIONS



APPENDIX A. SITE AMPLIFICATION FACTORS (SAFs) FOR THE 152 STATIONS



APPENDIX A. SITE AMPLIFICATION FACTORS (SAFS) FOR THE 152 STATIONS



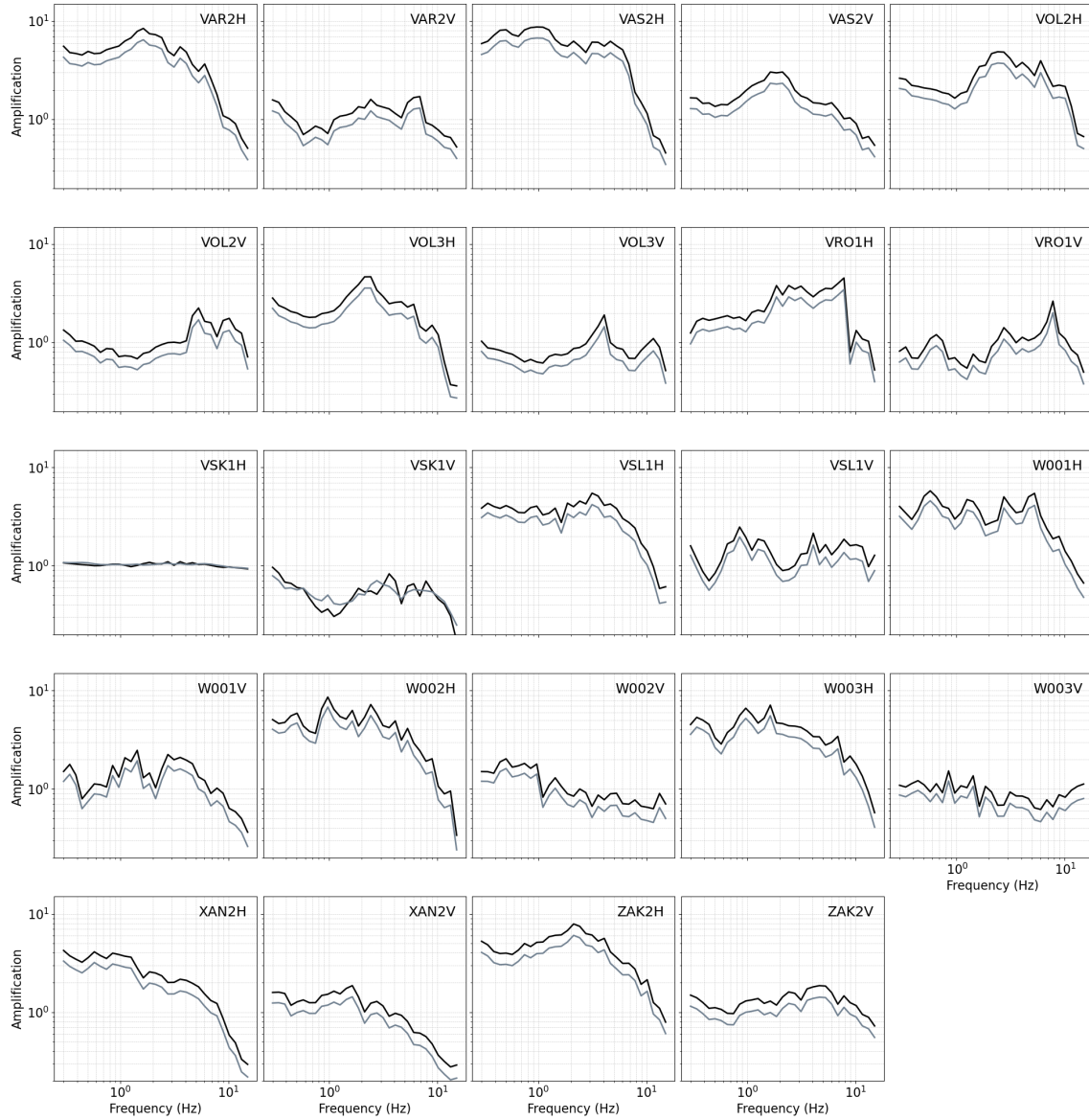


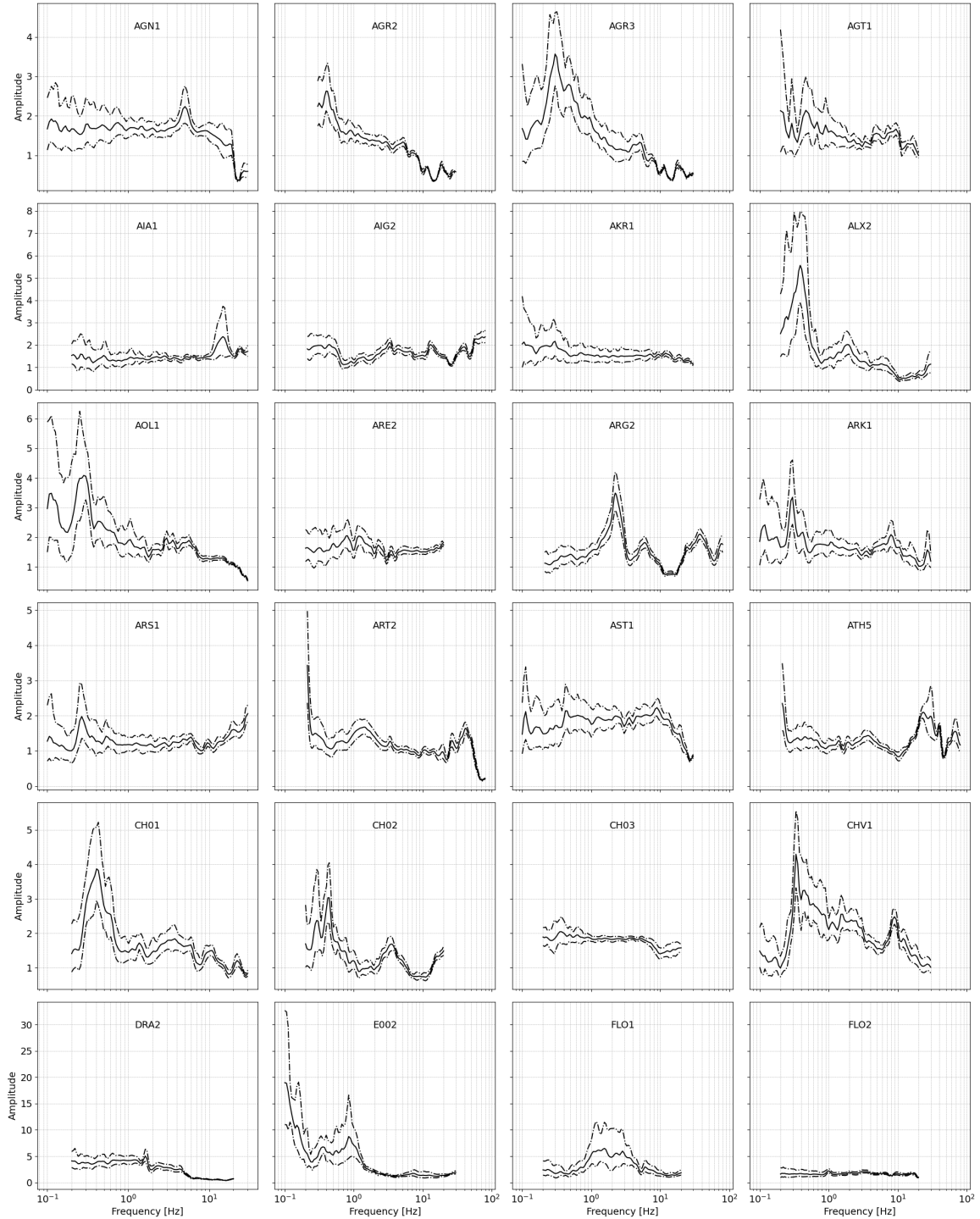
Figure A.1: Horizontal and Vertical Site Amplification Factors for engineering bedrock (grey lines) against the Horizontal and Vertical Site Amplification Factors for seismological bedrock (black lines) for each of the 152 stations



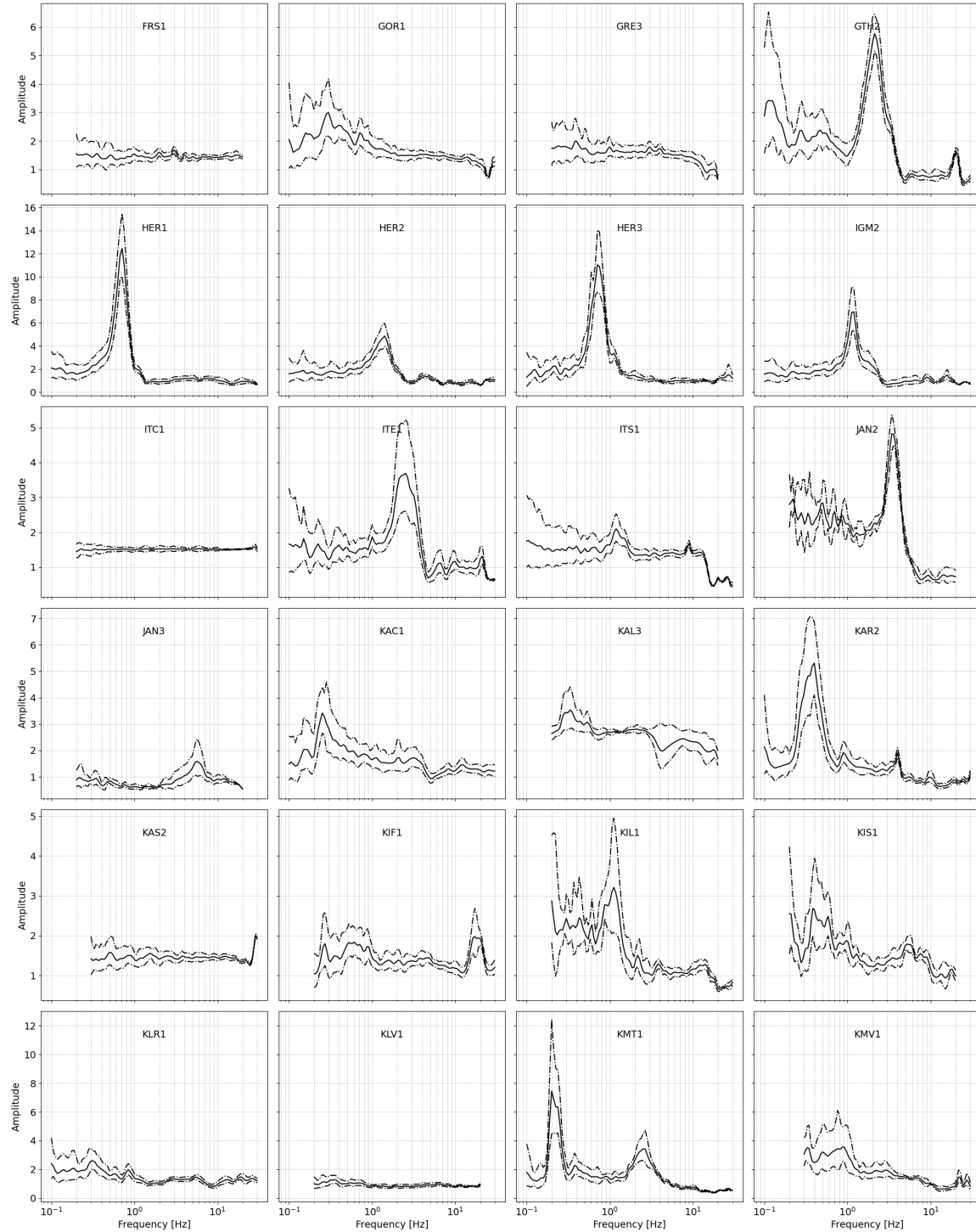
Appendix A

mHVSRS of 132 stations out of the 152 total stations.

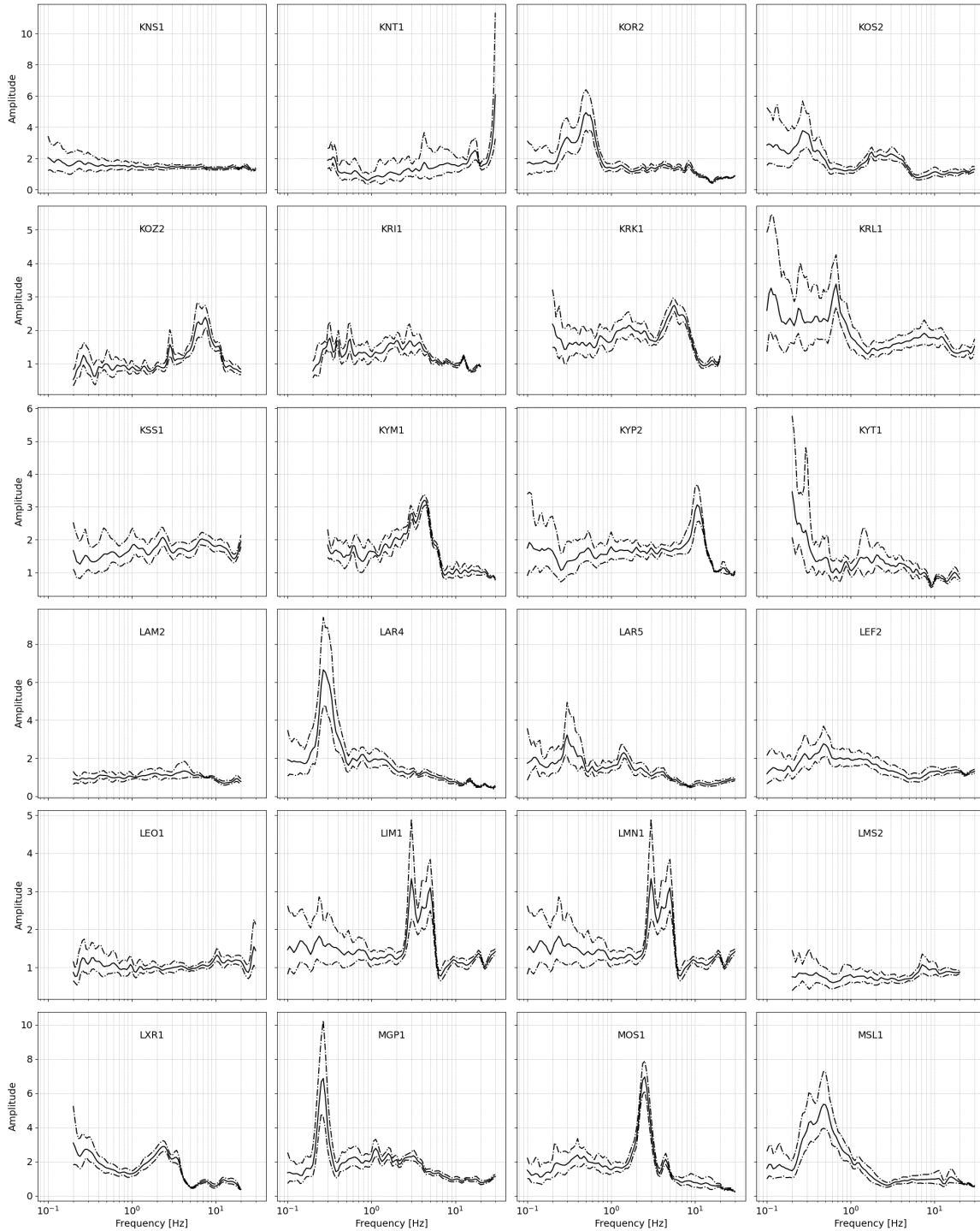
APPENDIX A. MHVSRs OF 132 STATIONS OUT OF THE 152 TOTAL STATIONS.



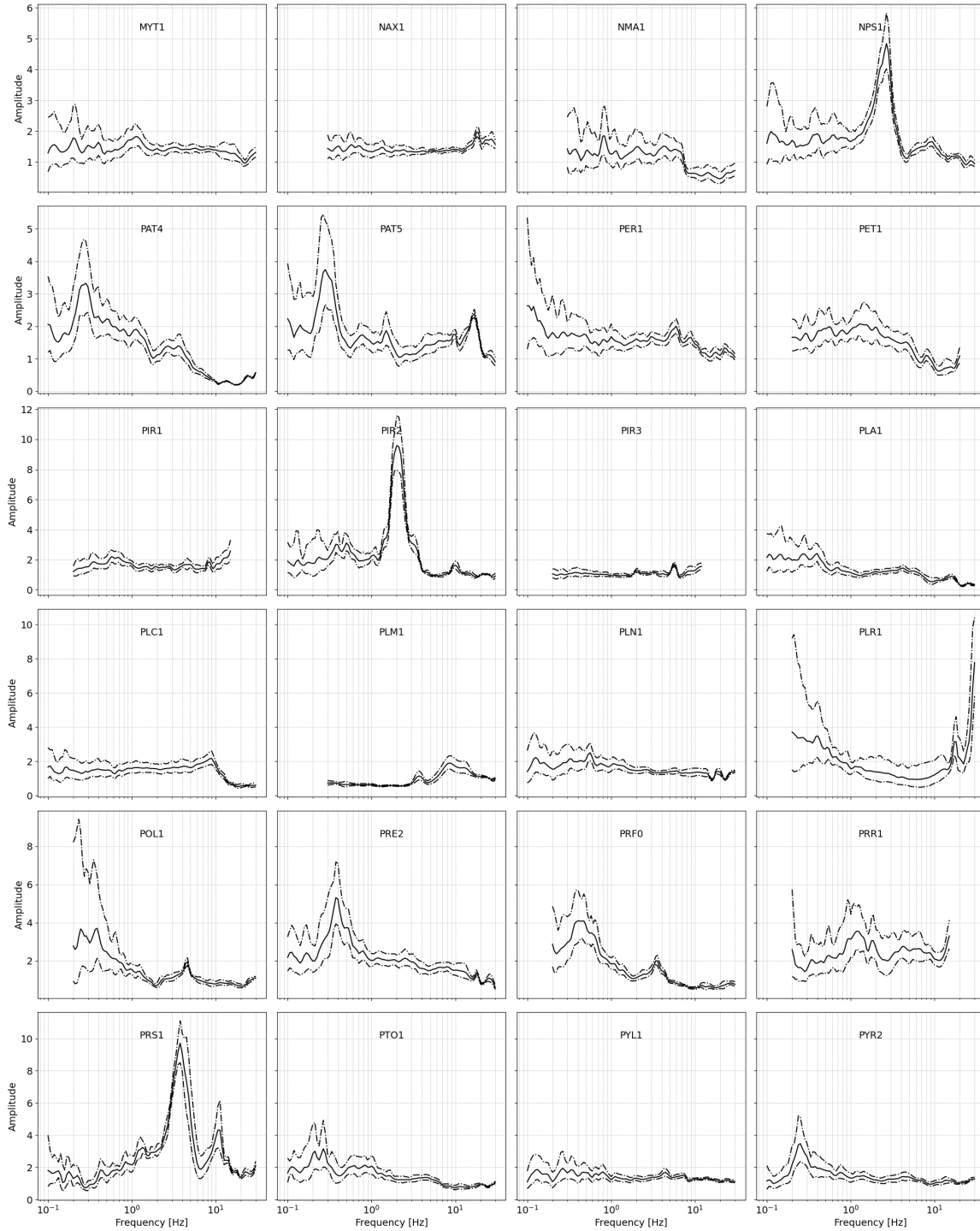
APPENDIX A. MHVRS OF 132 STATIONS OUT OF THE 152 TOTAL STATIONS.



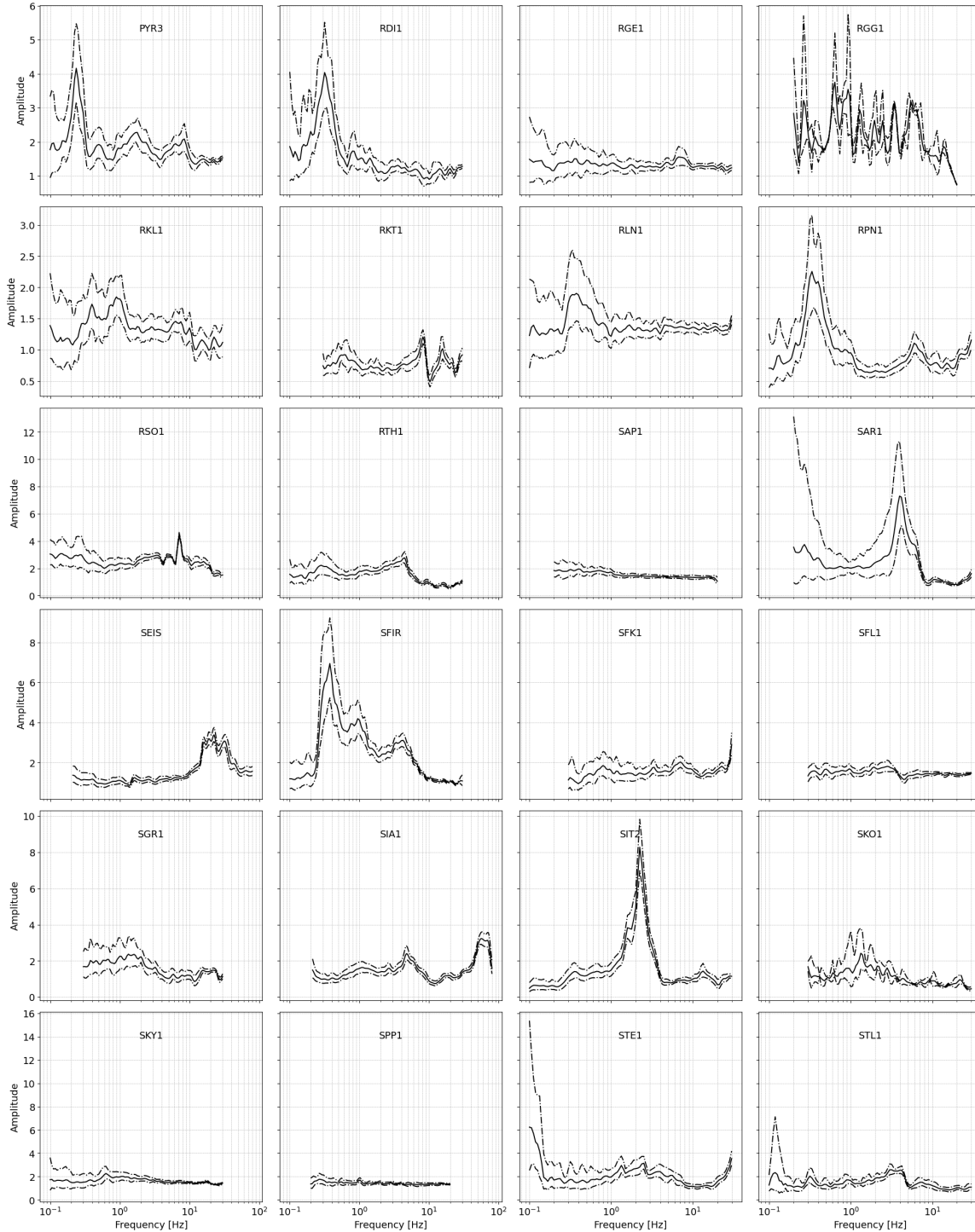
APPENDIX A. MHVRS OF 132 STATIONS OUT OF THE 152 TOTAL STATIONS.



APPENDIX A. MHVRSRS OF 132 STATIONS OUT OF THE 152 TOTAL STATIONS.



APPENDIX A. MHVRS OF 132 STATIONS OUT OF THE 152 TOTAL STATIONS.



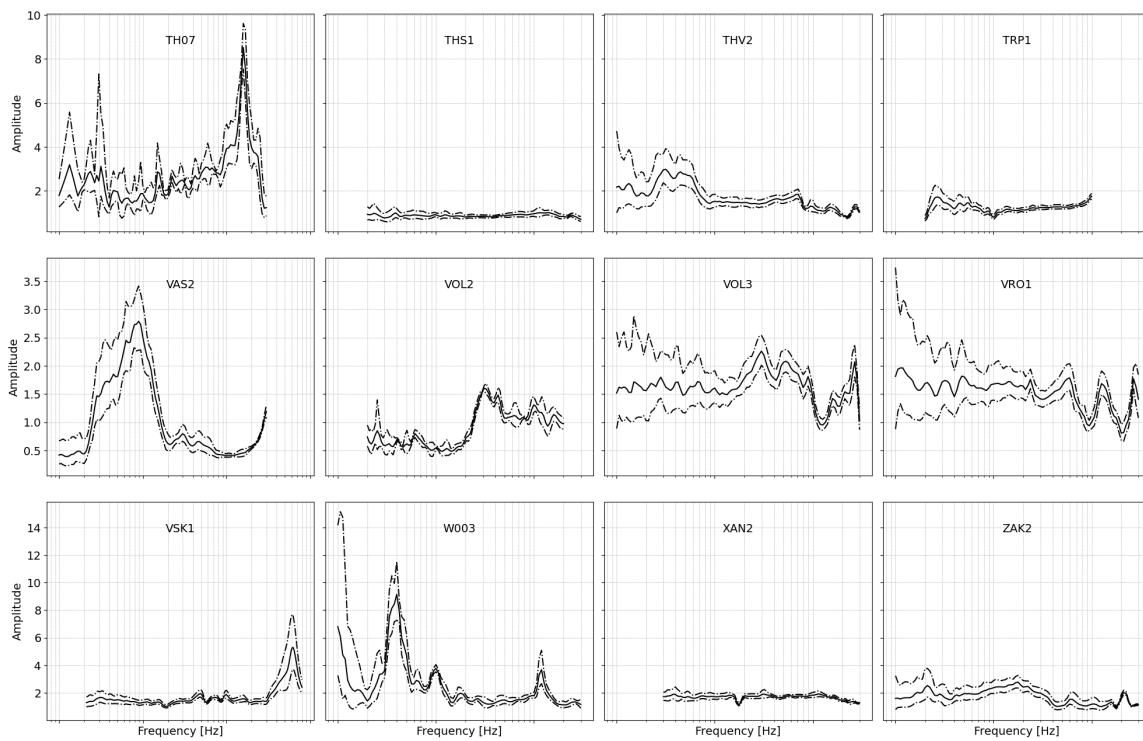


Figure A.1: Horizontal-to-Vertical Spectra Ratio of ambient noise (mHVSR) for 132 of 152 studied stations produced from Geopsy software.



Appendix A

Additional tables

Table A.1: Categorization of sites based on the peak Frequency f_p and peak Amplitude A_p of Horizontal-to-Vertical Spectral Ratios of Earthquakes (eHVSRs). This categorization was used for log-average Vertical Amplification Correction Functions (VACFs) calculation in each category and depicted in figure 4.22a.

| f_p [Hz] | A_p | Number of Sites | Log-average of f_p (Hz) | Log-average of A_p |
|--------------------|--------------|-----------------|---------------------------|----------------------|
| $f_p \leq 1$ | $A_p < 5$ | 27 | 0.6079 | 2.9037 |
| $f_p \leq 1$ | $A_p \geq 5$ | 7 | 0.6201 | 6.7744 |
| $1 < f_p \leq 5$ | $A_p < 5$ | 75 | 2.306 | 3.0188 |
| $1 < f_p \leq 5$ | $A_p \geq 5$ | 22 | 2.0564 | 6.3467 |
| $5 < f_p \leq 10$ | $A_p < 5$ | 14 | 7.254 | 3.0144 |
| $5 < f_p \leq 10$ | $A_p \geq 5$ | 1 | 6.86 | 6.244 |
| $10 < f_p \leq 20$ | $A_p < 5$ | 5 | 12.8271 | 2.8917 |
| $10 < f_p \leq 20$ | $A_p \geq 5$ | 1 | 11.186 | 7.263 |

Table A.2: Categorization of sites based on the peak Frequency f_p and peak Amplitude A_p of Vertical-to-Horizontal Spectra Ratios of Earthquakes (eVHSRs). This categorization was used for log-average Vertical Amplification Correction Functions (VACFs) calculation in each category and depicted in figure 4.22b.

| f_p [Hz] | A_p | Number of Sites | Log-average of f_p (Hz) | Log-average of A_p |
|--------------------|--------------|-----------------|---------------------------|----------------------|
| $f_p \leq 1$ | $A_p < 5$ | 34 | 0.6104 | 0.2893 |
| $f_p \leq 1$ | $A_p \geq 5$ | 0 | - | - |
| $1 < f_p \leq 2$ | $A_p < 5$ | 38 | 1.4607 | 0.2700 |
| $1 < f_p \leq 2$ | $A_p \geq 5$ | 0 | - | - |
| $2 < f_p \leq 5$ | $A_p < 5$ | 59 | 2.965 | 0.2865 |
| $2 < f_p \leq 5$ | $A_p \geq 5$ | 0 | - | - |
| $5 < f_p \leq 10$ | $A_p < 5$ | 15 | 7.2271 | 0.316 |
| $5 < f_p \leq 10$ | $A_p \geq 5$ | 0 | - | - |
| $10 < f_p \leq 20$ | $A_p < 5$ | 6 | 12.5378 | 0.2966 |
| $10 < f_p \leq 20$ | $A_p \geq 5$ | 0 | - | - |

Table A.3: Log-average Vertical Amplification Correction Functions (VACFs) for all 152 stations used in the present study (figure 4.24).

| <i>freq</i> [Hz] | <i>VACFs</i> | <i>log - std</i> |
|------------------|--------------|------------------|
| 0.3000 | 1.5542 | 0.9955 |
| 0.3420 | 1.4659 | 0.8669 |
| 0.3890 | 1.3643 | 0.8265 |
| 0.4440 | 1.2888 | 0.7565 |
| 0.5050 | 1.2746 | 0.7197 |
| 0.5760 | 1.2486 | 0.7110 |
| 0.6560 | 1.2481 | 0.7452 |
| 0.7470 | 1.2073 | 0.7157 |
| 0.8510 | 1.2236 | 0.7338 |
| 0.9700 | 1.2476 | 0.8128 |
| 1.1050 | 1.2608 | 0.8704 |
| 1.2590 | 1.2305 | 0.9804 |
| 1.4350 | 1.2509 | 1.0055 |
| 1.6340 | 1.2610 | 0.8685 |
| 1.8620 | 1.2875 | 0.8089 |
| 2.1210 | 1.3113 | 0.8201 |
| 2.4170 | 1.3408 | 0.8478 |
| 2.7530 | 1.3980 | 0.7928 |
| 3.1370 | 1.4932 | 0.9491 |
| 3.5740 | 1.5034 | 0.9121 |
| 4.0720 | 1.5589 | 1.0824 |
| 4.6390 | 1.5526 | 1.3330 |
| 5.2850 | 1.5121 | 1.5127 |
| 6.0210 | 1.4395 | 1.2827 |
| 6.8600 | 1.3698 | 1.3523 |
| 7.8150 | 1.2805 | 1.1991 |
| 8.9040 | 1.1723 | 0.9906 |
| 10.1400 | 1.0592 | 0.9951 |
| 11.5600 | 0.9280 | 0.7741 |
| 13.1700 | 0.8165 | 0.7682 |
| 15.0000 | 0.7021 | 0.7565 |

Table A.4: Fundamental frequency, f_0 , for all 152 stations.

| Stations | $freq$ [Hz] |
|----------|-------------|----------|-------------|----------|-------------|----------|-------------|
| AGN1 | 4.9962 | IGM2 | 1.1575 | LMS2 | 8.2309 | RKT1 | 00.0000 |
| AGR2 | 0.4065 | ITC1 | 27.8724 | LSM0 | 3.0000 | RLN1 | 0.3890 |
| AGR3 | 0.3039 | ITE1 | 2.4561 | LXR1 | 2.3577 | RPN1 | 0.3719 |
| AGT1 | 9.8279 | ITS1 | 1.2383 | MGP1 | 0.2551 | RSO1 | 7.1053 |
| AIA1 | 14.5592 | JAN2 | 3.5799 | MOS1 | 2.5106 | RTH1 | 4.2312 |
| AIG2 | 69.0566 | JAN3 | 5.5973 | MSL1 | 0.4655 | SAP1 | 0.4070 |
| AKR1 | 0.3056 | KAC1 | 0.2870 | MYT1 | 1.1232 | SAR1 | 4.0520 |
| ALX2 | 0.3914 | KAL3 | 0.3167 | NAX1 | 18.3592 | SEIS | 21.7755 |
| AMK1 | 0.2195 | KAR2 | 0.3788 | NHR1 | 0.2644 | SFIR | 0.3709 |
| AOL1 | 0.2768 | KAS2 | 28.6365 | NMA1 | 0.8921 | SFK1 | 7.2198 |
| ARE2 | 0.8095 | KIF1 | 17.6010 | NPS1 | 2.5490 | SFL1 | 2.7119 |
| ARG2 | 2.2685 | KIL1 | 1.0116 | OUR1 | 3.5773 | SGR1 | 1.2958 |
| ARK1 | 0.2964 | KIS1 | 0.4374 | PAN1 | 0.4570 | SIA1 | 59.8694 |
| ARN1 | 2.2466 | KLR1 | 0.3157 | PAT4 | 0.2666 | SIT2 | 2.2657 |
| ARS1 | 0.2813 | KLV1 | 0.3280 | PAT5 | 0.2816 | SKO1 | 1.2222 |
| ART2 | 21.3474 | KMT1 | 0.2136 | PER1 | 5.8559 | SKY1 | 0.6519 |
| AST1 | 9.2741 | KMV1 | 0.8074 | PET1 | 1.2372 | SOH1 | 22.0000 |
| ATH5 | 20.2376 | KNS1 | 0.1465 | PIR1 | 0.6109 | SPP1 | 0.2683 |
| CH01 | 0.4020 | KNT1 | 17.1764 | PIR2 | 2.0372 | STC1 | 2.2710 |
| CH02 | 0.4373 | KOR2 | 0.5174 | PIR3 | 5.7001 | STE1 | 2.2971 |
| CH03 | 0.3750 | KOS1 | 0.2769 | PLA1 | 0.3789 | STL1 | 3.5869 |
| CHV1 | 0.3599 | KOS2 | 0.2741 | PLC1 | 8.4280 | TEK1 | 0.4840 |
| DRA2 | 1.6020 | KOZ2 | 7.0242 | PLM1 | 8.5485 | TH07 | 16.2326 |
| E001 | 1.0000 | KRI1 | 0.3498 | PLN1 | 0.5497 | THS1 | 13.5822 |
| E002 | 0.9277 | KRK1 | 6.0254 | PLR1 | 0.4155 | THV2 | 0.3329 |
| E003 | 0.7000 | KRL1 | 0.6692 | POL1 | 0.3763 | TRP1 | 0.2861 |
| FLO1 | 1.5236 | KSS1 | 2.2685 | PRE2 | 0.3724 | VAR2 | 1.6995 |
| FLO2 | 0.9984 | KYM1 | 4.2847 | PRF0 | 0.4546 | VAS2 | 0.8701 |
| FRM1 | 0.7320 | KYP2 | 10.6425 | PRR1 | 1.2276 | VOL2 | 3.1136 |
| FRS1 | 3.1105 | KYT1 | 00.0000 | PRS1 | 3.9388 | VOL3 | 2.8390 |
| GOR1 | 0.3045 | LAM2 | 4.2307 | PTO1 | 0.2562 | VRO1 | 0.1363 |
| GRA1 | 1.7330 | LAR4 | 0.2893 | PYL1 | 0.2800 | VSK1 | 62.0069 |
| GRE3 | 0.3903 | LAR5 | 0.3333 | PYR2 | 0.2607 | VSL1 | 0.5071 |
| GTH2 | 2.1168 | LEF2 | 0.4870 | PYR3 | 0.2458 | W001 | 0.8500 |
| HER1 | 0.6984 | LEO1 | 28.3787 | RD11 | 0.3193 | W002 | 0.4260 |
| HER2 | 1.3362 | LGD1 | 0.6085 | RGE1 | 6.8857 | W003 | 0.3847 |
| HER3 | 0.7114 | LIM1 | 3.2978 | RGG1 | 0.7841 | XAN2 | 11.0394 |
| IER1 | 1.2856 | LMN1 | 3.2978 | RKL1 | 0.9236 | ZAK2 | 1.7218 |

Table A.5: The longitude and latitude as well as the total records at the 152 stations used in the present study.

| Station name | Latitude | Longitude | Record's samples | Station name | Latitude | Longitude | Record's samples |
|--------------|----------|-----------|------------------|--------------|----------|-----------|------------------|
| AGN1 | 35.188 | 25.716 | 79.0 | KLR1 | 40.583 | 22.950 | 56.0 |
| AGR2 | 38.632 | 21.414 | 21.0 | KLV1 | 38.033 | 22.108 | 118.0 |
| AGR3 | 38.589 | 21.416 | 52.0 | KMT1 | 41.116 | 25.407 | 35.0 |
| AGT1 | 38.251 | 20.384 | 4.0 | KMV1 | 38.779 | 22.785 | 79.0 |
| AIA1 | 40.164 | 21.820 | 55.0 | KNS1 | 40.048 | 20.752 | 98.0 |
| AIG2 | 38.242 | 22.072 | 99.0 | KNT1 | 41.167 | 22.900 | 9.0 |
| AKR1 | 38.154 | 22.313 | 100.0 | KOR2 | 37.940 | 22.950 | 79.0 |
| ALX2 | 40.845 | 25.874 | 27.0 | KOS1 | 36.892 | 27.290 | 12.0 |
| AMK1 | 40.520 | 22.989 | 6.0 | KOS2 | 36.894 | 27.289 | 12.0 |
| AOL1 | 37.643 | 21.625 | 120.0 | KOZ2 | 40.305 | 21.784 | 95.0 |
| ARE2 | 36.666 | 22.383 | 93.0 | KRI1 | 37.662 | 20.817 | 73.0 |
| ARG2 | 38.178 | 20.488 | 85.0 | KRK1 | 39.618 | 19.916 | 97.0 |
| ARK1 | 35.149 | 25.264 | 63.0 | KRL1 | 37.795 | 26.706 | 65.0 |
| ARN1 | 40.488 | 23.596 | 3.0 | KSS1 | 35.419 | 26.921 | 40.0 |
| ARS1 | 37.635 | 22.729 | 50.0 | KYM1 | 38.634 | 24.106 | 84.0 |
| ART2 | 39.148 | 20.994 | 100.0 | KYP2 | 37.250 | 21.667 | 84.0 |
| AST1 | 38.542 | 21.090 | 124.0 | KYT1 | 36.299 | 22.964 | 10.0 |
| ATH5 | 37.975 | 23.737 | 39.0 | LAM2 | 38.902 | 22.432 | 88.0 |
| CH01 | 35.517 | 24.021 | 75.0 | LAR4 | 39.642 | 22.422 | 86.0 |
| CH02 | 35.515 | 24.031 | 75.0 | LAR5 | 39.640 | 22.411 | 36.0 |
| CH03 | 35.533 | 24.070 | 9.0 | LEF2 | 38.830 | 20.708 | 109.0 |
| CHV1 | 38.184 | 20.382 | 13.0 | LEO1 | 37.169 | 22.864 | 93.0 |
| DRA2 | 41.159 | 24.148 | 24.0 | LGD1 | 40.749 | 23.070 | 12.0 |
| E001 | 40.671 | 23.307 | 8.0 | LIM1 | 39.877 | 25.060 | 4.0 |
| E002 | 40.674 | 23.315 | 8.0 | LMN1 | 39.875 | 25.059 | 38.0 |
| E003 | 40.676 | 23.324 | 11.0 | LMS2 | 40.835 | 21.142 | 68.0 |
| FLO1 | 40.779 | 21.400 | 4.0 | LSM0 | 40.628 | 22.960 | 8.0 |
| FLO2 | 40.780 | 21.405 | 68.0 | LXR1 | 38.201 | 20.437 | 61.0 |
| FRM1 | 40.655 | 23.298 | 8.0 | MGP1 | 37.402 | 22.138 | 101.0 |
| FRS1 | 39.293 | 22.384 | 101.0 | MOS1 | 37.953 | 23.682 | 77.0 |
| GOR1 | 35.058 | 24.963 | 69.0 | MSL1 | 38.373 | 21.424 | 102.0 |
| GRA1 | 40.675 | 23.289 | 11.0 | MYT1 | 39.085 | 26.569 | 51.0 |
| GRE3 | 40.085 | 21.438 | 96.0 | NAX1 | 37.101 | 25.374 | 98.0 |
| GTH2 | 36.760 | 22.566 | 67.0 | NHR1 | 41.180 | 23.281 | 4.0 |
| HER1 | 35.318 | 25.102 | 71.0 | NMA1 | 37.819 | 22.663 | 110.0 |
| HER2 | 35.338 | 25.136 | 78.0 | NPS1 | 36.513 | 23.062 | 64.0 |
| HER3 | 35.330 | 25.107 | 72.0 | OUR1 | 40.333 | 23.979 | 9.0 |
| IER1 | 40.397 | 23.875 | 4.0 | PAN1 | 40.585 | 23.031 | 5.0 |
| IGM2 | 39.486 | 20.259 | 23.0 | PAT4 | 38.234 | 21.748 | 106.0 |
| ITC1 | 38.365 | 20.716 | 70.0 | PAT5 | 38.296 | 21.795 | 84.0 |
| ITE1 | 38.434 | 22.427 | 37.0 | PER1 | 38.012 | 23.703 | 83.0 |
| ITS1 | 40.605 | 23.012 | 35.0 | PET1 | 36.964 | 21.925 | 95.0 |
| JAN2 | 39.664 | 20.852 | 107.0 | PIR1 | 37.937 | 23.643 | 84.0 |
| JAN3 | 39.684 | 20.838 | 91.0 | PIR2 | 37.946 | 23.671 | 76.0 |
| KAC1 | 38.138 | 21.548 | 135.0 | PIR3 | 37.957 | 23.652 | 90.0 |
| KAL3 | 37.025 | 22.103 | 82.0 | PLA1 | 40.556 | 22.989 | 22.0 |
| KAR2 | 39.366 | 21.919 | 104.0 | PLC1 | 35.231 | 23.683 | 20.0 |
| KAS2 | 40.505 | 21.281 | 94.0 | PLM1 | 38.975 | 26.369 | 17.0 |
| KIF1 | 38.077 | 23.815 | 83.0 | PLN1 | 39.998 | 23.575 | 43.0 |
| KIL1 | 40.990 | 22.868 | 5.0 | PLR1 | 39.936 | 23.677 | 4.0 |
| KIS1 | 35.494 | 23.659 | 22.0 | POL1 | 40.380 | 23.441 | 4.0 |

| Station name | Latitude | Longitude | Record's samples |
|--------------|----------|-----------|------------------|
| PRE2 | 38.958 | 20.755 | 104.0 |
| PRF0 | 40.593 | 22.956 | 41.0 |
| PRR1 | 40.683 | 23.279 | 3.0 |
| PRS1 | 40.680 | 23.286 | 4.0 |
| PTO1 | 40.510 | 21.682 | 91.0 |
| PYL1 | 36.914 | 21.695 | 101.0 |
| PYR2 | 37.667 | 21.451 | 119.0 |
| PYR3 | 37.679 | 21.462 | 82.0 |
| RDI1 | 36.451 | 28.224 | 59.0 |
| RGE1 | 36.027 | 27.931 | 60.0 |
| RGG1 | 38.719 | 22.709 | 4.0 |
| RKL1 | 36.337 | 28.171 | 61.0 |
| RKT1 | 35.954 | 27.767 | 53.0 |
| RLN1 | 36.089 | 28.087 | 56.0 |
| RPN1 | 36.449 | 28.218 | 56.0 |
| RSO1 | 36.363 | 28.002 | 58.0 |
| RTH1 | 35.365 | 24.472 | 73.0 |
| SAP1 | 41.023 | 25.701 | 7.0 |
| SAR1 | 40.097 | 23.978 | 13.0 |
| SEIS | 40.632 | 22.963 | 69.0 |
| SFIR | 36.421 | 25.428 | 59.0 |
| SFK1 | 35.256 | 24.173 | 12.0 |
| SFL1 | 41.190 | 26.304 | 40.0 |
| SGR1 | 39.211 | 25.855 | 60.0 |
| SIA1 | 40.257 | 21.553 | 90.0 |
| SIT2 | 35.206 | 26.107 | 83.0 |
| SKO1 | 39.123 | 23.729 | 69.0 |
| SKY1 | 38.904 | 24.565 | 70.0 |
| SOH1 | 40.821 | 23.356 | 9.0 |
| SPP1 | 41.023 | 25.701 | 32.0 |
| STC1 | 40.649 | 23.305 | 5.0 |
| STE1 | 40.645 | 23.305 | 9.0 |
| STL1 | 40.662 | 22.935 | 42.0 |
| TEK1 | 40.684 | 22.891 | 4.0 |
| TH07 | 40.638 | 22.949 | 4.0 |
| THS1 | 40.738 | 24.575 | 54.0 |
| THV2 | 38.316 | 23.320 | 90.0 |
| TRP1 | 37.511 | 22.363 | 99.0 |
| VAR2 | 37.864 | 21.208 | 55.0 |
| VAS2 | 38.630 | 20.608 | 116.0 |
| VOL2 | 39.366 | 22.951 | 82.0 |
| VOL3 | 39.374 | 22.935 | 94.0 |
| VRO1 | 38.406 | 26.134 | 11.0 |
| VSK1 | 38.409 | 20.564 | 85.0 |
| VSL1 | 40.479 | 23.136 | 8.0 |
| W001 | 40.665 | 23.274 | 8.0 |
| W002 | 40.661 | 23.260 | 11.0 |
| W003 | 40.660 | 23.251 | 9.0 |
| XAN2 | 41.142 | 24.891 | 34.0 |
| ZAK2 | 37.788 | 20.900 | 92.0 |

Table A.6: Categorization of sites according to 2024 draft EC8, based on the standard categorisation shown in Table 4.15 (second column) and based on $V_{S,H}$ and f_0 categorisation shown in Table 4.16 (third column). The categories inside the parenthesis are based on the standard deviation of $V_{S,H}$ and f_0 .

| Stations | Stand. Cat. | $V_{S,H}$ and f_0 | Stations | Stand. Cat. | $V_{S,H}$ and f_0 | Stations | Stand. Cat. | $V_{S,H}$ and f_0 |
|----------|-------------|---------------------|----------|-------------|---------------------|----------|-------------|---------------------|
| AGN1 | B | B (E) | KLR1 | U | B | PRE2 | U | B |
| AGR2 | U | B | KLV1 | B | B | PRF0 | B | B |
| AGR3 | B | B | KMT1 | B | B | PRR1 | U | F |
| AGT1 | E | E (B) | KMV1 | B | B (F) | PRS1 | B | B (E) |
| AIA1 | E | E (A) | KNS1 | U | B | PTO1 | U | B |
| AIG2 | A | A | KNT1 | E | A (E) | PYL1 | U | B |
| AKR1 | U | B | KOR2 | B | B (F) | PYR2 | B | B |
| ALX2 | U | B | KOS1 | U | B | PYR3 | B | B (F) |
| AMK1 | U | B | KOS2 | U | B | RD11 | B | B |
| AOL1 | B | B | KOZ2 | E | E (B) | RGE1 | E | E (B) |
| ARE2 | B | B (F) | KRI1 | U | B | RGG1 | B | B (F) |
| ARG2 | B | B (C) | KRK1 | E | E (B) | RKL1 | U | F |
| ARK1 | U | B | KRL1 | B | B (F) | RKT1 | A | A |
| ARN1 | B | B (E) | KSS1 | B | B (E) | RLN1 | U | B |
| ARS1 | U | B | KYM1 | B | B (E) | RPN1 | U | B |
| ART2 | A | A | KYP2 | B | A (E) | RSO1 | E | E (B) |
| AST1 | E | E (B) | KYT1 | A | A | RTH1 | B | B (E) |
| ATH5 | A | A | LAM2 | B | B (E) | SAP1 | B | B (F) |
| CH01 | U | B | LAR4 | B | B | SAR1 | E | E (B) |
| CH02 | U | B | LAR5 | U | B | SEIS | A | A |
| CH03 | U | B | LEF2 | B | B (F) | SFIR | U | B |
| CHV1 | U | B | LEO1 | A | A (E) | SFK1 | B | B (E) |
| DRA2 | B | B (C) | LGD1 | B | B (F) | SFL1 | C | E (B) |
| E001 | B | B (D) | LIM1 | B | B (E) | SGR1 | B | B (C) |
| E002 | B | B (F) | LMN1 | B | B (E) | SIA1 | A | A |
| E003 | B | B (F) | LMS2 | E | E (B) | SIT2 | C | C (B) |
| FLO1 | B | B (C) | LSM0 | B | B (E) | SKO1 | B | B (F) |
| FLO2 | U | F | LXR1 | C | C (B) | SKY1 | U | B |
| FRM1 | B | B | MGP1 | U | B | SOH1 | A | A |
| FRS1 | B | B (E) | MOS1 | B | B (E) | SPP1 | B | B (F) |
| GOR1 | U | B | MSL1 | B | B (F) | STC1 | B | B |
| GRA1 | C | C | MYT1 | B | B (F) | STE1 | B | B (E) |
| GRE3 | U | B | NAX1 | E | A | STL1 | B | B (E) |
| GTH2 | B | B (E) | NHR1 | B | B | TEK1 | U | B |
| HER1 | B | B (F) | NMA1 | B | B (F) | TH07 | E | E (A) |
| HER2 | B | B (C) | NPS1 | B | B (E) | THS1 | E | A (E) |
| HER3 | B | B (F) | OUR1 | B | B (E) | THV2 | B | B |
| IER1 | B | B (C) | PAN1 | U | B | TRP1 | U | B |
| IGM2 | B | B (F) | PAT4 | B | B | VAR2 | C | C (B/E) |
| ITC1 | A | E | PAT5 | U | B | VAS2 | B | B (F) |
| ITE1 | C | C (B/E) | PER1 | E | E (B) | VOL2 | B | B (E) |
| ITS1 | B | B (F) | PET1 | B | B (C) | VOL3 | B | B (E) |
| JAN2 | B | B (E) | PIR1 | B | B (F) | VR01 | U | B |
| JAN3 | E | E (B) | PIR2 | B | B (E) | VSK1 | A | A |
| KAC1 | B | B | PIR3 | E | E (B) | VSL1 | U | B |
| KAL3 | U | B | PLA1 | B | B | W001 | B | B (D) |
| KAR2 | B | B | PLC1 | B | B (E) | W002 | B | B |
| KAS2 | A | A (E) | PLM1 | B | B (E) | W003 | B | B (F) |
| KIF1 | E | E (A) | PLN1 | U | B | XAN2 | E | A |
| KIL1 | B | B (F) | PLR1 | U | B | ZAK2 | C | C (B/E) |
| KIS1 | U | B | POL1 | U | B | | | |